

University of New Hampshire

University of New Hampshire Scholars' Repository

Doctoral Dissertations

Student Scholarship

Spring 2021

Wind, Wave, and Engineering Effects on Tidal Inlet Morphodynamics

Joshua Lincoln Humberston
University of New Hampshire, Durham

Follow this and additional works at: <https://scholars.unh.edu/dissertation>

Recommended Citation

Humberston, Joshua Lincoln, "Wind, Wave, and Engineering Effects on Tidal Inlet Morphodynamics" (2021). *Doctoral Dissertations*. 2574.
<https://scholars.unh.edu/dissertation/2574>

This Dissertation is brought to you for free and open access by the Student Scholarship at University of New Hampshire Scholars' Repository. It has been accepted for inclusion in Doctoral Dissertations by an authorized administrator of University of New Hampshire Scholars' Repository. For more information, please contact nicole.hentz@unh.edu.

Wind, Wave, and Engineering Effects on Tidal Inlet Morphodynamics

BY

Joshua L Humberston

BS, University of Delaware, 2012

MS, University of New Hampshire, 2016

DISSERTATION

Submitted to the University of New Hampshire

in Partial Fulfillment of

the Requirements for the Degree of

Doctor of Philosophy

in

Oceanography

May, 2021

ALL RIGHTS RESERVED

©2021

Joshua L. Humberston

This dissertation has been examined and approved in partial fulfillment of the requirements for the degree of Doctorate of Philosophy in Oceanography by:

Dr. Thomas Lippmann, Dissertation Director,
Associate Professor
University of New Hampshire
Department of Earth Sciences

Dr. Jesse McNinch, Chief Science Officer
Sealaska Cooperation

Dr. Ryan Mulligan, Associate Professor
Queen's University
Department of Civil Engineering

Dr. Diane Foster, Director
School of Marine Science and Ocean Engineering
University of New Hampshire

Dr. Larry Ward, Research Associate Professor
University of New Hampshire
Department of Earth Sciences

On Tuesday, May 4, 2021

Original approval signatures are on file with the University of New Hampshire Graduate School.

DEDICATION

To my mom, for unwavering love and support, and the natural world, for hanging in there
while we figure it out.

ACKNOWLEDGEMENTS

Any success I have found during my doctoral degree is credited to my colleagues, friends and family – it was a privilege to have your support during this time of thinking about the questions I wanted to think about. I was blessed with an incredible advisor, Dr. Tom Lippmann; I would never have come to UNH 8 years ago if it were not for visiting on your advice and I have thoroughly enjoyed working together ever since. I was equally blessed to have the support of Dr. Jesse McNinch, a co-advisor, mentor, and good friend. The moments where your vision astounded me are too many to count. I am filled with gratitude for the guidance and trust you have both shared with me.

I was also blessed with an ideal committee: Ryan, your brilliance is balanced by your kindness and I look forward to working together in years to come. Thank you, Diane, for sharing your wisdom and expressing your confidence in me. You helped me to round out my work and grow as an educator. And thank you Larry, for your humor and geologic insights over the years; they kept me grounded.

And finally, I would like to sincerely thank my friend Salme for her support throughout my degree. From office banter to travelling to North Carolina to support my work to talking me through the deeper challenges of life – it was everything. There are countless others who supported me in all sorts of ways: Mom, Nate, Ben, Ellen, and Noah, Heidi Wadman, Scott Lemos, Bekah Coleman, Nick Brown, the Seacoast Paddleboard Club, Maddie Smith, Gail Hanlon, Lil's, Earth Eagle Brewings, Nick Cohn, Dan Freer, Alex Renaud, Patt Dickhudt, Kent Hathaway, Jeff Waters, Jeff Gough, Kate Brodie, the FRF field team, the CCOM IT team, and many others.

PREFACE

The coastal zones of this planet possess immense natural value. Filled with nutrients and life ranging from fields of marine vegetation to large schools of fish and apex predators, coastal waters are a natural sanctuary for life, and the adjacent lands may be equally prosperous. For example, the seasonal grasses of a coastal salt marsh form one of the most efficient systems for carbon sequestration on the planet. It is no surprise then that humans have also thrived along the coasts. The abundance of food, fertile lands and transportation passages in these areas were a significant catalyst for the rise of human civilizations and they remain at the epicenter today. Forty percent of the global population lives near the coasts in areas that compose just 10 percent of total land cover and the value of goods and services related to global coastal ecosystems is estimated to surpass \$33 trillion per year (Costanza et al., 1997).

However, recent decades have shown that the rigid style of modern human development along coasts often clashes with the natural dynamics of these environments. A measure of this may be seen in the hundreds of billions of dollars spent in the United States each year to respond to natural coastal disasters, and these costs are quickly trending towards the \$1 trillion dollar per year mark due to the effects of a warming climate. As sea levels continue to rise, more and more coastal infrastructure will become vulnerable along thousands of miles of coastline. The financial cost of protecting these developed areas, even during quiescent conditions, will surely rise into the trillions of dollars, and still the solutions will be temporary and the safety of people inhabiting these areas will not be guaranteed.

Despite the severity of these imminent challenges, it may be argued that far too little is

being done to prepare, and in some cases, the situation is being willfully exacerbated: dunes are being breached to install luxury homes, wetlands are being drained for industrial complexes, and roads and parking lots are replacing coastal vegetation. The harsh ramifications to come from these dubious decisions seem clear, but a pervasive mindset remains that would believe all environmental challenges will eventually be solved by technological innovation. The idea is not absurd, and seems almost grounded in three centuries of time where it has seldom failed. Still, it is worth considering that "those three centuries represent a tiny and very unusual fraction of humanity's trajectory on this planet" (Greer, 2011).

Many modern technologies and engineering practices are designed to deflect and prevent coastal processes that would endanger coastal infrastructure. Realistically, these efforts may at best defer these processes taking hold. With the force of a warming planet feeding them, the strength of coastal processes will continue to swell like a wave, and if not addressed, they will deliver a time of traumatic reckoning. A real solution may be realized only when the methods of human development are altered to fit within the natural dynamics of coastal environments. This means that, even while all efforts are taken to curb carbon emissions and slow anthropogenic climate change, it must be earnestly considered that some coastal areas are no longer suitable for permanent infrastructure.

There are portions of the Outer Banks, a barrier island system located off the coast of North Carolina, USA, that seem to fit this bill. The most vulnerable segments of the island chain sit nearly 50km offshore in hurricane prone Atlantic waters where storm waves and surges frequently wash over the island. Bulldozers often sit poised along NC route 12 prepared to remove thousands of tons of sand from the sole evacuation route and rebuild a thin and rapidly decaying artificial dune (Figure 1). In spite of hundreds of millions of dollars spent to manually rebuild the eroding island, multiple blocks of houses have fallen into the sea. Future efforts aim to defy these natural forces at yet greater cost, but there are enough indicators to suggest this situation is beginning to spiral out of control. To understand why and to find a better path forward, we must learn from the past.

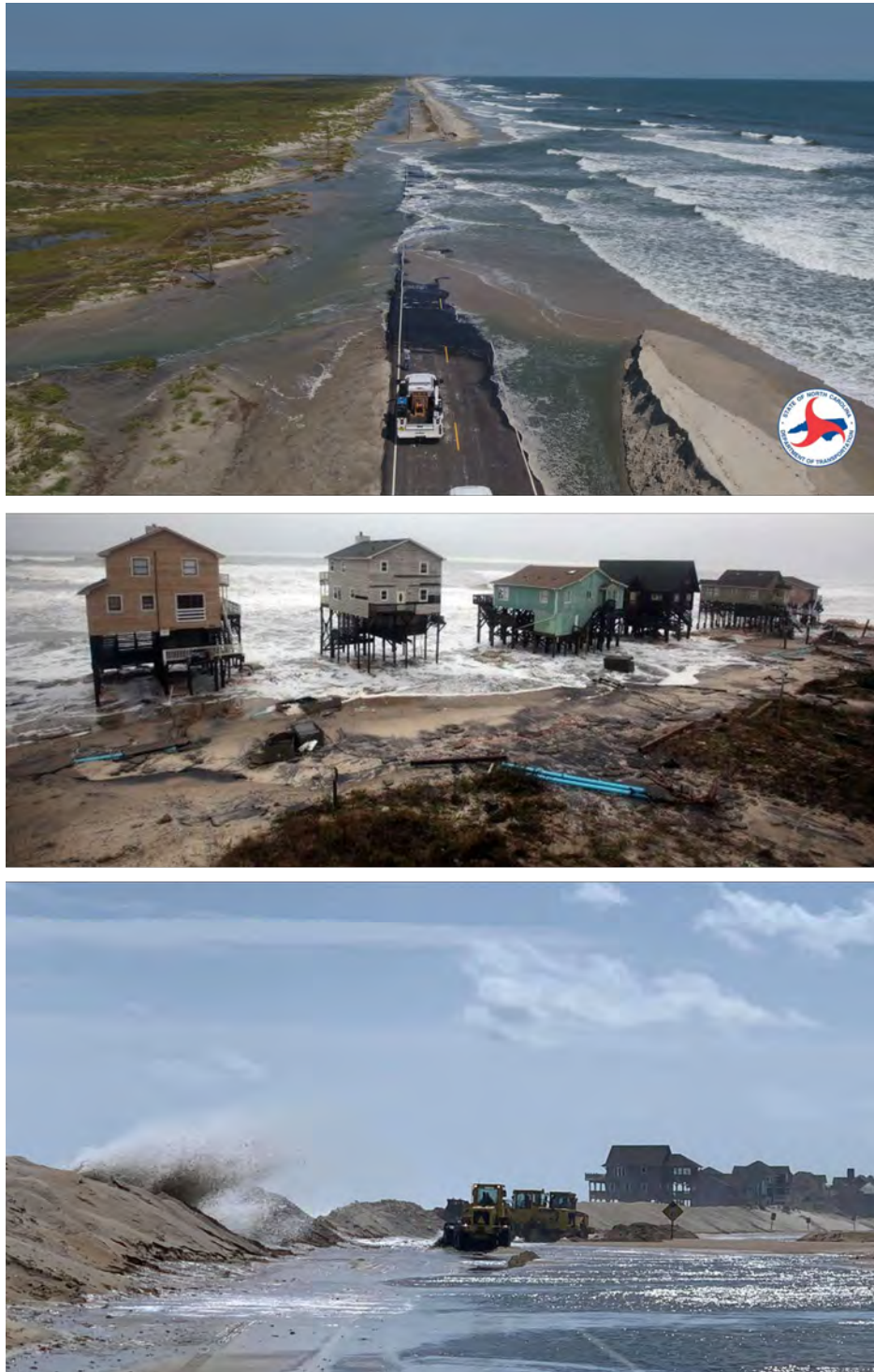


Figure 1: Top, a section of NC12 is easily washed out as the artificial dune is over-washed by large waves and a storm surge (Source: Coastal Review). Bottom, a few of many houses in Nags Head on the Outer Banks that could not be protected from coastal erosion (source: The Virginia-Pilot).

Barrier island systems, like most natural systems, must evolve to reach a dynamic equilibrium with the forces acting on them. Geologic records show that barrier islands, like those forming the Outer Banks, may be maintained even during periods of sea level rise by migrating landward via wave driven wash-over events and inlet migration. It is crucial that these processes occur if the system is to continue to exist in the face of rapidly evolving environmental forces. Unfortunately, this is paradoxical to the human perspective that sees these forces as entirely destructive, though this is but short-sightedness. It will be a great mistake if people seek at all costs to resist coastal change. Our greatest efforts will either fail or cause coastal systems to fail. Instead, we must adopt a different approach. We must endeavor to better understand why and how coastal systems evolve and use that knowledge to reinvent our coastal development strategy. The following research on coastal processes and evolution was conducted in support of this approach.

TABLE OF CONTENTS

DEDICATION	iv
ACKNOWLEDGEMENTS	v
PREFACE	vi
LIST OF FIGURES	xiii
ABSTRACT	xxii
1 Introduction	1
1.1 Coastal environments	1
1.2 Coastal Observations	2
1.3 Numerical Modeling	6
1.4 Barrier Islands and Tidal Inlets	8
2 Observations of wave influence on ebb-tidal delta shoals using a newly developed X-Band radar system	15
2.1 Abstract	15
2.2 Introduction	16
2.2.1 Remote sensing of bedforms	17
2.2.2 Geographic Setting	20
2.3 Wave induced longshore sediment transport	22
2.4 Methods	23

2.4.1	X-Band Measurements	23
2.4.2	Morphodynamic analysis	27
2.4.3	Longshore Sediment Transport	30
2.5	Results	30
2.5.1	Bedform Migratory Patterns	30
2.5.2	Alongshore forces acting on an ebb-tidal delta	33
2.6	Discussion	35
2.6.1	Wave Forcing	35
2.6.2	Longshore transport	37
2.7	Conclusions	39
2.8	Acknowledgments	40
3	Regional winds substantially influence tidal inlet currents at Oregon Inlet, NC	41
3.1	Abstract	41
3.2	Introduction	42
3.3	Methods	47
3.3.1	Data	47
3.4	Force Balance	57
3.5	Discussion	62
3.6	Conclusions	67
4	Idealized simulations of tidal inlet morphologic responses to wave, sub- tidal water level gradients and engineering modifications	69
4.1	Abstract	69
4.2	Introduction	70
4.3	Methodology	72
4.3.1	Domain Setup	73

4.3.2	Model Configuration	73
4.3.3	Model Scenarios	77
4.4	Results	77
4.5	Discussion	82
4.6	Conclusions	91
5	Conclusions	93
5.1	The story of Oregon Inlet	97
5.2	Insights from this work	100
5.3	Closing Remarks	104
	LIST OF REFERENCES	106
A	Sensativity to different wave angle observations near Oregon Inlet	123

LIST OF FIGURES

1	Top, a section of NC12 is easily washed out as the artificial dune is over- washed by large waves and a storm surge (Source: Coastal Review). Bottom, a few of many houses in Nags Head on the Outer Banks that could not be protected from coastal erosion (source: The Virginia-Pilot).	viii
1.1	Argus video cameras in Noordwijk aan Zee - from coastalwiki.org	3
1.2	By incrementing the time (t) in equation 1.1, the wave crest (denoted by the black dot) in the surface water level η propagates in the positive x direction in this simple numerical model.	7
1.3	A barrier island systems off the coast of North Carolina, USA (Left) is in a wave dominated region and shows elongate islands while, a barrier island system off the coast of the Netherlands (Right) in a more tidally controlled region exhibits 'drumstick' shaped islands. (Source: Google Earth)	9
1.4	A generalized schematic of the morphology and components of a tidal inlet [from Hayes and FitzGerald 2013.]	12
1.5	An early theory on how sediment bypassed a tidal inlet [from FitzGerald 1982; Hayes 1980.]	12
1.6	Oregon Inlet, NC is a notoriously challenging inlet to transit, with waves at times breaking around the full parameter of the ebb-tidal delta. There have been many vessels capsized or grounded. (Sources: http://outerbanksvoice.com , carolinadesigns.com)	14

2.1	(Top-left panel) The Outer Banks are located along the U.S. East Coast. (Top left panel) Oregon Inlet is located along the northern Outer Banks between Bodie Island (to the North) and Pea Island (to the South). The regional shoreline orientation is marked by a dashed black line. (Top right panel) In this Satellite imagery of Oregon Inlet, the bridge spanning the inlet may be seen, as well as wave breaking around the perimeter of the ebb-tidal delta. The position of a RIOS during this study and the Oregon Inlet Marina tidal gauge are marked.	21
2.2	A Radar Inlet Observing System (RIOS) at Oregon Inlet, NC in 2019. For this deployment, RIOS was powered completely by the solar panels and the wind turbine. Guy wires stabilized the radar antenna on a telescoping stand to minimize movements from wind.	24
2.3	(Top panel) An example of the relative x-band backscatter from a single antenna rotation (which takes place over approximately 1.2s) at Oregon Inlet. The intensity of the return signal represents the near instantaneous wave shoaling and breaking patterns. (Middle panel) The average backscatter intensity from a 10-minute (512 rotation) collection. (Bottom panel) An example 25 hour filtered product of the 10-minute average intensities used to smooth the lateral shifts in wave breaking due to tides.	26
2.4	(Left panel) Predetermined locations where timestacks were created. The black lines show an example of the cross-shore and longshore orientation and reach of the timestacks. Timestacks overlap 50% with the next timestack in each direction so that bedform paths extending off the edge of one may be marked in their entirety in the adjacent timestack. (Right panel) Starting locations of bedforms migratory paths picked within timestacks. X (cross-shore) and Y (alongshore) oriented timestacks were differentiated as they did not necessarily depict the same bedform.	28

2.5	An example of a cross-shore oriented timestack. The colormap represents the averaged backscatter intensity in which peaks represent the location of a bedform. The zoomed in subset shows an example area of the manually picked bedform path through time (magenta), the path interpolated only during period the radar was active (black) and the path picked by applying a local maxima filter (green).	29
2.6	Temporally averaged direction and relative magnitude of bedform movements (green arrows) for a period from 16 November 2016 to 01 April 2017. Migration patterns and rates were obtained using an optical motion tracking algorithm on successive 25-hour averaged intensity images. The red dots mark the location of the channel marker buoys which introduce artificial migration indicators in their immediate vicinity. Letters mark areas of interest (see text for explanation).	31
2.7	Spatially averaged alongshore bedform migration rate (red; left axis), and estimated wave driven alongshore sediment transport from the Ashton and Murray (2006) derivation (blue; right axis).	34
2.8	Time lagged cross-correlation between the spatially averaged alongshore bedform migration time series and the estimated wave driven alongshore sediment transport. Maximum correlation is 0.65. 95% confidence intervals are shown with the dashed gray lines (computed using the long-lag artificial skill method of Davis (1976)).	34
2.9	Alongshore bedform migration distances of all the bedforms depicted in the timestacks (gray lines), and the average alongshore location of all bedforms over time (bold black line).	35

2.10	Time series of the cumulative average longshore bedform movement magnitude (solid black line; left axis) and its linear trend (dashed black line), and the cumulative estimated alongshore sediment transport (solid red line; right axis) and its linear trend (dashed red line).	36
2.11	Estimated wave driven alongshore sediment transport rate from the Ashton and Murray (2006) formulation (Equation 2.2) during a year long period from 20 October 2016 to 20 October 2017. The orange line shows the period during which RIOS was deployed and the blue shows the remaining portion of that year. Transport directions are predominantly N-to-S during the late fall, winter and early spring months and S-to-N during the later summer and early fall months.	38
3.1	(left) The study site is located at Oregon Inlet along the Outer Banks, NC, a large spit and barrier island system on the U.S. mid-Atlantic coast highlighted by the dashed red box. (right) The inlet, in the dashed red box, is the northernmost of 3 inlets that connect the Atlantic Ocean to the large Pamlico sound.	45
3.2	The Oregon Inlet field site with bathymetry relative to the NAVD88 vertical datum (approximately MSL), surveyed in March 2019, shown within the dashed gray line. An ADCP with pressure sensor was deployed on the ocean side of the inlet within the main inlet channel (yellow triangle), and an AWAC with pressure sensor was placed on the sound side of the inlet (green diamond). A spotter wave buoy was moored offshore of the ebb-tidal delta (magenta star) and a meteorological station was located at the Oregon Inlet Marina (red star). The red arrow indicates the orientation of the main ebb channel (13° rel. true north) and the orientation of the positive x-axis used in data analysis and force balance.	49

3.3	Time series of observed wind speeds (top) and directions (middle) over the 40-day study period. (Bottom) A wind rose shows the dominant wind directions during the experiment	51
3.4	The Ocean side observed current magnitude (top) and direction (2nd from top) and the Sound side observed current magnitude (3rd from top) and direction (4th from top) for the 40-day study period.	52
3.5	Observed (thin lines) and filtered subtidal (thick lines) time series. Water levels for the ocean side ADCP (top) and from the sound side AWAC (2nd from top). Along-channel current speed for the ocean side ADCP (3rd from top) and sound side AWAC (4th from top). Along-channel wind speed from the meteorological station at Oregon Inlet Marina (5th from top). Significant wave heights (bottom) from the offshore waverider buoy (black line), the spotter buoy just seaward of the ebb-tidal delta (dotted black line), and the sound side AWAC (dashed black line), with the subtidal signal shown only for the waverider buoy timeseries.	54
3.6	Subtidal time series for the along-channel wind speed (top), STWL gradient (2nd from top), and ST currents from the main channel ADCP (3rd from top), and the raw significant wave height time series (bottom).	56
3.7	Time-lagged cross correlation between the along-channel component of wind speed and the sub-tidal water level gradient (solid), between the along channel component of the wind and the sub-tidal ST current (dashed gray), and between the sub-tidal STWL water level gradient and the along-channel component of the ST current (dot-dashed light gray).	58

3.8	Time series of the observed along-channel ST current (black solid line), and the predicted current based on a force balance using the STWL pressure gradient without wind drag incorporated (dashed blue line), and the predicted current based on the STWL pressure gradient including the surface wind stress (red dashed line).	61
3.9	Observations during storm waves with strong winds out of the north (upper panel). Time series of STWL pressure gradient (blue line) and offshore significant wave height (orange line) as measured by a wave rider buoy (NDBC station 44095). (lower panel) Time series of wind direction with wind speeds indicated by the color scale on the right-hand-side.	63
3.10	Observations during storm waves with strong winds out of the south (upper panel). Time series of STWL pressure gradient (blue line) and offshore significant wave height (orange line) as measured by a wave rider buoy (NDBC station 44095). (lower panel) Time series of wind direction with wind speeds indicated by the color scale on the right-hand-side.	64
3.11	(left) STWL gradient as a function of the along-channel wind velocity. Linear regression is shown by the dashed black line with R^2 value of 0.74. (right) The observed current as a function of the water level gradient only associated with astronomical tides (blue; $R^2=0.49$), and as function of the water level gradient that includes tides and the wind-forced STWL gradient from wind forcing (red; $R^2 = 0.88$).	66
4.1	The synthetic domain extends 18km in the y-direction and 18km in the x-direction. There is a 3m deep sound on the west side, separated from the ocean on the East side by a 300m wide and 3m tall island with an inlet centered in the y-direction	74

4.2	An initial synthetic topo-bathymetric surface was constructed and divided into 8 sub-domains of varying resolution for application of domain-decomposition in D-3D.	76
4.3	The initialized topo-bathymetric surface was used as a starting bathymetry to simulate a control scenario and 3 test scenarios. The Control maintains the same forcings and setup as the initialization run and serves as a control. Scenario A is forced by waves on a 45° relative to north. Scenario B includes a sub-tidal oscillation forced along the sound-side borders. Scenario C includes a terminal groin along the northern terminus of the southern island.	78
4.4	In Scenario B, a sub-tidal water level forcing was applied to the sound-side boundaries. The signal consists of alternating positive and negative sinusoids occurring over 5 days with 5 days of zero forcing in between.	79
4.5	The topo-bathymetric surface and mean-total sediment transport patterns from the control Scenario.	80
4.6	Top, the topo-bathymetric surface and mean-total sediment transport vectors from Scenario A that included incident waves from 45° relative to North. Bottom, the difference in end-state topobathymetric surfaces and transport vectors between the control and scenario B. Note that warm colors indicate that Scenario B had a higher elevation (shallower depth) than the control.	81
4.7	Top, the topo-bathymetric surface and mean-total sediment transport vectors from scenario B that included a sub-tidal water level forcing on the sound side of the inlet. Bottom, the difference in end-state topobathymetric surfaces and transport vectors between the control and scenario B. Note that warm colors indicate that Scenario A had a higher elevation (shallower depth) than the control.	83

4.8	Top, the topo-bathymetric surface and mean-total sediment transport vectors from scenario C that included a representation of a terminal groin on the northern side of the souther land mass. Bottom, the difference in end-state topobathymetric surfaces and transport vectors between the control and scenario C. Note that warm colors indicate that Scenario C had a higher elevation (shallower depth) than the control.	84
4.9	Left, a zoom of the results of Scenario C, where the purple line represents the position of the infinitely thin dam used to simulate a terminal groin. Right, a zoom in of Oregon Inlet focused on the terminus of the southern island that is maintained by a terminal groin. This satellite image was collected in 2006.	89
4.10	From top to bottom, 3 aerial images of Oregon Inlet from 1979, 1989, and 1996. The shorelines of each are marked for the year the image was collected as well as in all subsequent images.	90
5.1	A schematic of barrier island system from Reinson (1992). The islands are composed primarily of sand forced landward by wave action, and overlay back barrier marsh material from a previous period of lower sea level. The island is marked by a tidal inlet and washover events and shelters the back barrier marshes and mud flats.	93
5.2	Top, a schematic of a incremental shift in barrier island position associated with a rise in sea level. Bottom, a schematic of the long term migration of a barrier island into the back bay due to rising sea levels. . From (Rosati, 2009; Zecchin et al., 2019)	94
5.3	Top, a major breach of the Outer Banks near the town of Hatteras caused by Hurricane Isabel, 2003 (photo: US Geological Survey). Bottom, destruction near the town of Rodanthe on the Outer Banks caused by Hurricane Irene (2011) that devastated more than 1,100 homes in the state, costing \$70 million in damages. (photo: REUTERS)	95

5.4	A satellite image of Oregon Inlet, NC that shows the expansive flood-tidal delta channels and shoals, the condensed flood-tidal delta, the terminal groin, and the nearby beach faces.	98
5.5	As a recurring spit intrudes upon the navigation channel, a single hopper dredger attempts to clear the channel through the only navigation span of the Bonner Bridge.	99
5.6	Top, the construction of the new Marc Basnight Bridge that spans Oregon Inlet. Bottom, the completed March Basnight Bridge (left) next to the the old Bonner Bridge (right) before its removal.	101

ABSTRACT

Wind, Wave, and Engineering Effects on Tidal Inlet Morphodynamics

by

Joshua L. Humberston

University of New Hampshire, May, 2021

This body of work examines the hydro- and morpho-dynamics of tidal inlets using a diverse array of research tools. A custom X-band radar system (RIOS) is designed and used to track the evolution of shoal features over the ebb-tidal delta at Oregon Inlet, NC. Analysis of the data reveals that alongshore shoal migration rates are closely correlated to wave driven along-shore sediment transport, and also that the cross-shore bedform migration rates are tightly correlated with a sub-tidal water level gradient through the inlet. A follow up experiment with in-situ sensors suggests that the sub-tidal gradient is set up by regional winds and that the resulting pressure gradient significantly alters the tidal inlet hydrodynamics, at times entirely reversing tidal flows. Finally, the geomorphic impact of wind driven currents, as well as waves and the insertion of a terminal groin, is tested through an idealized numerical modeling study of a synthetic inlet system. The addition of a sub-tidal water level gradient has substantial and cascading effects on the inlet system morphology, potentially suggesting that the traditional inlet classification system, based only on wave and tidal properties, should be modified to include wind influence.

CHAPTER 1

Introduction

1.1 Coastal environments

The intersection of land, water and atmosphere defines the coastline, but there is enormous variability in what this may look like. In the northeast United States, the coastal environment is typically rocky, with occasional pocket beaches and inlets that connect the ocean to inland water bodies and marshes. Further south on the US eastern seaboard, the coastal systems transition into sandy and dynamic barrier islands that enclose large bays and sounds where fish and other marine species lay their eggs and swarms of migrating birds spend their time. There is yet greater coastal diversity existing around the world: the extensive Great Barrier Reef in Australia, the turbid waters of the Amazon River Mouth in South America, the icy shelves of Antarctica and Greenland, the rugged cliffs on the American West Coast, and the sprawling mud flats and permafrost of Canada.

The diversity of these systems stems from the full spectra of coastal processes that shape them, from microscopic turbulent eddies that dictate the motions of individual particles to the millennial scale climatic trends that alter sea levels. Just a few of the myriad other factors include sediment composition, latitude, historic plate tectonics, storm frequency and intensity, sediment supply, wave climate, regional topography, and plant growth, and this is to say nothing of human impacts. For coastal studies, the complex interactions of these processes makes it challenging to understand even a small coastal area at a solitary point in time. Perhaps this is why, in spite of a rich framework of governing physical equations, it has remained tremendously difficult to predict coastal behavior. Even the most catered

combination of theoretical formulations will explain only a small and brief idealized instant in space and time before external factors render it obsolete. As a result, the community of coastal scientists and engineers has turned to innovative methods for measuring and understanding coastal processes and evolution.

1.2 Coastal Observations

The recent age of technological advancement has led to a precipitous increase in observational tools for coastal studies. Existing instruments have been reinvented to reduce costs, make better measurements, and operate in swarm deployments. Recent decades have also seen a rapid expansion of remote sensing technologies that provide unique ability to make observations over a swath of area from a distance.

While many remote sensing advancement have been catered to satellite observations, coastal studies require knowledge of micro- to meso-scale processes that can not be imaged in adequate spatial or temporal resolution by most satellite sensors. Instead, a number of remote sensing instruments utilizing various portions of the electromagnetic spectrum have been developed or adapted from other uses to make measurements of coastal regions at these scales. One of the most common tools is locally collected optical data (video imagery) with higher spatial and temporal resolution that may be obtained from a satellite. The Argus video monitoring system has been at the forefront of this methodology and typically utilizes multiple high definition camera systems and a back end processing computer to georectify the imagery (Figure 1.1).

In contrast to in situ surveys, video and other coastal remote sensing techniques excel in highly energetic sea states because they utilize the disturbances associated wind roughness and surface wave propagation to derive other valuable parameters (Holman and Haller, 2013; Hessner et al., 2014; Pianca et al., 2014). For example, time-averaged optical observations of wave breaking appear as higher intensity signals that have been used as a direct proxy for the morphology of the underlying bathymetry (Lippmann and Holman 1989, and many



Figure 1.1: Argus video cameras in Noordwijk aan Zee - from coastalwiki.org

others). Sequential time-averaged images can also be used to estimate the evolution of the morphology provided a continuous detectable surface signature is captured (Lippmann and Holman, 1990).

Additional information about bathymetry may also be extracted in post processing. As surface waves transition from deep to shallow water, they begin to shoal; celerity and wavelength are reduced while wave steepness increases. Eventually, wave steepness exceeds a critical threshold and wave breaking occurs (Munk, 1949; Thornton and Guza, 1983). Time series of pixel intensity can be used to estimate wavenumbers and frequencies of the surface waves that vary with these processes, and consequently used to infer the underlying bathymetry (e.g., Williams, 1947). C-bathy is a well-accepted algorithm for this purpose (Holman and Haller, 2013; Radermacher et al., 2014; Bergsma et al., 2016).

Video imaging has and continues to be a valuable tool for coastal studies, especially as post-processing has improved to derive ever more information from the original images, but it too has limitations. Video data cannot be collected at night and may be distorted by meteorological conditions such as rain and fog – a major shortcoming during storm events. It can also be a large undertaking to place the cameras at a sufficient elevation to obtain the visual ranges desired (Holman et al., 1993).

Another approach is Light Distance and Ranging (LiDaR) which is a technology that uses an active light signal (ranging between the ultraviolet, visible and near infrared frequencies) to measure the distance of targets from the sensor. This may be done from a single source, but the technology has also evolved to allow arrays of light sources on a rotating platform to capture 3-D georeferenced landscapes, typically within 1km of the sensor to maintain eye-safe light levels. These sensors may be placed at a stationary location, or, when paired with a GPS and Inertial Motion Unit (IMU), on a vehicle such as a car, marine vessel or airplane. While generally expensive, this capability is highly valuable for quantifying topographic or water features and has been used for this purpose in numerous coastal studies (Lillycrop et al., 1996; Stockdon et al., 2002; Sallenger Jr et al., 2003). High costs have often been a

prohibiting factor for LiDaR, but they continue to decrease as LiDaR technology has entered the broader market for uses in "smart cities" and "autonomous cars." Still, for coastal studies, a limiting factor for LiDaR observation is turbid water that may prevent bottom detection. This makes it difficult to acquire long time series of inlet bathymetry and bedform locations at regular time intervals and on time scales of interest (Gao, 2009).

Yet another method for remotely sensing coastal environments is X-band radar. These sensors emit and receive a signal from the microwave band of the electromagnetic spectrum. Despite the difference in signal, X-band radar can often be used in a similar manner to video observations (Haller and Lyzenga, 2003). The backscatter of a microwave X-band signal from long waves like those on the ocean surface is well modeled by the Composite-Surface Model (CSM) that acts on the Bragg scatterers (Bass et al., 1968; Wright, 1968; Catalán et al., 2014). The backscatter also increases as waves shoal and the angle of incidence is reduced (Lee et al., 1995). As waves break, they produce a highly roughened and near-oblique target, further increasing backscatter (Catalán et al., 2014). The resulting interaction between the X-band signal and the surface has been demonstrably useful for making oceanographic measurements in the nearshore region (Phillips, 1988; Barrick, 1972; Donelan and Pierson Jr, 1987; Trizna, 1997). Compared to visual band observations, X-band radars tend to lack the spatial resolution necessary to resolve multiple frequency peaks in the wave field which, according to the CSM, is due to long wave modulations limiting the observed signal of shorter waves. Still, multiple studies have successfully demonstrated inversion techniques including the application of C-bathy (Bell, 1999, 2002; Holman and Haller, 2013; Hessner et al., 2014; McNinch, 2007; Catalán and Haller, 2008).

X-band radar sensors have the attractive attributes that they can be used during day and night time periods, and that radar antennae deployments do not require high elevation platforms. Rotating radars can acquire backscatter measurements over circular regions with diameter in excess of 5 km and with 5 m or better resolution. Because radar systems can be used to sample large surface areas in nearly all-weather conditions, they have become

increasingly effective research tools in coastal environments, particularly for examining larger scale coastal behavior and sea surface processes

The application of these novel observational tools have shed new light on the previously unappreciated spatial variability of coastal processes. Bathymetry, surface and sub-surface material variations, water properties, wave and current characteristics can now be measured in much greater resolution and precision than was possible a few decades ago. However, some of these advancements have raised as many new questions as they have answered old ones. There are complex and sometimes unexpected hydro- and morpho-dynamics patterns and it remains difficult to define causal relationships from observations alone.

1.3 Numerical Modeling

To this end, numerical models have become a ubiquitous tool for nearly all scientific studies. Even within earth sciences, there is a great assortment of numerical models for different applications. Still, most models for earth sciences are fundamentally the discretized mathematical representation of physical processes. This generally includes a temporal dependency that allows the topic of interest to evolve in response to the governing equations over time.

For example, the equations for surface water level (η) based on Linear Wave Theory may be turned into a simple 2-D numerical model by incrementing the time term (t) in equation 1.1. Given other constant parameters for wave amplitude (a), wave number (k), orbital velocity (ω), and an array locations on the x-axis (x), incrementing the time variable simulates a wave moving through space over time (Figure 1.2). This is, of course, a highly simplified model; most coastal studies now use complex numerical models spanning 3 dimensions and various mediums.

$$\eta(x, t) = a \sin(kx - \omega t) \tag{1.1}$$

While early models were acutely limited by computational power and inadequate param-

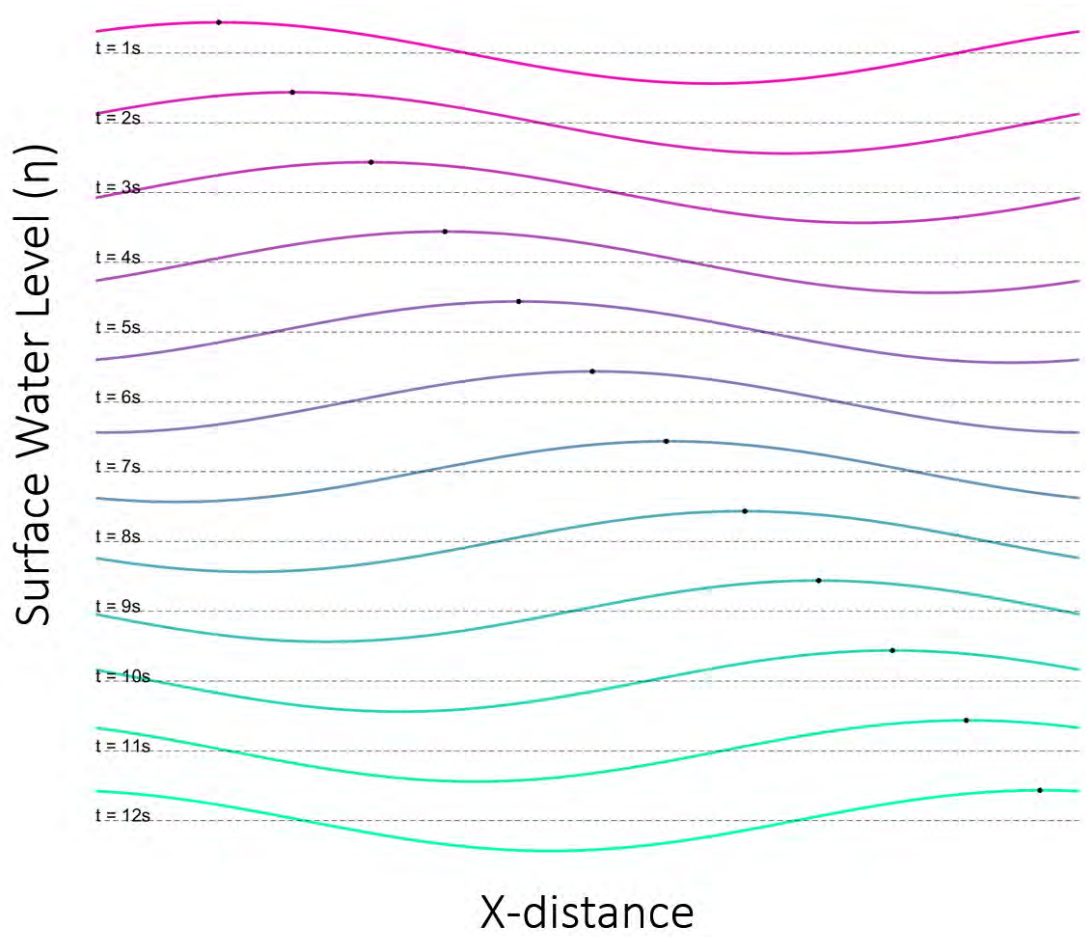


Figure 1.2: By incrementing the time (t) in equation 1.1, the wave crest (denoted by the black dot) in the surface water level η propagates in the positive x direction in this simple numerical model.

eterizations, both computers and models have now been developed to a level sufficient for producing useful approximations of real-world processes. Hind-casting models can be paired with observations to validate the model results and then better grasp 2- or 3-dimensional processes only ambiguously captured by point observations. Another major benefit of numerical modeling is the ability to run simulations into the future and predict likely future states. This remains an area of active research, especially for morphodynamic modeling, but ever improving efforts to run ensembles of simulations and assimilate real-time data are quickly improving the accuracy of near term predictions.

1.4 Barrier Islands and Tidal Inlets

Remote sensing development and numerical models have become capable tools for studying earth processes, and these new tools are desperately needed. Innumerable environments, coastal and otherwise, that will be inextricably altered by the effects of anthropogenic climate change. This body of work focuses on barrier island systems that are particularly vulnerable to changing water levels. Specifically, the research explores tidal inlets, the features that separate the islands from each other and the mainland. Barrier islands are a relatively common coastal features that are estimated to span 10% of the world's coastlines (Stutz and Pilkey, 2001), yet mystery remains in how they evolve and why they exist in the first place. The three foremost proposed mechanisms for barrier island formation include, "(1) upbuilding of offshore bars; (2) cutting of inlets through spits; and (3) submergence of ridge like coastal features (Schwartz, 1971). There have been strong proponents of each method over the years (Bird, 1969; Shepard, 1999; Hoyt, 1967), but the current consensus seems to be that barrier islands may form from any or an amalgamation of all three processes (Davis, 1994; Otvos, 2020).

Whatever the underlying cause of formation, it is clear that barrier islands may take on many different forms. In a seminal piece of work, Hayes (1979) proposed a classification system for barrier island morphology based on the relative strength of waves and tides in

a region. In a wave dominated environment, barrier islands tend to be thin and elongated with washover processes limiting the width (Davis, 1994; Hayes, 1979). In contrast, the tidal energy limits the size of barrier islands in meso-macro tidal regions and results in shorter and more bulbous shaped islands (Hayes and Kana 1976 –Figure 1.3). In areas with very large tidal ranges, there are rarely any barrier islands due to the tidal forces and the width of wave breaking activity over a tidal cycle.

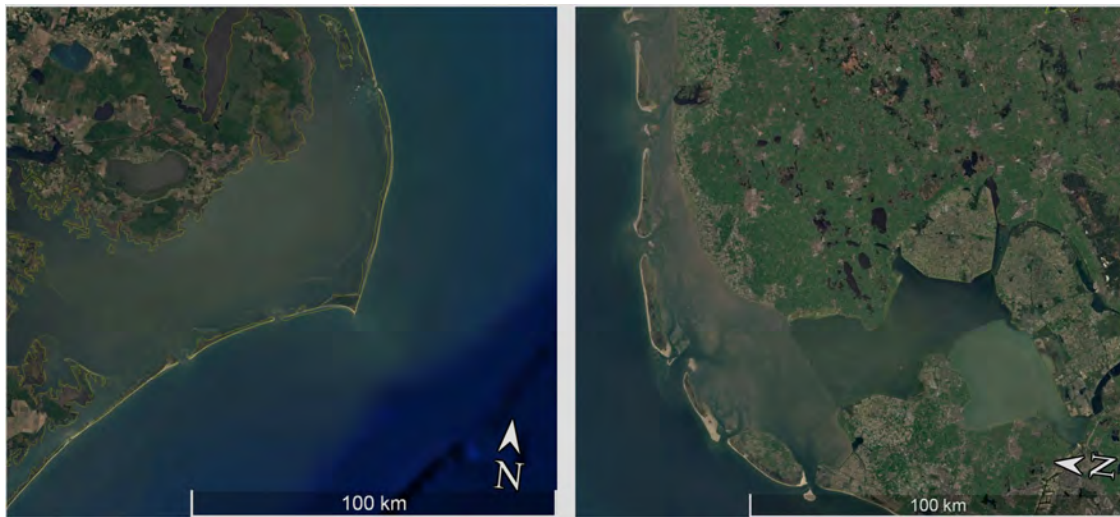


Figure 1.3: A barrier island systems off the coast of North Carolina, USA (Left) is in a wave dominated region and shows elongate islands while, a barrier island system off the coast of the Netherlands (Right) in a more tidally controlled region exhibits 'drumstick' shaped islands. (Source: Google Earth)

Of course, barrier islands systems are defined as much by the channels of water between islands as they are by the islands themselves. These channels, known as tidal inlets, were defined by FitzGerald and Buynevich (2003) as "an opening in the shoreline through which water penetrates the land thereby providing a connection between the ocean and bays, lagoons, marsh, and tidal creek systems." It was also noted that, "tidal currents maintain the main channel of a tidal inlet," which differentiates them from other coastal channels composed of rock or hard materials. As such, tidal inlets are generally dynamic, evolving as tides and currents shift their sands. Often, asymmetric alongshore sediment transport patterns will causes an inlet to migrate laterally along the coast.

Tidal inlets can exist around the world in a range of coastal environments but are especially common along barrier island systems and other sandy shorelines where they may originate due to storm driven overtopping and scouring processes (FitzGerald and Pendleton, 2002). Breaches may naturally close off due to sediment transport into the channel, however, if the breach forms a hydrodynamically efficient route for tidal waters to flow between the ocean and inland water body, then it may become self maintaining and be considered a tidal inlet.

Tidal inlets are an important coastal feature because they often demonstrate control on the regional coastal environment beyond their immediate geographic footprint (Hayes, 1980; FitzGerald, 1988). For example, tidal inlets positioned at the seaward edge of an estuary or bay system will regulate the flux of water, nutrients and sediment into and out of the system and are therefore an important control of the systems overall ecologic health (Fulton et al., 1993). Tidal inlets are equally influential from a geophysical perspective as their cross-shore tidal currents disrupt alongshore sediment transport, temporarily or permanently storing large volumes of sediment in the flood and ebb tidal deltas (FitzGerald, 1982; Boothroyd, 1985; Walton and Dean, 2011; Legault et al., 2012). These disruptions may manifest as large scale erosional or accretional patterns over extended swaths of neighboring coastline (FitzGerald, 1988).

The main channel of tidal inlets and their landward connected water bodies also frequently serve as valued maritime passages and harbors for shipping traffic, fishing fleets and recreational boats. It is therefore necessary at many inlets to maintain a stable and navigable waterway while also preserving the natural longshore sediment exchange between adjacent shorelines. Efforts to unify the varied aspects of this challenge has driven extensive research focused on both natural and engineered inlets (O'Brien and Zeevaert, 1969; Hayes et al., 1970; Bruun, 1978; Hayes, 1980; FitzGerald, 1988, 1996; Elias et al., 2003; Fiechter et al., 2006; Pacheco et al., 2008).

There is a hydrodynamic constriction through the throat of an inlet that causes tidal cur-

rents to accelerate and scour bottom sediment. Much of this sediment will be transported to the areas adjacent to the inlet throat where the hydrodynamic constriction is relaxed. Here, the currents wane and sediment is deposited on large shoal features known as tidal deltas, one of the major features of interest in the following studies (Figure 1.4). At wave dominated inlets, early theories suggested that sediment bypasses inlets via swash bars migrating along a continuous path along the terminal lobe of the ebb-delta (Hayes and FitzGerald, 2013). This was of course an idealized representation; the actual patterns of transport were known to be far more complex and also to vary between inlets (Figure 1.5). Nonetheless, the underlying assumption remains intact: sediment transport is in the direction of bedform migration.

However, even today, the validity of this assumption have been difficult to examine in much detail. This is, in part, because there has been limited observational data of bedform morphodynamics and sediment transport over the scales of complexity existing at tidal inlet systems (Komar, 1996; Herrling and Winter, 2018). Understanding and predicting inlet sediment dynamics has proven difficult, largely owing to the forceful and complex interactions of waves and currents with the seabed that contribute to variations in formation and maintenance of channels and shoals (Aubrey, 1993; FitzGerald, 1996; Elias et al., 2003; Davidson-Arnott et al., 2019; Olabarrieta et al., 2011; Chen et al., 2015). Complicating the problem is that flood- and ebb-tidal deltas are generally superimposed with complex and highly variable bedforms ranging in scale from several to tens of meters (Hayes, 1980; Komar, 1996; FitzGerald et al., 2000; Pianca et al., 2014).

The challenges associated with making effective measurements of inlet hydrodynamics and morphology have remained over several decades. Strong currents confront breaking waves over the ebb-tidal delta, making any type of survey difficult and potentially dangerous (Figure 1.6). Additionally, even under calm conditions, a bathymetric survey of an inlet system is difficult, with depths ranging from 20m or more to exposed shoals over very short distances. Multi-beam surveys are often unpractical under these conditions as the

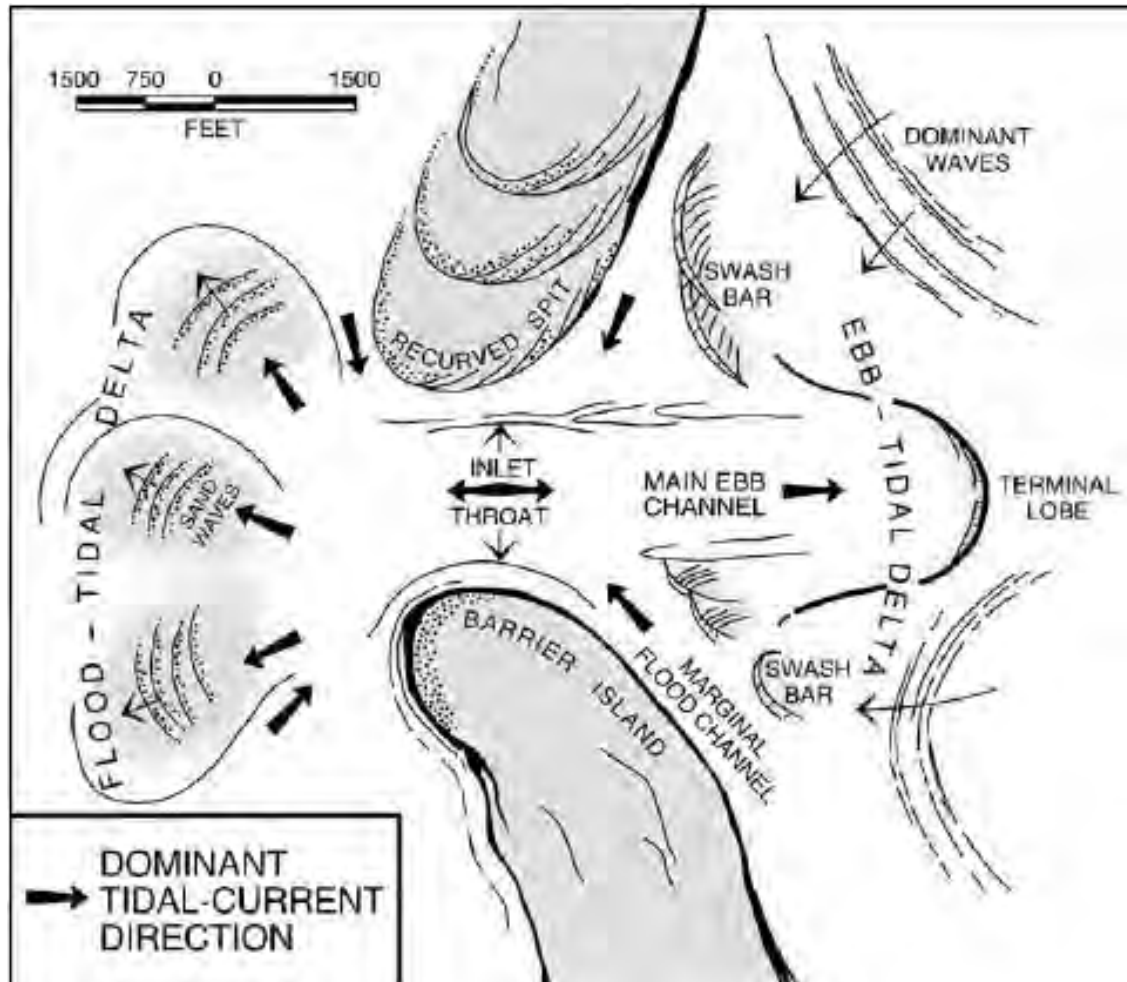


Figure 1.4: A generalized schematic of the morphology and components of a tidal inlet [from Hayes and FitzGerald 2013.]

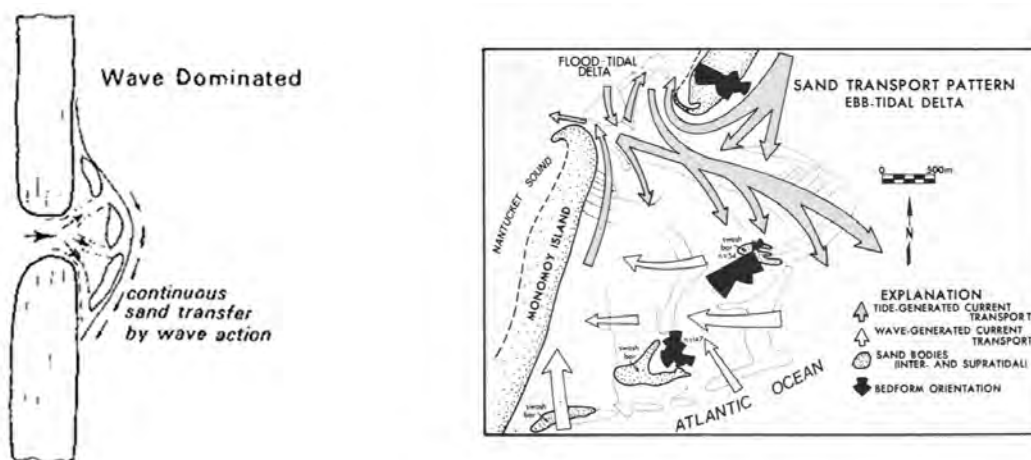


Figure 1.5: An early theory on how sediment bypassed a tidal inlet [from FitzGerald 1982; Hayes 1980.]

swath varies based on depth and full coverage would require many hours of surveying the shallows. Single beam surveys are somewhat easier to conduct, but will likely miss the complex bedforms existing between survey lines. And finally, even if great care and time is used to fully survey a tidal inlet system, the measured depths may not be valid for long; the bathymetry varies over tidal cycles and may go through dramatic rearrangements during storms. A single survey does not provide the necessary temporal resolution to understand morphologic evolution at a tidal inlet. Thus, remote sensing and numerical models are ideal tools for studying tidal inlet systems.

The following 3 chapters present studies of tidal inlets that use a combination of observational technologies and numerical models. These are paired with traditional in situ observations to make new insights into the forcings responsible for tidal inlet dynamics, and how these systems may be expected to behave under different future scenarios. Beyond satisfying scientific intrigue, it is this author's hope that these advances also prove useful for real-world applications including the development of future coastal engineering projects and infrastructure planning.



Figure 1.6: Oregon Inlet, NC is a notoriously challenging inlet to transit, with waves at times breaking around the full perimeter of the ebb-tidal delta. There have been many vessels capsized or grounded. (Sources: <http://outerbanksvoice.com>, carolinadesigns.com)

CHAPTER 2

Observations of wave influence on ebb-tidal delta shoals using a newly developed X-Band radar system

2.1 Abstract

The Radar Inlet Observation System (RIOS) collected hourly X-band radar data at the wave dominated Oregon Inlet, NC, for 9 months from September 2016 to May 2017. The intensity of the radar backscatter, predominantly associated with surface wave shoaling and breaking, was time-averaged to provide an implied measure of bedforms superimposed on the ebb-tidal delta. Eulerian and Lagrangian motion tracking analyses determined the bedform alongshore migration rates over the study period; these were found to be significantly correlated to estimates of longshore sediment flux based on offshore wave parameters given by Ashton and Murray (2006). Although the exact magnitude of sediment transport cannot be directly estimated from bedform migration, the correlation does support an underlying assumption that sediment transport varies proportionally in both magnitude and direction to average bedform movements at Oregon Inlet. The implications of these findings were further explored through application of the sediment transport model to a year long period of continuous offshore wave data (20 Oct 2016 to 20 Oct 2017). The predicted net transport of $90,000m^3$ southward during this year is consistent with a previous estimate of inlet bypassing (Dolan and Glassen, 1973). However, pronounced and opposing seasonal transport patterns were an order of magnitude higher than the yearly net, and could lead to significant inter-annual variability in alongshore sediment transport with similar dynamic response in ebb-delta morphodynamics.

2.2 Introduction

Tidal inlets and their associated delta systems are dynamic sedimentary coastal features that can change substantially on long (monthly to yearly) and short (individual storm) time scales and have the potential to significantly alter local sediment transport patterns (e.g., O'Brien and Zeevaert, 1969; Hayes et al., 1970; Bruun, 1978; Hayes, 1980; FitzGerald, 1988, 1996; Elias et al., 2003; Fiechter et al., 2006; Pacheco et al., 2008). However, understanding and predicting inlet sediment dynamics has proven difficult, largely owing to the complex interactions of waves and currents with the seabed that contribute to variations in formation and maintenance of channels and shoals (e.g. Aubrey, 1993; FitzGerald, 1996; Davidson-Arnott et al., 2019; Olabarrieta et al., 2011; Chen et al., 2015). Complicating the problem is that flood- and ebb-tidal deltas are generally superimposed with complex and highly variable bedforms ranging in scale from several to tens of meters (Hayes, 1980; Komar, 1996; FitzGerald et al., 2000; Pianca et al., 2014).

General tidal delta properties are categorized reasonably well from knowledge of local tidal magnitude, wave climate, and gross bathymetry (Hayes, 1980; Boothroyd, 1985). The mechanisms of delta evolution and sediment bypassing are less clear. At wave dominated inlet systems, classic theory suggests sediment bypasses the inlet via bedforms (referred to as swash bars) that migrate along a continuous pathway over the ebb-deltas terminal lobe (FitzGerald, 1982). The underlying assumption is that sediment transport is in the direction of bedform migration. The details of this process are not well constrained, at least in part because of limited observational data of bedform morphodynamics and sediment transport over the scales of complexity existing at tidal inlet systems (Komar, 1996; Herrling and Winter, 2018).

In this work, we examine patterns of implied bedform movements observed from remotely sensed time-averaged breaking patterns on the ebb tidal delta of the wave dominated Oregon Inlet. These patterns, quantified by a spatially averaged migration rate, are compared to

the alongshore sediment transport model of Ashton and Murray (2006). The study provides new observational evidence that alongshore bedform migration at the inlet is consistent with wave forcing that drives a net southerly sediment transport that bypasses the inlet, although with substantial seasonal variability. It should be noted that, while bedform morphology is generated by gradients in sediment transport, comparisons of bedform movements with sediment transport formulae are based on an implied assumption herein that sediment transport is in the direction of the bedform migration, an assumption made in many previous inlet and delta studies (e.g., Robinson, 1975; O'Connor et al., 2011; Pianca et al., 2014; Ridderinkhof et al., 2016; and others).

2.2.1 Remote sensing of bedforms

Breaking waves and rapidly changing shallow bathymetry at tidal inlets render most sonar surveys difficult, expensive, and their results of temporally limited relevance. Consequently, several alternative survey procedures have been developed to circumvent these issues, including remote sensing techniques based on optical, lidar, and radar measurement devices that have proven effective at acquiring evolutionary information in energetic inlet environments (Holman and Haller, 2013; Montreuil et al., 2014). Lidar (Light Detection and Ranging) observations from airborne platforms are valuable owing to their very high spatial resolution and rapid observational methods (Lillycrop et al., 1996; Stockdon et al., 2002; Sallenger Jr et al., 2003); however, costs may be prohibitive and turbid water can often prevent detection of bottom returns. This makes it difficult to acquire long time series of inlet bathymetry and bedform locations at regular time intervals and on time scales of interest (Gao, 2009).

Conversely, video (optical) and X-band radars capitalize on energetic sea states by measuring the surface disturbances associated with surface wave propagation independent of water clarity (Holman and Haller, 2013; Hessner et al., 2014; Pianca et al., 2014; Bergsma et al., 2016). As surface waves transition from deep to shallow water, they begin to shoal; celerity and wavelength are reduced while wave steepness increases. Eventually, wave steep-

ness exceeds a critical threshold and wave breaking occurs (Munk, 1949; Thornton and Guza, 1983).

Continuous recording with high-resolution video captures the optical surface reflection of wave shoaling and breaking processes. In post processing, time series of pixel intensity can be used to estimate wavenumbers and frequencies of the surface waves, and subsequently used to infer bathymetry using the dispersion relation (e.g., Williams, 1947) as demonstrated in commonly employed algorithms such as C-bathy (Holman and Haller, 2013; Radermacher et al., 2014; Bergsma et al., 2016).

In the nearshore, time-averaged optical observations of wave breaking appear as higher intensity signals. Historically, this has been used as a direct proxy for the morphology of the underlying bathymetry (Lippmann and Holman, 1989; and many others). Sequential time-averaged images can then be used to estimate the evolution of the morphology provided a continuous detectable surface signature is captured (Lippmann and Holman, 1990). A major limitation of optical techniques is that images can only be collected during daytime hours, and the range over which image resolution is reasonable is dependent on the height of the camera system (Holman et al., 1993).

X-band radars use a signal from a different band of the electromagnetic spectrum (8.012.0 GHz) but can often be used in a similar manner to video observations (Haller and Lyzenga, 2003). The backscatter of a microwave X-band signal from long waves like those on the ocean surface is well modeled by the Composite-Surface Model (CSM) that acts on the Bragg scatterers (Bass et al., 1968; Wright, 1968; Catalán and Haller, 2008). The backscatter also increases as waves shoal and the angle of incidence is reduced (Lee et al., 1995). As waves break, they produce a highly roughened and near-oblique target, further increasing backscatter (Catalán et al., 2014). The resulting interaction between the X-band signal and the surface has been demonstrably useful for making oceanographic measurements in the nearshore region (Barrick, 1972; Donelan and Pierson Jr, 1987; Trizna, 1997). Compared to visual band observations, X-band radars tend to lack the spatial resolution necessary to

resolve multiple frequency peaks in the wave field which, according to the CSM, is due to long wave modulations limiting the observed signal of shorter waves. Still, multiple studies have successfully demonstrated inversion techniques (Bell, 1999, 2002; McNinch, 2007; Catálan and Haller, 2008).

Radar methods have the attractive attributes that they can be used during day and night time periods, and that radar antennae deployments do not require high elevation platforms. Rotating radars can acquire backscatter measurements over circular regions with diameter in excess of 5 km and with 5 m or better resolution. Because radar systems can be used to sample large surface areas in nearly all-weather conditions, they have become increasingly effective research tools in coastal environments, particularly for examining large-scale coastal behavior.

Yet while many studies have utilized both optical and X-band signals to estimate bottom morphology and bathymetry, there remain complicating factors in using water surface characteristics to estimate bottom morphology. The relation between water depths and wave phase speeds measured by radar and optical techniques can be altered by currents that modify wave numbers. The interactions of currents with surface gravity waves may also increase the surface roughness which has implications for the measured backscatter of an X-band signal (Lyzenga, 1991, 1998; Plant et al., 2010). Haller et al. (2014) have been able to capitalize on this effect by using the increased roughness to image the lateral surface structure of rip currents in the nearshore. For application to estimating the position of bottom features, wave breaking has been shown to be more influenced by bathymetry than by wave-current interactions, even in inlets where currents are particularly strong (Olabarrieta et al., 2014). As such, the change in the location of breaking is expected to be most strongly connected to the change in the location of the underlying bathymetric feature that instigates depth-limited breaking.

Studies of tidal inlets, deltas and other energetic coastal environments have particularly benefited from remote sensing. X-band systems are increasingly deployed in concert with

other remote sensing technologies and in-situ instrumentation to examine the otherwise under-surveyed evolution of coastal features of varying scales (Ruessink et al., 2002; Holman and Haller, 2013; Montreuil et al., 2014; Hessner et al., 2014). The high spatial and temporal resolution of remotely collected data in these environments has allowed forcing mechanisms to be connected directly to morphologic evolution (Balouin et al., 2001; Díaz Méndez et al., 2015; Pianca et al., 2014).

2.2.2 Geographic Setting

Oregon Inlet ($35.779^{\circ}N$, $-75.532^{\circ}W$) is a large inlet system located on the Outer Banks of Dare County, North Carolina. The inlet divides Bodie Island (currently a large spit) to the north from Pea Island (currently connected to Hatteras Island) to the south (Figure 2.1). Following its formation during a storm in 1846, Oregon Inlet rapidly and consistently migrated south at a rate of up to two kilometers per 100 years (Miller et al., 1997). In 1991, the U.S. Army Corps of Engineers Wilmington District (USACE-SAW) built a 1 km terminal groin along the northern end of Pea Island to protect the bridge ramp from further inlet migration (Overton et al., 1993).

The wave climatology at Oregon Inlet consists of periodic high-wave ($> 3m$) events - tropical and extra-tropical storms - that have historically been forced a net southward transport in this coastal area, although this trend can vary seasonally (Inman and Dolan, 1989). While the actual volume of sediment transported along the coast is not well constrained, rough estimates based on wave energy suggest a net southward flux of $282,285m^3$ per year (Dolan and Glassen, 1973). The USACE-SAW conducts a monthly survey of the navigational channel and attempts to maintain a $14ft(4.25m)$ draft clearance by nearly continuous dredging. However, the natural inlet channel has migrated to the south away from the intended navigation route such that it is pinned nearly against the terminal groin (McNinch and Humberston, 2019).

The mean tidal range is approximately 0.98 m on the ocean side of Oregon Inlet (measured

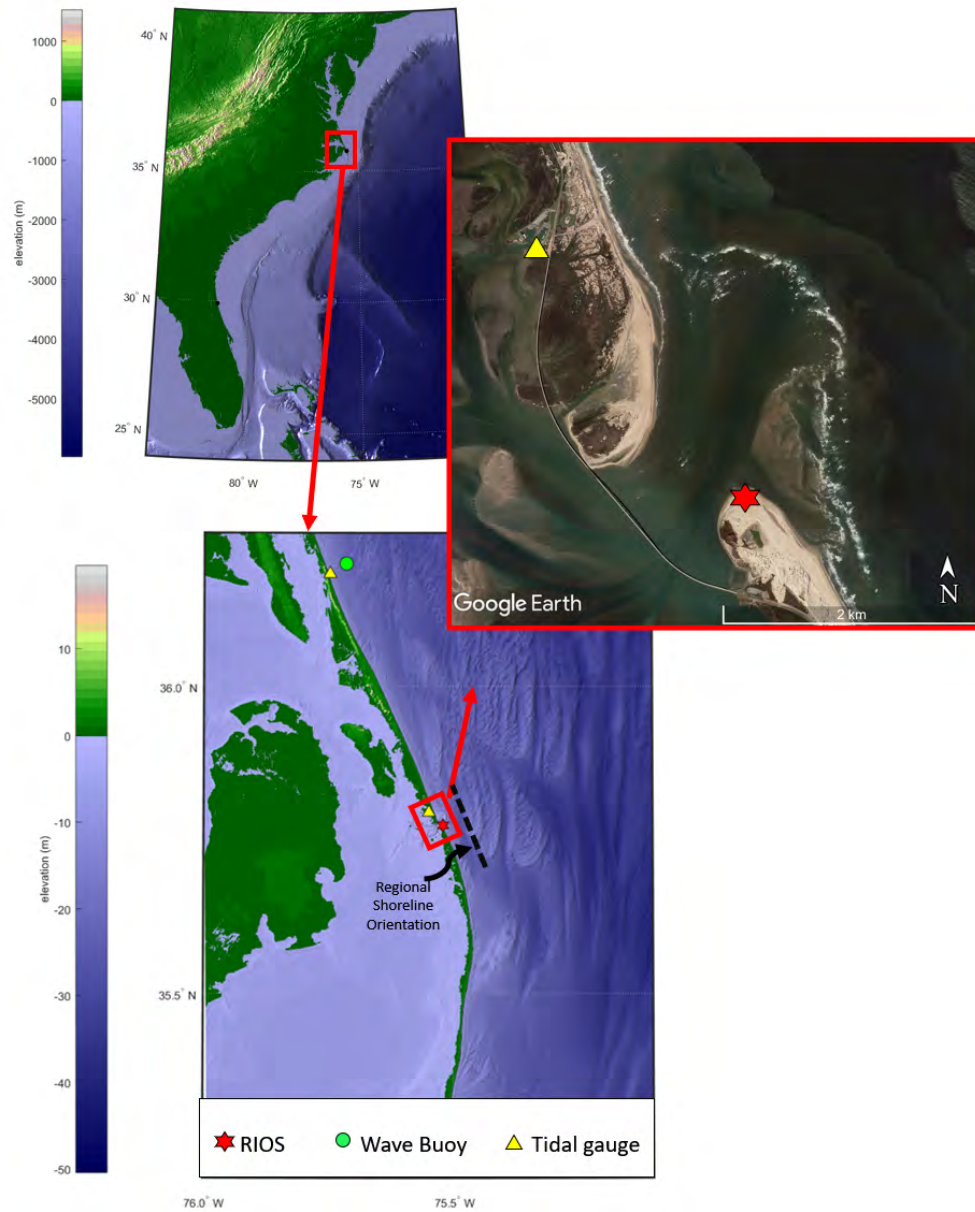


Figure 2.1: (Top-left panel) The Outer Banks are located along the U.S. East Coast. (Top left panel) Oregon Inlet is located along the northern Outer Banks between Bodie Island (to the North) and Pea Island (to the South). The regional shoreline orientation is marked by a dashed black line. (Top right panel) In this Satellite imagery of Oregon Inlet, the bridge spanning the inlet may be seen, as well as wave breaking around the perimeter of the ebb-tidal delta. The position of a RIOS during this study and the Oregon Inlet Marina tidal gauge are marked.

at the USACE Field Research Facility in Duck, NC, about 48 km to the north), and 0.28 m on the bay side (measured at the Oregon Inlet Marina located on the back side of Bodie Island 2.5 km north of the inlet). The inlet connects the Atlantic Ocean to the large Pamlico and Albemarle Sounds to the west of the Outer Banks, and is the only hydraulic connection between the two water bodies for nearly 200 km. The coastline around Oregon Inlet is subjected to a markedly strong and highly variable wave climate for the U.S. East Coast. Consequently, Oregon Inlets ebb delta is considered wave dominated with a small volume relative to its expansive flood delta. Although the installation of the groin has stopped the erosion on Pea Island, the Oregon Inlet channels and delta systems continue to be dynamic. The main channel and surrounding bedforms continually meander and dramatic inlet rearrangements frequently occur during large storm events (Dolan and Glassen, 1973).

2.3 Wave induced longshore sediment transport

Komar and Inman (1970) and Komar (1971) used concepts of wave radiation stress (Longuet-Higgins and Stewart, 1964; Longuet-Higgins, 1970) to derive a simple equation directly estimating volumetric longshore sediment transport from breaking wave parameters

$$Q_s = K_1 H_b^{5/2} 2 \cos(\phi_b - \theta) \sin(\phi_b - \theta) \quad (2.1)$$

where Q_s is the volumetric sediment transport rate (in m^3 per time interval, often reported as m^3/day), H_b is the height (in m) of waves at their breaking point, ϕ_b is the breaking wave crest angle (relative to true N), θ is the shoreline orientation (also relative to true N), and K_1 is an empirical constant relating the driving forces to the sediment flux approximated by $0.4m^{1/2}/s$ for quartz sand (Komar, 1998; Rosati et al., 2002).

Recognizing that H_b is not necessarily uniform along the coast (particularly where there are dynamic coastline shapes present), Ashton and Murray (2006) further modified equation 2.1 to estimate sediment transport from offshore wave properties

$$Q_s = K_2 H_o^{12/5} T^{1/5} \cos^{6/5}(\phi_o - \theta) \sin(\phi_o - \theta) \quad (2.2)$$

where K_2 is a function of K_1 and the ratio of wave height to water depth (assumed to be 0.42 after Komar and Inman 1970, and consistent with Sallenger Jr and Holman 1985) for breaking waves (Komar, 1998), H_o is the wave height in deep water, T is wave period, and ϕ_o is deep water wave angle. The derivation assumes that refraction occurs over shore parallel depth contours, breaking waves are fully shallow water waves, and wave breaking is depth limited. These approximations are assumed reasonable along gently sloping passive margins like the U.S. eastern coastline offshore the Outer Banks and are used herein to estimate sediment transport rates in the vicinity of Oregon Inlet using wave properties measured at an offshore buoy.

2.4 Methods

2.4.1 X-Band Measurements

The US Army Corps of Engineers (Corps) is the lead federal agency tasked with monitoring and maintaining navigable depths in coastal waterways. With limited resources, it has become a significant challenge for the Corps to track the evolution of the many shoals and channels throughout the country that may evolve over single storm events. In an effort to address some of these challenges, the Corps developed the Radar Inlet Observing System (RIOS), an X-band radar system capable of providing tidal-inlet stakeholder a continuous near, real-time assessment of channel and shoal position as well as breaking wave conditions within the navigation channel (Figure 2.2, McNinch and Humberston, 2019).

RIOS is a complete hardware and software system designed specifically to measure morphology over extended deployments in coastal zones (Figure 2.2). As a research oriented system, RIOS is often updated or modified for specific use cases, but always uses a commercial-over-the-shelf (COTS) digital radar (generally from Navico Simrad) to reduce costs and

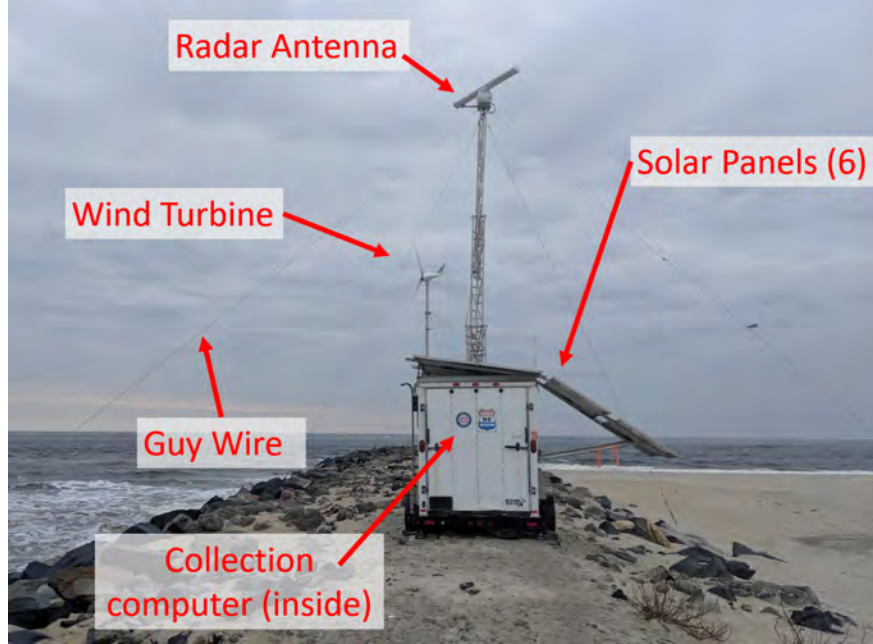


Figure 2.2: A Radar Inlet Observing System (RIOS) at Oregon Inlet, NC in 2019. For this deployment, RIOS was powered completely by the solar panels and the wind turbine. Guy wires stabilized the radar antenna on a telescoping stand to minimize movements from wind.

improve accessibility and reproducibility. A radar antenna does not have the same elevation requirements a camera system might, but a telescoping stand provides the antenna with a clear line of sight to a larger area. The RIOS radar antenna is controlled by a collection computer with custom software that initiates an 10-minute collection every hour, saves the raw data to a hard drive, converts the polar data to Cartesian coordinates, and streams images of the results to an online repository. Between collects, the systems enters a power savings mode where the antenna stops spinning so that the total power requirements for the system are low ($< 1600W/day$). This allows RIOS to be used in remote locations using a built in power systems composed of a battery bank that is charged by a combination of solar panels and a small wind turbine. For extended deployment in remote locations, a backup high-efficient diesel generator can be included and auto-triggered to charge the battery bank if necessary. Deployment typically requires 2-3 person team for one field-day.

Observations of ebb-tidal delta morphology and bedform migration at Oregon Inlet were obtained with RIOS (McNinch et al., 2012; McNinch and Humberston, 2019) deployed on

the terminal groin of the southern side of Oregon Inlet from 21 July 2016 through 16 May 2017. The radar footprint covered a 6 km diameter semi-circle encompassing the inlet and ebb-delta systems. Raw backscatter was collected for 10 minutes each hour at a sampling rate of approximately 1.2 Hz (with very minor variations due to wind). In total, 512 radar antenna rotations were completed during each sampling period and consisted of 514 azimuthal beams, each composed of 1024 evenly spaced range samples over the 3 km radius. The polar coordinate referenced data were gridded to a 5 m Cartesian grid with the x and y axes oriented to the best estimate of the cross-shore (shore-normal) and longshore (shore-parallel) directions, respectively. The regional orientation of the shoreline was estimated to be 152 degrees CW relative to true north based on the regional shoreline orientation of the Outer Banks near Oregon Inlet (Figure 2.1, top right panel).

Gridded intensity values were averaged over each hourly 10-minute collection to produce an hourly time-averaged backscatter product primarily representing wave shoaling and breaking patterns. A 25 hour running average filter was applied to these hourly time-averaged images to smooth the periodic horizontal migration of wave breaking patterns due to dominant M2 tidal constituent (Holman and Stanley, 2007). Resulting 25 hour filtered images produced a more robust representation of wave shoaling patterns and thus a more realistic approximation of the underlying morphology. Finally, a flat structuring element (binary valued neighborhood) was created using a disk method surrounding each pixel of the averaged returns to approximate lingering mechanically spawned background trends which were then removed to accentuate water surface related features (Figure 2.3; Van Den Boomgaard and Van Balen, 1992).

While wave breaking locations are expected to be primarily dictated by the underlying morphology, other processes such as wave-current interactions may also shift the breaking location (Olabarrieta et al., 2014). Therefore, without further verification, areas with high levels of continuous backscatter associated with wave breaking are considered implied bed-form locations (henceforth shortened to IBL) as there is yet some ambiguity in the exact

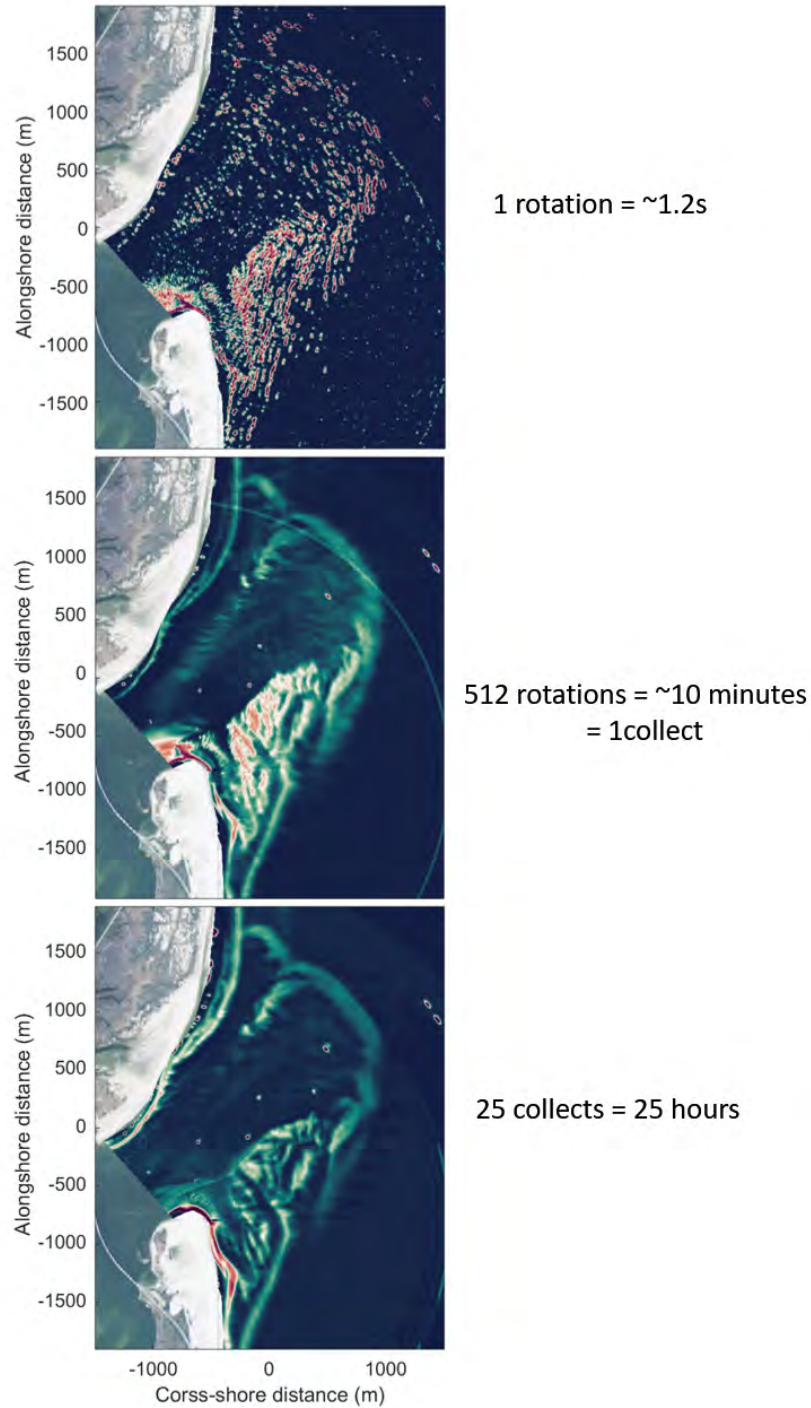


Figure 2.3: (Top panel) An example of the relative x-band backscatter from a single antenna rotation (which takes place over approximately 1.2s) at Oregon Inlet. The intensity of the return signal represents the near instantaneous wave shoaling and breaking patterns. (Middle panel) The average backscatter intensity from a 10-minute (512 rotation) collection. (Bottom panel) An example 25 hour filtered product of the 10-minute average intensities used to smooth the lateral shifts in wave breaking due to tides.

relation between the backscatter maximum and morphological features.

2.4.2 Morphodynamic analysis

The areas over land and within the sound were voided in the temporally smoothed 25-hour intensity images. The remaining field of view was then analyzed from Eulerian and Lagrangian perspectives to estimate the migratory rates and directions of IBL. In the first (Eulerian) method an optical flow tracking algorithm was applied to the daily averaged images to estimate the flow (following Farnebäck, 2003). Various forward stepping intervals ranging 2 to 25 hr were used in the optical flow algorithm, with a 4 hr interval chosen to allow appreciable morphologic evolution without overly smoothing fine scale changes. The migration patterns of the IBL resulting from this analysis were decomposed into their cross-shore and longshore components relative to the estimated regional shoreline orientation.

The second method followed specific bedforms using a Lagrangian approach in the form of longshore and cross-shore oriented Hovmoller diagrams, also known as timestacks (Shand et al., 1999). Timestacks with spatial extent of 1200 m were created along the x and y axes over a staggered grid designed to minimize overlap (Figure 2.4). Coherent increased intensity returns due to consistent wave shoaling and breaking signified the presence of a bedform. These features could be tracked through space (in orthogonal directions) and time. In each timestack that contained at least one clear bedform migratory path, the most complete path within the timestacks spatial extent was coarsely manually marked (Figure 2.5-magenta). In each case, the cross-shore and alongshore movements were chosen independently and so do not necessarily reflect the same bedform but only an orthogonal component within the same area. The periodically chosen positions were interpolated onto each timestep to create a continuous digitized bedform path (Figure 2.5-black). A local maxima filter was applied to the continuous manually selected paths to capture the finer scaled variations of bedform movements (Figure 2.5-green). In cases where no bedform path could be clearly identified or distinguished from other bedform paths, none were extracted.

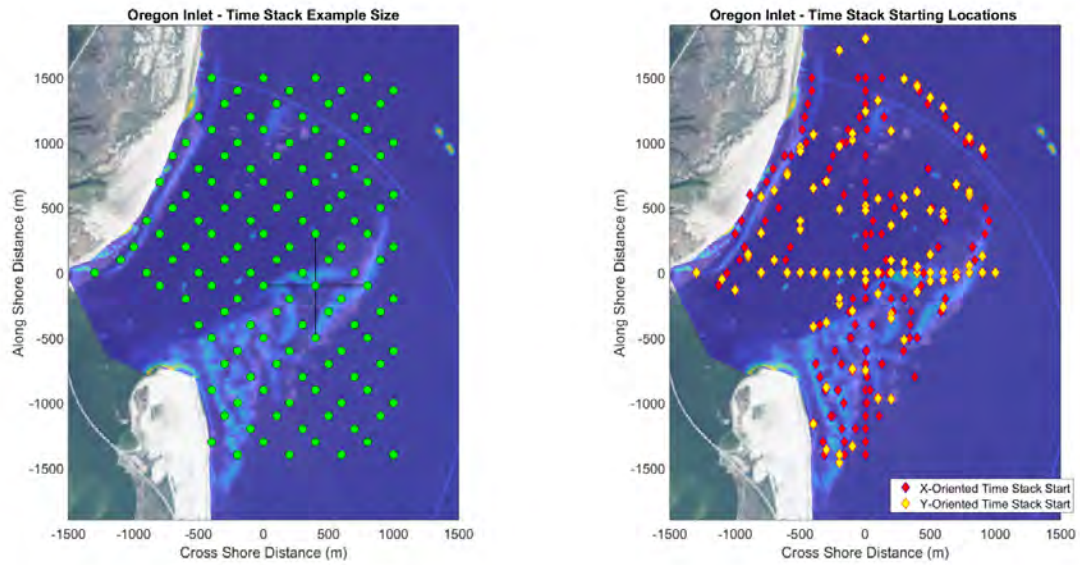


Figure 2.4: (Left panel) Predetermined locations where timestacks were created. The black lines show an example of the cross-shore and longshore orientation and reach of the timestacks. Timestacks overlap 50% with the next timestack in each direction so that bedform paths extending off the edge of one may be marked in their entirety in the adjacent timestack. (Right panel) Starting locations of bedforms migratory paths picked within timestacks. X (cross-shore) and Y (alongshore) oriented timestacks were differentiated as they did not necessarily depict the same bedform.

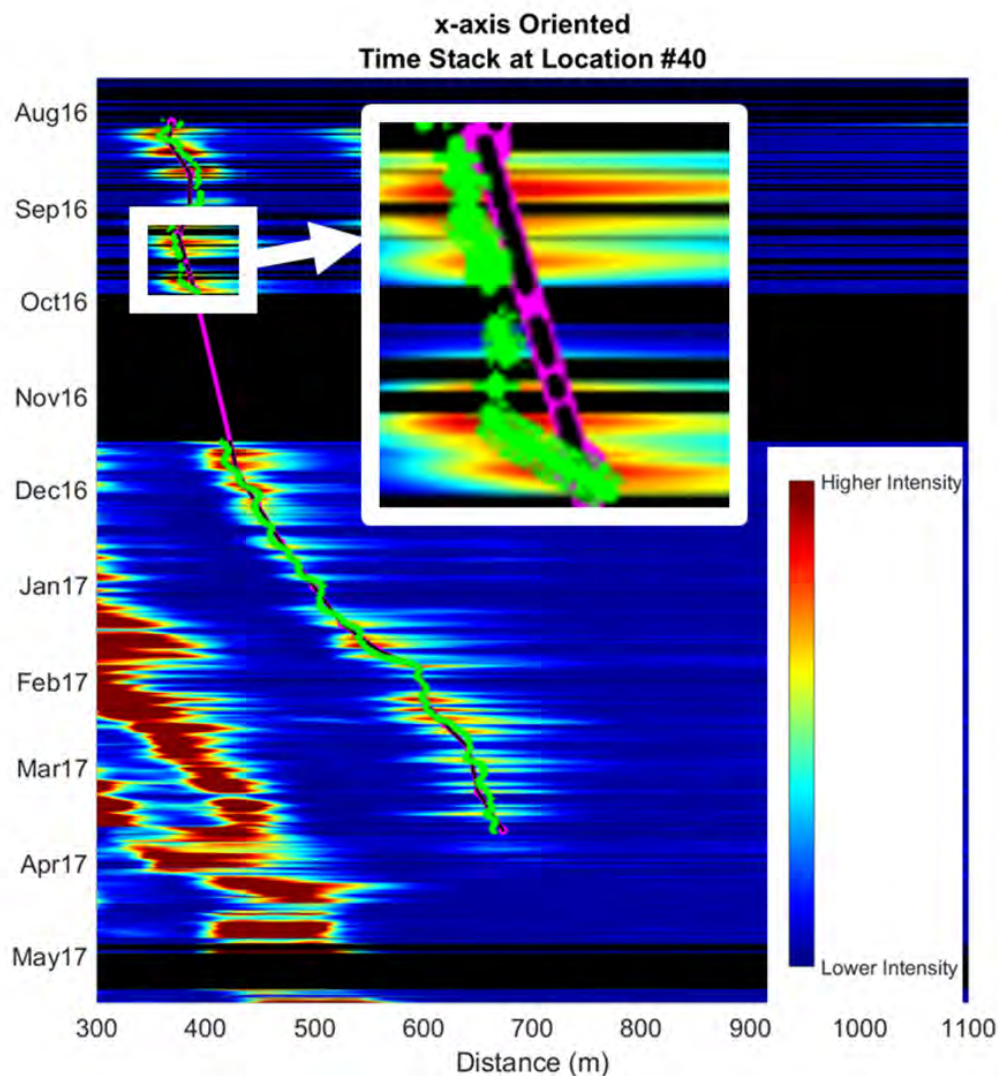


Figure 2.5: An example of a cross-shore oriented timestack. The colormap represents the averaged backscatter intensity in which peaks represent the location of a bedform. The zoomed in subset shows an example area of the manually picked bedform path through time (magenta), the path interpolated only during period the radar was active (black) and the path picked by applying a local maxima filter (green).

2.4.3 Longshore Sediment Transport

Time series of wave statistics were obtained from a Datawell Directional Waverider buoy (NDBC station #44100) located in 26 m water depth seaward of the coast of the USACE FRF in Duck, 48km north of Oregon Inlet. Wave statistics from the buoy include significant wave height (in m), peak and mean wave period (in sec) and peak and mean wave direction (in degrees from true N). The Oregon Inlet Buoy (NDBC station #44095) located nearly directly offshore from Oregon Inlet was offline for substantial portions of the study period; however, time periods when data were available from both buoys were compared to determine mean differences in wave statistics and an assessment of the usefulness in using the more distant Duck wave buoy data. The average difference between the FRF and Oregon Inlet wave direction measurements was 5.8° . This was added to the wave angle recorded at the FRF buoy to account for the bulk lateral variation in wave angles from the buoy location to offshore of Oregon Inlet. An analysis of the effects of the spatial separation between the buoy used to make wave measurements and the inlets location was conducted and results are discussed in Appendix A, but results suggest any effects were limited.

The wave records were used to estimate longshore volumetric sediment transport in the nearshore region using equation 2.2 with the deep-water wave height approximated by the observed significant wave height, the deep-water wave period assumed to be the average wave period and the deep water wave angle assumed to be the average wave angle.

2.5 Results

2.5.1 Bedform Migratory Patterns

Migration rates and directions estimated from the Eulerian optical flow tracking algorithm were averaged from 16 November 2016 to 01 April 2017, a period with no data lapses, to examine long-term migration patterns (Figure 2.6). The analysis revealed complex but spatially coherent migration patterns which suggests the various IBL are migrating in recurring

patterns over time.

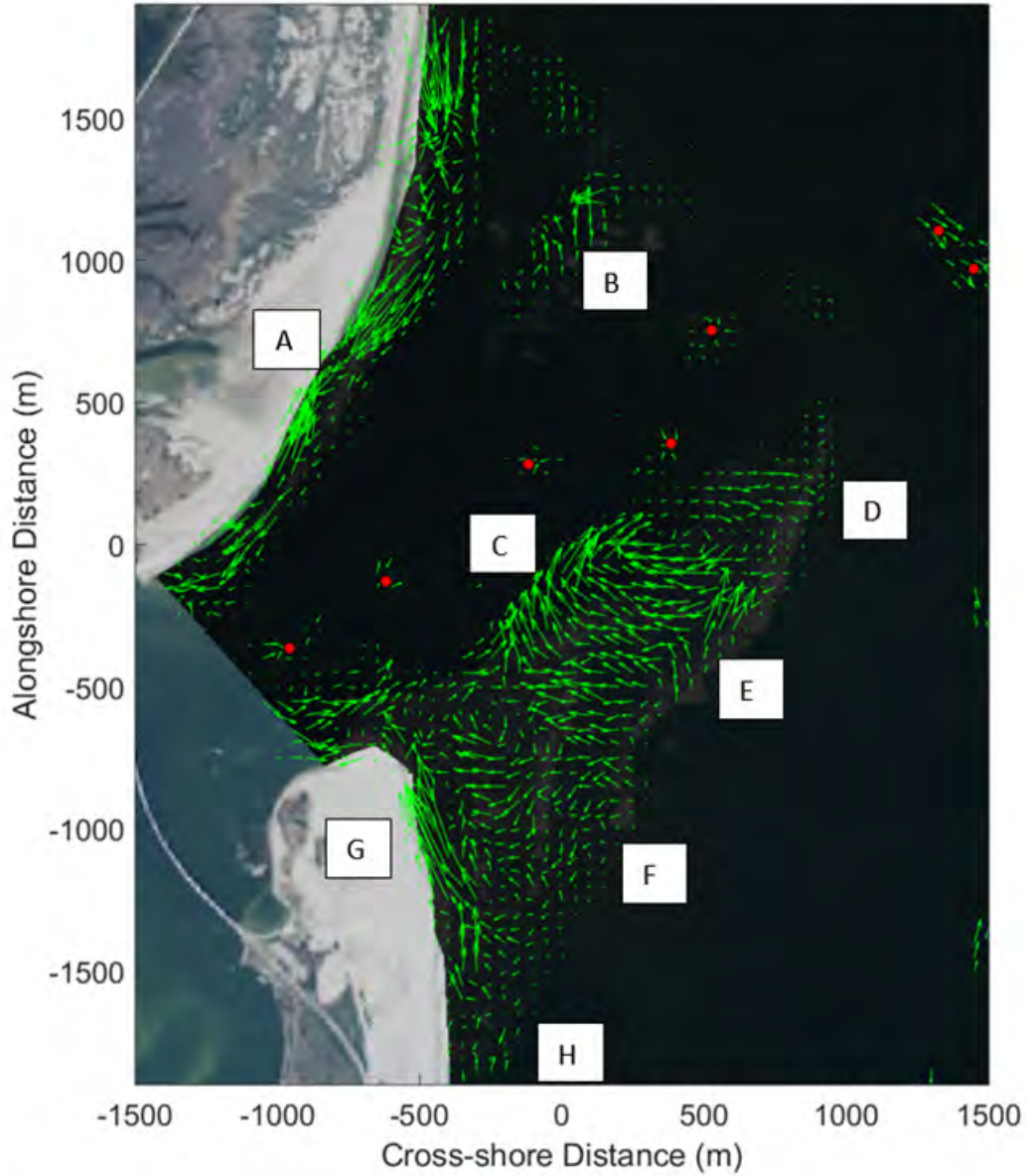


Figure 2.6: Temporally averaged direction and relative magnitude of bedform movements (green arrows) for a period from 16 November 2016 to 01 April 2017. Migration patterns and rates were obtained using an optical motion tracking algorithm on successive 25-hour averaged intensity images. The red dots mark the location of the channel marker buoys which introduce artificial migration indicators in their immediate vicinity. Letters mark areas of interest (see text for explanation).

There is a migration of the IBL towards the inlet within the northern marginal flood channel (along the coast of Bodie Island). This is consistent with the dominant direction of

alongshore sediment transport due to wave activity as well as the tidally controlled direction of flow expected in this channel. Sand bar like features were observed along this section of coast and became increasingly perpendicular to the coast and the inlets throat towards the terminus of Bodie Island. The inlet directed migration of bedforms along the northern coast is interrupted by an area of reverse bedform migration (Figure 2.6, location A). This area coincides with the mouth of a minor second channel that periodically opens, generally during storm events.

A long ($> 1000m$), narrow ($\sim 250m$) and relatively linear shoal feature (channel margin linear bar) existed seaward of Bodie Islands coast and separated the marginal flood channel from the main ebb channel (Figure 2.6-B). This feature was observed through much of the study period and averaged radar images suggest it was superimposed with sand waves with roughly 60 m wavelengths. However, due to significant wave dissipation over the terminal lobe, wave shoaling and breaking patterns were only consistently recorded on the seaward end of this linear shoal feature and so the motions of IBL along the landward segment of the bar are not well captured in the averaged flow analysis results. The IBL movements over this inner part are periodically captured and during such times were consistently migrating seaward. The migratory patterns on the seaward edge of this shoal, which were captured by the optical flow analysis, show a recirculation pattern where bedforms migrating seaward curve northward and then landward, presumably as the channel focused ebb current dissipates into the surrounding waters (Figure 2.6-B).

To the south of the main ebb channel is a large shoal complex. It is markedly larger than the solitary channel margin linear bar to the north of the channel. The optical flow analysis shows that the movement of the breaking patterns on the southern shoal complex are also more dynamic than those on the northern shoal. Along the southern edge of the main ebb channel, IBL were continuously migrating seaward (Figure 2.6-C). Like on the northern shoal, but mirrored, IBL migrating seaward begin to curve away from the main ebb channel near the terminal lobe, again likely due to a dispersing ebb-current (Figure

2.6-D). The large portion of the center of the southern shoal complex (Figure 2.6-E) shows evidence of IBL migrating back toward the main ebb channel. In combination with the seaward portion of the complex, this forms a circular and rotating migration pattern of the IBL. Further landward on the shoal complex (Figure 2.6-F) the IBL migration directions begin to orient towards the shoreline. Along the coast of the southern island (Pea Island; (Figure 2.6-G) there is a strong migratory pattern towards the inlet within the southern marginal flood channel. Further south, there is a relatively subtle migration pattern that suggests bedforms are welding to the coast of Pea island approximately 1100m south of the inlets southern extent (Figure 2.6-H).

2.5.2 Alongshore forces acting on an ebb-tidal delta

The modeled longshore transport time series were compared with the spatially averaged alongshore migration rates of IBL estimated by the Eulerian motion tracking algorithm (Figure 2.7), and found to be significantly correlated (Figure 2.8; $R = 0.65$ with 95% confidence interval of 0.08 given by the long-lag artificial skill method of Davis, 1976). This provides statistically significant evidence (explaining 45% of the variance) that the average estimated alongshore sediment transport varies concurrently with the movement of IBL on the ebb-tidal delta. The remainder of the variance not explained by the alongshore model is due to limitations to the gross sediment transport model, inaccuracies in observed IBL rates, and sediment transport unrelated to shoal migration. Additionally, the alongshore bedform movements and sediment transport may be complicated by cross-shore circulation within the inlet itself, not unreasonable considering the more complex recirculating sediment transport pathways at Oregon Inlet hypothesized by (McNinch and Humberston, 2019).

Individual bedform migration captured by the Lagrangian analysis of the full study period showed high variability. The average migration distance of all bedforms tracked through the analysis was 40.5 m to the south indicating a net southward transport (Figure 2.9) under the assumption that transport is in the direction of shoal migration (e.g., Robinson, 1975;

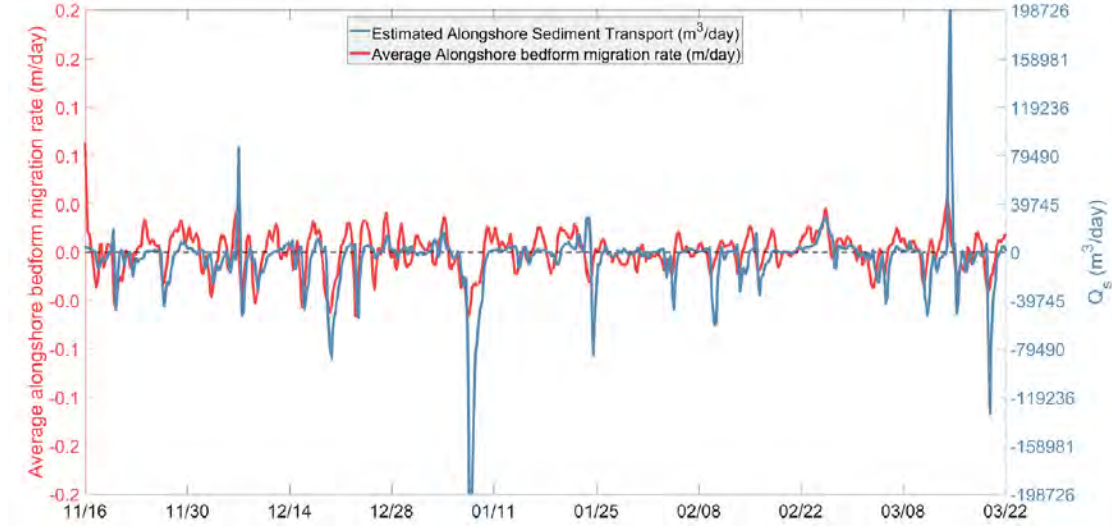


Figure 2.7: Spatially averaged alongshore bedform migration rate (red; left axis), and estimated wave driven alongshore sediment transport from the Ashton and Murray (2006) derivation (blue; right axis).

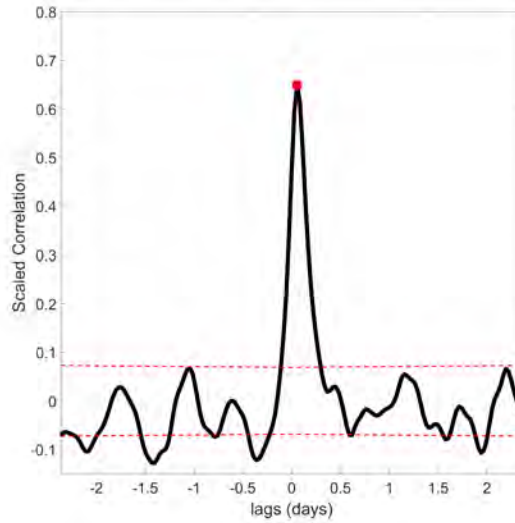


Figure 2.8: Time lagged cross-correlation between the spatially averaged alongshore bedform migration time series and the estimated wave driven alongshore sediment transport. Maximum correlation is 0.65. 95% confidence intervals are shown with the dashed gray lines (computed using the long-lag artificial skill method of Davis (1976)).

O'Connor et al., 2011; Pianca et al., 2014; Ridderinkhof et al., 2016). Because the timestack measurements capture the cumulative migration of bedforms, their average deviation from their starting position was compared against the cumulative estimated sediment transport rather than the instantaneous rates (Figure 2.10). While many of the high frequency variations experienced on average by the system are not captured by the time-stack analysis, the bulk north to south migration rates and longer scale patterns show similar trends.

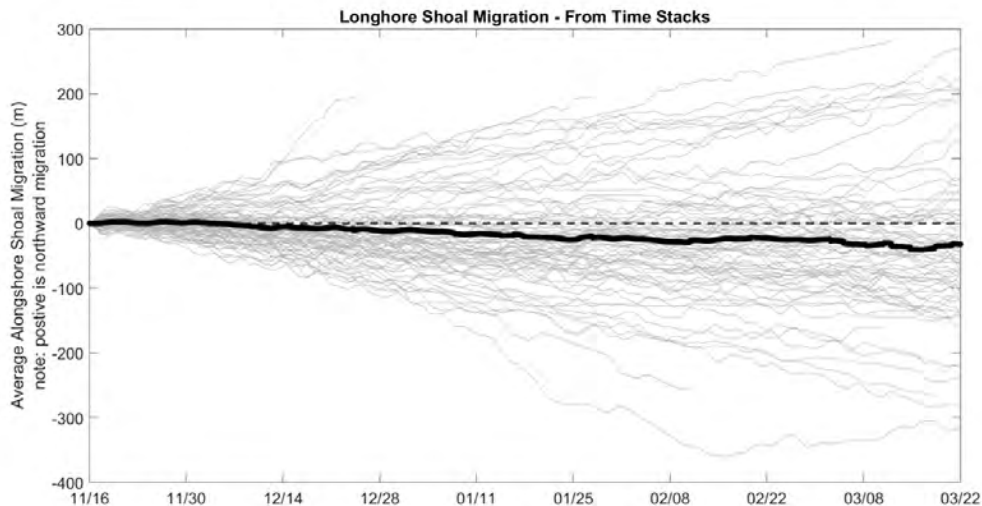


Figure 2.9: Alongshore bedform migration distances of all the bedforms depicted in the timestacks (gray lines), and the average alongshore location of all bedforms over time (bold black line).

2.6 Discussion

2.6.1 Wave Forcing

A significant correlation was found between the alongshore bedform movement and estimates of alongshore sediment transport based on offshore wave properties (Figure 2.8). This result was based on averaging the longshore IBL migration rates over the ebb-tidal delta, greatly simplifying the complex sediment transport processes of ebb-delta shoals. The average trends depicted are certainly the culmination of more complex and localized processes. Olabarrieta et al. (2014) showed that currents over the ebb-delta are complex, consistent with the spa-

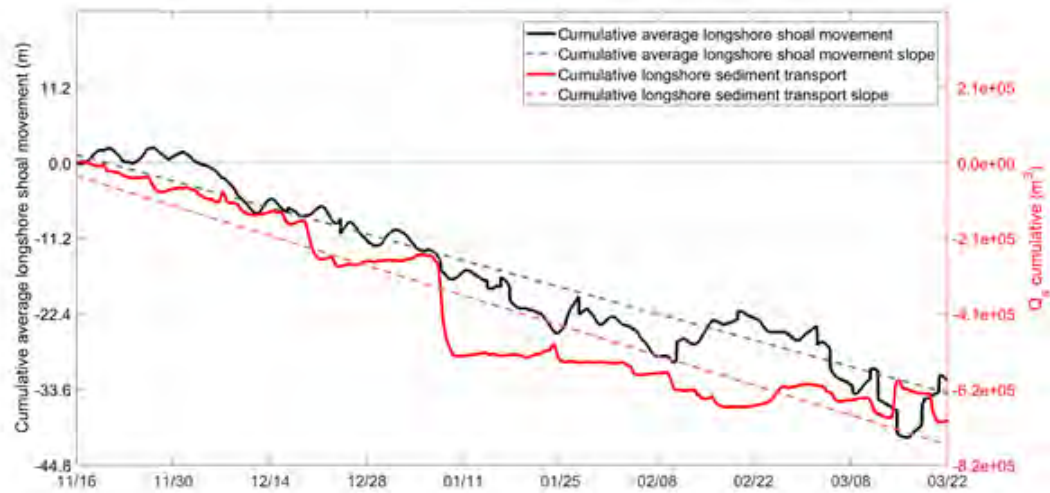


Figure 2.10: Time series of the cumulative average longshore bedform movement magnitude (solid black line; left axis) and its linear trend (dashed black line), and the cumulative estimated alongshore sediment transport (solid red line; right axis) and its linear trend (dashed red line).

tially resolved RIOS observations of bedform migration. Additionally, ebb tidal currents are not exclusively oriented seaward but fan out over the ebb-tidal delta. Oregon Inlets main channel is also tilted relative to the shore-normal axis used to define the alongshore and cross-shore directions of bedform migration. Despite these complicating factors, the strong correlation between bedform movement and wave driven transport suggests that alongshore oriented wave forces strongly influences sediment transport and bedform movement on the ebb-tidal delta.

The relation between wave driven longshore transport and bedform movements at Oregon Inlet is not unexpected. Classic theory suggests swash bars (bedforms) bypass an inlet by following a continuous path along the terminal lobe of a wave dominated ebb-tidal delta due to wave action and ebb-tidal currents (FitzGerald, 1982). However, the results of the Eulerian tracking analysis of IBL suggest that there is a more complex sediment bypassing pathway controlled by a combination of wave-driven alongshore forces (as quantified by Ashton and Murray, 2006) and cross-shore forces which may consist of sub-tidal pressure gradients across the inlet, tides and wave-driven flows, as suggested in McNinch and Humberston (2019).

2.6.2 Longshore transport

Wave driven longshore transport rates were calculated using observed wave observations continuously obtained for 1 year between 20 Oct 2016 and 20 Oct 2017 from Ashton and Murrays equation 2.2 (Figure 2.11). The average transport rate was $242 \text{ m}^3/\text{day}$ with a net year-long longshore transport of $90,000 \text{ m}^3$ directed southward. This estimate is roughly consistent (within an order of magnitude) of the annual $282,285 \text{ m}^3/\text{yr}$ southward transport calculated by Dolan and Glassen (1973). However, there are marked season variations in wave conditions at Oregon Inlet. A 164 day time period from 20 Oct 2016 to 31 Mar 2017 spanning the fall and winter months (when RIOS observations were present and strongly correlated to Ashton and Murrays formulation) was dominated by waves from the north, resulting in net alongshore transport of $904,000 \text{ m}^3$ directed southward ($5,512 \text{ m}^3/\text{day}$). During the ensuing 203 days from 1 Apr 2017 to 20 Oct 2017 (when RIOS observations were not present), the net transport was $814,000 \text{ m}^3$ directed northward ($4,099 \text{ m}^3/\text{day}$), nearly balancing the yearly net alongshore transport.

The seasonal transport rates, largely determined by the occurrence of storm events, are up to an order of magnitude larger than the yearly average. Long term averages homogenize the intermittent but dominating effects of storms, most commonly occurring from wave events out of the north (noreasters) in the late fall and winter and out of the south (tropical cyclones) during late summer and early fall (Figure 2.11). Changes in the number or intensity of storms during a season may thus substantially modify the net transport over annual time scales. The relatively small net volume of longshore transport estimated over the whole year ($90,000 \text{ m}^3$) might have been coincidentally directed southward simply owing to the timing and occurrence of the storms during the analyzed time period.

The estimate of a net southward wave-driven alongshore sediment transport along this section of coast is consistent with previous studies (Dolan and Glassen, 1973; Birkemeier et al., 1985; Inman and Dolan, 1989) and further supported by the long term southern progression of Oregon Inlet until the installation of the terminal groin. The significant

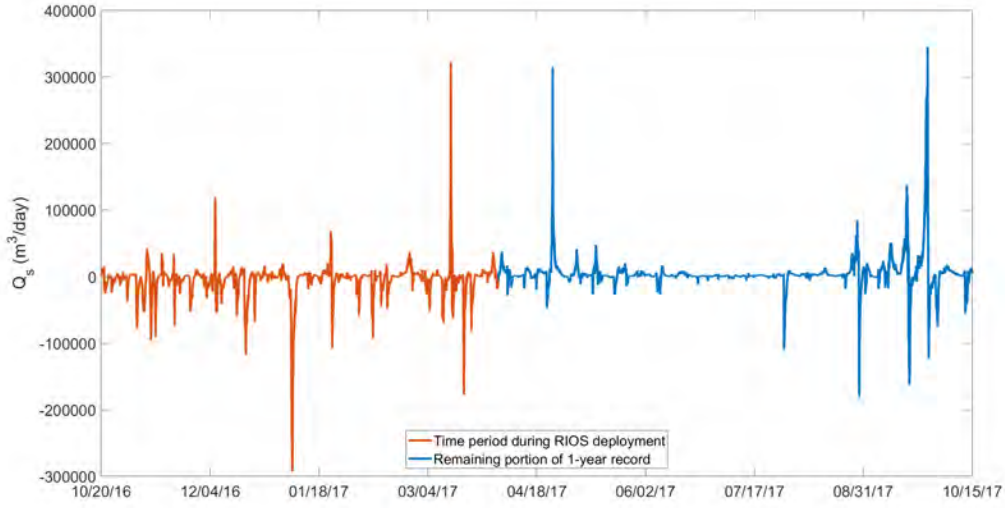


Figure 2.11: Estimated wave driven alongshore sediment transport rate from the Ashton and Murray (2006) formulation (Equation 2.2) during a year long period from 20 October 2016 to 20 October 2017. The orange line shows the period during which RIOS was deployed and the blue shows the remaining portion of that year. Transport directions are predominantly N-to-S during the late fall, winter and early spring months and S-to-N during the later summer and early fall months.

correlation between the alongshore sediment transport estimate and the spatially averaged migration rate of IBLs suggests that the noted wave properties driving alongshore sediment transport on open beaches are similarly influencing coherent bedform movements on Oregon Inlets ebb delta.

Storm events can dominate both the sediment transport and bedform migration signals and at times drove estimated transport rates exceeding $200,000 m^3/day$. It remains unclear whether such rates are realistic as there is no effective method to measure the representative large scale sediment transport along a section of coast. Nevertheless, it is worth considering that the simple Ashton and Murray (2006) alongshore sediment transport model captures relative trends in transport both up and down coast driven by changes in wave direction and magnitude (largely dictated by the wave height term $H_o^{12/5}$), but lacks the complexity to accurately quantify details of the sediment flux. Sophisticated numerical models are required to resolve the nature of the three-dimensional sediment transport, yet the details of sediment

transport formulations used in such models are also highly dependent on parameterizations not easily validated on large time and space scales similar to those in this study. Field verification efforts are thus generally limited to comparison with observed hydrodynamics and measured (in situ) changes in bathymetry, and are the subject of ongoing research efforts.

A potential limitation to the method of remotely determining bedform location (and the subsequent implied direction of sediment transport) with RIOS is the effect of currents on wave properties. Although not expected to influence wave breaking patterns as strongly as bathymetric changes, wave-current interactions can also alter breaking locations. Currents can increase surface roughness and interact with wave orbital velocities such that patterns of waves shoaling and breaking are modified independently of morphologic change, but such shifts are expected to be minor in the alongshore direction (Haller et al., 2014). Thus, for this study, it is assumed that depth-limited wave breaking is the primary control on breaking locations (Olabarrieta et al., 2014).

2.7 Conclusions

Multi-month X-band radar measurements of breaking and non-breaking surface waves obtained with RIOS (McNinch and Humberston, 2019) at Oregon Inlet, NC, provides an implied measure of the morphologic evolution of bedform features superimposed on the ebb-tidal delta. Using the simple alongshore sediment transport model of Ashton and Murray (2006), a time series of alongshore transport was estimated from wave parameters measured at an offshore buoy. The alongshore transport time series was compared to a spatially averaged time series of alongshore movements of implied bedform locations measured by RIOS (under the assumption that sediment transport is in the direction of shoal migration). The two records were significantly correlated ($R = 0.65$) suggesting that offshore wave properties are strongly influencing the alongshore migration of bedforms on the ebb-tidal delta, accounting for about 45% of the variance.

The Ashton and Murray transport formula was applied to continuous offshore wave data

for a year-long period from 20 Oct 2016 to 20 Oct 2017 and estimated that a net volume of $90,000m^3$ was transported from north to south across the inlet. This estimate is smaller but of similar magnitude and the same direction as the $282,285m^3/year$ estimated by Dolan and Glassen (1973). During the 164 day period when RIOS was deployed (20 Oct 2016 to 31 Mar 2017), the net alongshore transport was $904,000m^3$ directed southward, and during the following 201 days between 1 Apr 2017 and 20 Oct 2017 the transport was $814,000m^3$ directed northward, nearly balancing the yearly transport. These pronounced seasonal signals in longshore transport arising from the number and intensity of random storm events can result in high inter-annual variability that, given the correlation between transport rates and bedform movements on the ebb-tidal delta, are expected to strongly influence ebb-delta morphologic evolution at wave dominated inlets.

2.8 Acknowledgments

This work was supported by the U.S. Army Corps of Engineers and the expert field and technical crew of the Field Research Facility in Duck, NC. J.H. was supported under the Department of Defenses Science, Mathematics and Research for Transformation (SMART) Scholarship program. Comments from the anonymous reviewers greatly improved the paper.

CHAPTER 3

Regional winds substantially influence tidal inlet currents at Oregon Inlet, NC

3.1 Abstract

The influence of local and regional winds on tidal inlet hydrodynamics is examined using observations of currents, water level and winds collected over 40 days in Spring 2019 at Oregon Inlet, NC. Oregon Inlet is a large (1km wide, 9m deep) meso-tidal inlet with complex delta systems and a primary channel that, constrained by a terminal groin, meanders and periodically resets. Data show that a component of the current velocity through the primary channel fluctuates over subtidal time scales unrelated to astronomical tides. This subtidal current component is substantial, exceeding the magnitude of the tidal current one third of the time. The time series of water level slope through the inlet, estimated from pressure sensors located on both sides, is highly correlated with the subtidal current ($R = 0.95$). Wind magnitudes during this time ranged from 0 to 18m/s and the record of wind velocity through the inlet contained a sub-tidal component, also well correlated ($R = 0.86$) with the subtidal water level slope. A simple basin wind surge model and evidence from other studies suggest that the subtidal water level oscillations on the sound side of the inlet are driven by regionally induced wind surge. A force balance at the inlet indicates that the subtidal water level slope through the inlet is the dominant driver of the subtidal along-channel currents, with weaker contributions from local wind drag and possibly waves. The combination of observations and theoretical analysis indicate that regional winds induce a through inlet water level slope that exerts a first-order control on the currents at Oregon inlet. The temporal superposition

of the decoupled tidal and subtidal forces produces irregular hydrodynamic patterns within the inlet that are not well described by the traditional inlet classification system based only on the relative effects of tides and waves. The first-order influence of winds at Oregon Inlet may result from the geographic setup, but these processes are also likely to be influential at other meso-tidal inlets with large, shallow inland water bodies.

3.2 Introduction

A tidal inlet is a constrained channel or system of channels maintained by tidal flows that connect the open ocean to an estuary or other inland tidal water body. They exist around the world in a range of coastal environments, but are especially common along barrier island systems and other sandy shorelines where they may originate due to storm driven overtopping and scouring processes (FitzGerald and Pendleton, 2002). Breaches that evolve into stable inlets often control the regional coastal environment beyond their immediate geographic footprint (Hayes, 1980; FitzGerald, 1988). For example, tidal inlets positioned at the seaward edge of an estuary or bay system will regulate the flux of water, sediment, and nutrients into and out of the system, and are therefore an important control on the systems overall ecologic health (Fulton et al., 1993). Tidal inlets are equally influential from a geophysical perspective as flooding and ebbing cross-shore tidal currents disrupt alongshore sediment transport, temporarily or permanently storing large volumes of sediment in flood and ebb tidal deltas (FitzGerald, 1982; Boothroyd, 1985; Walton and Dean, 2011; Legault et al., 2012). These disruptions may manifest as large scale erosional or accretional patterns over extended swaths of neighboring coastline (FitzGerald, 1988).

Traditional characterization of tidal inlets focuses on the interplay between the hydrodynamics and morphology that result from a balance between tidal forces, typically characterized by the regional tidal range, and wave forces, generally captured by some measure of the regional wave climate (Hayes, 1975, 1980). This foundational categorization of inlets is still well accepted today, even as more recent observations and proliferation of numerical models

have allowed a closer examination of wave-current interactions, the role of sediment type and size, and anthropogenic impacts (Velasquez-Montoya et al., 2020; Lenstra et al., 2019; Olabarrieta et al., 2014; Giese et al., 2020). Despite these advances, accurate prediction of tidal inlet hydro- and morpho-dynamics, including the active evolution of tidal deltas, has remained challenging, at least partly owing to the complexity of inlet geometries, external forces, and internal hydrodynamic processes. Some models have shown success in making accurate morpho-dynamic predictions, though typically under hindcasts with parameters tuned by observations (Velasquez-Montoya et al., 2020; Hopkins et al., 2018).

Other verified hindcast models have been used to examine the physics of inlet hydro-dynamics and how they respond to wave forcing. Orescanin et al. (2014) showed that the currents through Katama Inlet on Marthas Vinyard, MA, during two hurricane events, were better modeled when ocean wave forcing was included. However, the study also found that, several kilometers further inside the bay at Edgartown Channel, the influence of wave forcing on currents through the channel was small compared with pressure gradients between Katama Bay and Vinyard Sound. Another study (Wargula et al., 2014) examined the forcing of currents across the ebb shoals at New River Inlet, NC (a situation like Katama Inlet), and found that waves over the ebb tidal delta significantly contributed to the subtidal along-channel momentum balance at that location. About 1-2 kilometers inside of the breaking waves though, the primary force balance was again between the pressure gradient and the bottom drag, with wave influences only of consequence during storms. Wargula et al. (2018) also showed the important influence of waves on water level modulations over the ebb-tidal delta, noting that they may contribute to the asymmetry of tidal currents. In each of these studies, the influence of waves and inertia on the main inlet channel currents well inland of the ebb shoals and wave breaking was small compared with pressure gradients and bottom drag. The direct forcing of currents by wind drag or wind-induced setup was not discussed in detail in these studies.

It is well known that winds can produce strong coastal currents (e.g., Winant and Beard-

sley, 1979) as well as significantly raise (or lower) water levels on the order of meters both on the ocean and sound sides of an inlet (e.g., Thompson et al., 2014; Mulligan et al., 2015; Safak et al., 2016). Recent studies at Ameland Inlet located between the North Sea and the Dutch Wadden Sea (a large shallow inland water body) more closely examined how winds may influence inlet processes (Elias et al., 2019; Van Weerdenburg, 2019). Residual non-tidal flows are observed within the inlet that significantly altered the tidal currents, at times entirely reversing them. Their analysis suggests the inlet currents result from a combination of waves and wind induced currents, and that winds significantly contribute to inlet flow and basin connectivity.

In this study, we examine the relative importance and mechanisms of wind influence on along-channel currents within Oregon Inlet, a dynamic spatially-large meso-tidal inlet located on the Outer Banks of North Carolina, a barrier island system within the mid-Atlantic Bight of the eastern seaboard of the U.S. (Figure 3.1). The Outer Banks is a chain of spits and islands spanning several hundred kilometers and reaching nearly 50 km seaward of the mainland. The system encloses the Albemarle and Pamlico Sounds, that together form a very large, shallow inland waterbody (Figure 3.1). The dominant exchange of water between the sounds and the Atlantic Ocean occurs about 50 km north of Cape Hatteras through Oregon Inlet where the hydrodynamics are characterized by strong flood and ebb currents within the inlet, wave breaking over the ebb-tidal shoals, and dynamic sediment transport that periodically rearranges the shoals and inlet channel, creating severe navigational hazards for fishing and recreational boats (e.g., Humberston et al., 2019).

There have been several studies that suggest winds may alter currents at Oregon Inlet (Nichols and Pietrafesa, 1997; Jarrett, 1978; Safak et al., 2016; Clunies et al., 2017). Like at Ameland Inlet, the landward side of Oregon Inlet is characterized by a large and shallow water body. However, unlike in the study of wind influence at Ameland Inlet, most studies of Oregon Inlet would suggest winds influences inlet currents by altering water levels, as opposed to wind shear stress directly modifying the currents. Oregon Inlets geographic configuration

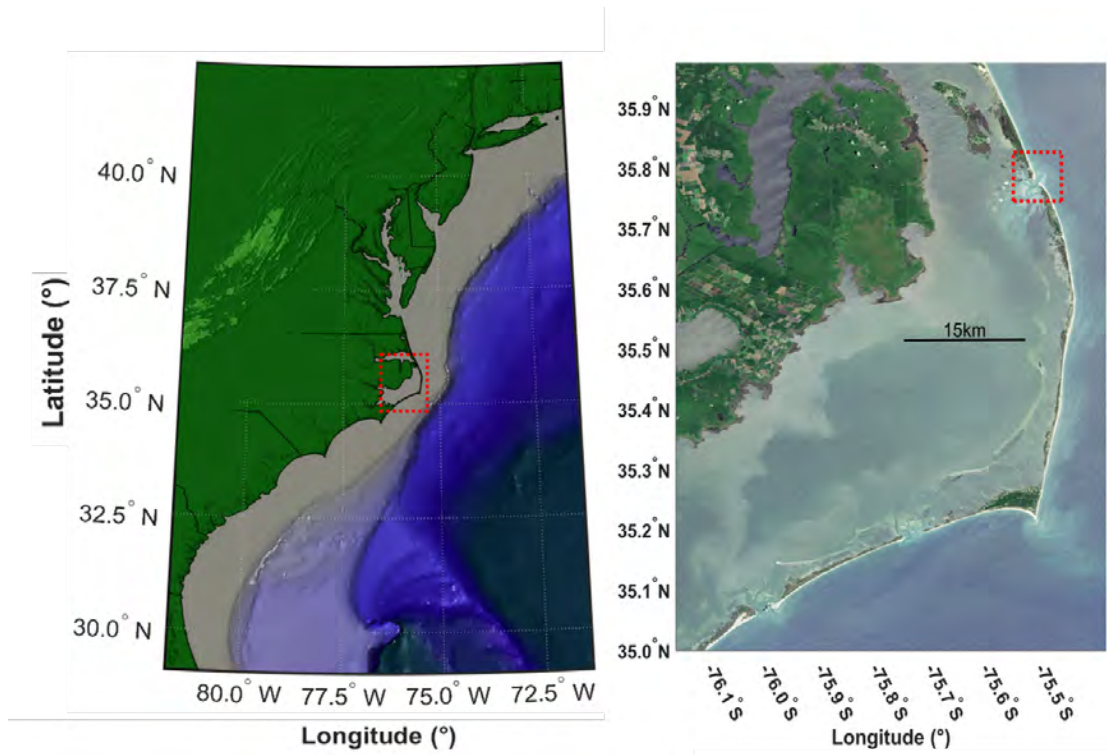


Figure 3.1: (left) The study site is located at Oregon Inlet along the Outer Banks, NC, a large spit and barrier island system on the U.S. mid-Atlantic coast highlighted by the dashed red box. (right) The inlet, in the dashed red box, is the northernmost of 3 inlets that connect the Atlantic Ocean to the large Pamlico sound.

(Figure 3.1), combined with prevailing winds from the southwest and northeast, maximizes fetch length over the Pamlico Sound and enhances wind induced setup(down) (Safak et al., 2016; Mulligan et al., 2015). Previous observations and numerical simulations have shown that winds may alter water levels in the sound by more than 2 m, a magnitude that surpasses the tidal range within the sound by at least an order of magnitude (Mulligan et al., 2015; Safak et al., 2016; Clunies et al., 2017; Rey and Mulligan, 2021).

Still, the influence of these wind driven water level fluctuations on inlet hydrodynamics have not been quantified. In an early study of Oregon Inlet, Jarrett (1978) speculated that anomalies observed in the flow through the inlet were due to wind forcing. Later, an internal report on larval fish transport by Nichols and Pietrafesa (1997) found qualitative relationships between synoptic scale atmospheric wind events and inlet flow. In a study of barrier island breach events, Safak et al. (2016) noted this same relationship between winds and water level variations along the North Carolina coastline of the Outer Banks. In all cases, water level records were obtained from tide gauges located at the Oregon Inlet Marina (2km North of Oregon Inlet on the sound side of the island) and the U.S. Army Corps of Engineers Field Research Facility pier in Duck, NC, about 50km north of the inlet.

As noted by Van Weerdenburg (2019), it is difficult to decipher the relative influence of winds from that of waves on tidal inlet hydrodynamics since both processes tend to occur at the same time and in the same direction. It is well known that surface waves may alter surf zone hydrodynamics and water levels on open coast beach faces, coral reefs, and ebb-tidal deltas (e.g., Bowen et al., 1968; Symonds et al., 1995; Faria et al., 1998; Stockdon et al., 2006; Wargula et al., 2014, 2018). Wave induced currents are also responsible for driving alongshore sediment transport and bypassing of inlet systems (e.g., FitzGerald, 1982, 1988; McNinch and Humberston, 2019; Humberston et al., 2019; Velasquez-Montoya et al., 2020). It must therefore be considered that any correlations between wind, water level and current variations in an inlet may be entirely due to wind forced surface waves. At Oregon Inlet (as in many other inlets), wave breaking occurs over the shoals of the ebb tidal delta.

Based on previous results discussed above that the effect of waves on inlet hydrodynamics is significantly reduced several kilometers further inland (Orescanin et al., 2014; Wargula et al., 2014, 2018), we will assume in this study that wave-induced water levels variations and wave-driven currents within the throat of Oregon Inlet (several kilometers inland of the extensive ebb shoal complex) are much less important than pressure gradients and bottom drag. The consequences of this assumption are qualitatively assessed in the discussion.

This study focuses primarily on the relationship between along-channel wind, water level and current variations over subtidal timescales at Oregon Inlet. We first describe the field data collection and analysis procedures. We then quantitatively compare observed subtidal wind variations through the axis of the main inlet channel with subtidal water level gradients and subtidal currents in the same orientation using cross-correlation analyses. The contribution of local and regional wind forcing to along-channel inlet currents is assessed with a simple force balance that includes pressure gradients, surface wind stress and quadratic bed shear stress. Finally, we discuss the broader implications of the findings, the possible consequences of ignoring wave-driven processes along the ebb-tidal shoal complex, and limitations to our understanding of wind-driven tidal inlet hydrodynamics.

3.3 Methods

3.3.1 Data

A field experiment was conducted over a 40-day period from 07 March to 16 April 2019 at Oregon Inlet, NC. Observations obtained include the initial inlet bathymetry, wind magnitude and direction, water levels and currents inside and outside the inlet throat, and wave properties. Topo-bathymetric data were collected at the beginning of the experiment on 07-08 March using a combination of single-beam sonar, RTK-GPS, and LiDAR systems (Forte et al., 2017; Spore et al., 2019; Spore and Brodie, 2017). The seabed elevation data were merged with historical elevation data (Stockdon et al., 2013) to create an updated and continuous 10m resolution digital elevation model (DEM) of the Oregon Inlet system that

includes the primary channel, the flood and ebb tidal deltas, the various channels incising those deltas, and the beach and dunes adjacent to the inlet (Figure 3.2). The DEM shows that the main channel was oriented at an angle of 13° east of true north during the study period, as depicted by the red arrow that also represents the along-channel convention for the positive x-axis used for data analysis. Historical satellite images show that, over the last 25 years, the angle of the primary channel orientation has varied between 10° and 80° relative to true north.

The DEM was used to guide the placement of two instrumented bottom-mounted tripods, one in $3m$ mean water depth on the sound side of the inlet in a channel incising the flood tidal delta, and one in $3.7m$ water depth on the ocean side of the inlet within the primary inlet channel that bisects the ebb-tidal delta. The sound side tripod was equipped with an upward facing $1000kHz$ Nortek acoustic wave and current (AWAC) measuring instrument with pressure sensor. The ocean side tripod was equipped with a $1200kHz$ RDI Sentinel Workhorse acoustic Doppler current profiler (ADCP) with pressure sensor. The vertical position of each sensor was known from the bathymetric survey but was referenced in post-processing to mean sea level (MSL) by averaging the pressure records over the full deployment and assuming no net difference in mean 40-day average water level inside and outside the inlet.

Observations of 6-minute average wind speed and direction (relative to true north) were obtained from a permanent NOAA NOS meteorological station located at the Oregon Inlet Marina on the sound side of the island approximately $2km$ north of the inlet. Water level observations were also collected by a permanent tidal gauge at this location. Wave observations were collected seaward of the inlet by a Spotter Buoy and a NDBC waverider buoy every 1 minute and 30 minutes, respectively, and landward of the inlet by the AWAC every hour. The Spotter Buoy broke from its mooring and was recovered on April 5 and not redeployed. All sensor locations are shown in Figure 3.2, except for the NDBC wave rider buoy that was located approximately $18km$ seaward in $18m$ water depth.

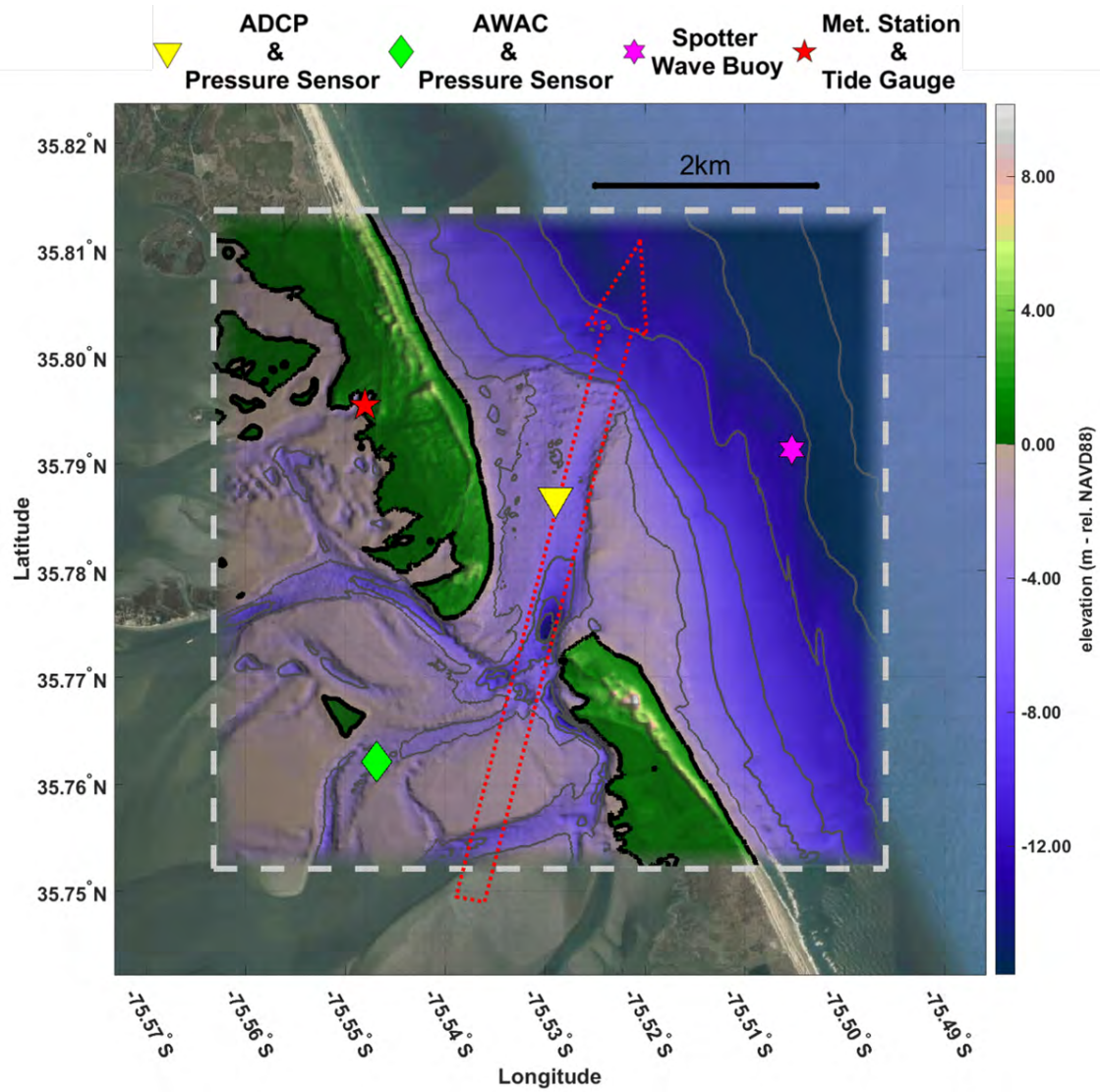


Figure 3.2: The Oregon Inlet field site with bathymetry relative to the NAVD88 vertical datum (approximately MSL), surveyed in March 2019, shown within the dashed gray line. An ADCP with pressure sensor was deployed on the ocean side of the inlet within the main inlet channel (yellow triangle), and an AWAC with pressure sensor was placed on the sound side of the inlet (green diamond). A spotter wave buoy was moored offshore of the ebb-tidal delta (magenta star) and a meteorological station was located at the Oregon Inlet Marina (red star). The red arrow indicates the orientation of the main ebb channel (13° rel. true north) and the orientation of the positive x-axis used in data analysis and force balance.

The anemometer at the Oregon Inlet Marina meteorological station was at a height of 6.7 m above MSL. Time series of wind speed and direction are shown in Figure 3.3.1. There were strong multi-day variations in wind speed (ranging 0-10 m/s) and direction (including rapid wind reversals) associated with the passage of atmospheric frontal systems. The raw wind data were interpolated onto a 15-minute interval time vector spanning the study period that is used as a common time vector for all observations. Also shown in Figure 3.3.1 is the wind rose indicating that the prevailing wind patterns at Oregon inlet over the course of the experiment were from the NNE and from the SSW, generally in alignment with the orientation of maximum fetch across the Pamlico sound as well as that of the main channel of the inlet.

The AWAC and ADCP sampled currents (in 0.25 m vertical bins spanning the water column) and near-bottom pressures continuously at 1 Hz and that were then ensemble averaged over 10- and 1-minute intervals, respectively, for the 40 days from 13 March to 16 April. The observations of the current from the ADCP and AWAC exhibited typical vertical variation in magnitude with depth associated with influences by the bottom boundary layer. Current direction did not vary significantly with depth and the phase of the currents remained generally consistent throughout the water column. As such, the current observations are simplified by depth-integrating over the water column at the sensor locations. The depth integrated current data was then interpolated onto the 15-minute incrementing common time vector. The resulting time series of observed depth-averaged current magnitudes and directions (relative to true north) for the ocean ADCP and sound side AWAC are shown in Figure 3.4. Strong tidal oscillations are observed throughout the 40-day record with reversals in the current occurring rapidly over time periods of a few minutes. Current magnitude ranged from 0 – 1.5 m/s . There was some variation in the nature of the rotational structure of the reversing currents throughout the course of the experiment, as seen in previous observations of tidal and subtidal currents in inlets (e.g., Lippmann et al., 2013a,b), but the details of the rotational behavior were beyond the scope of this study and are not discussed further.

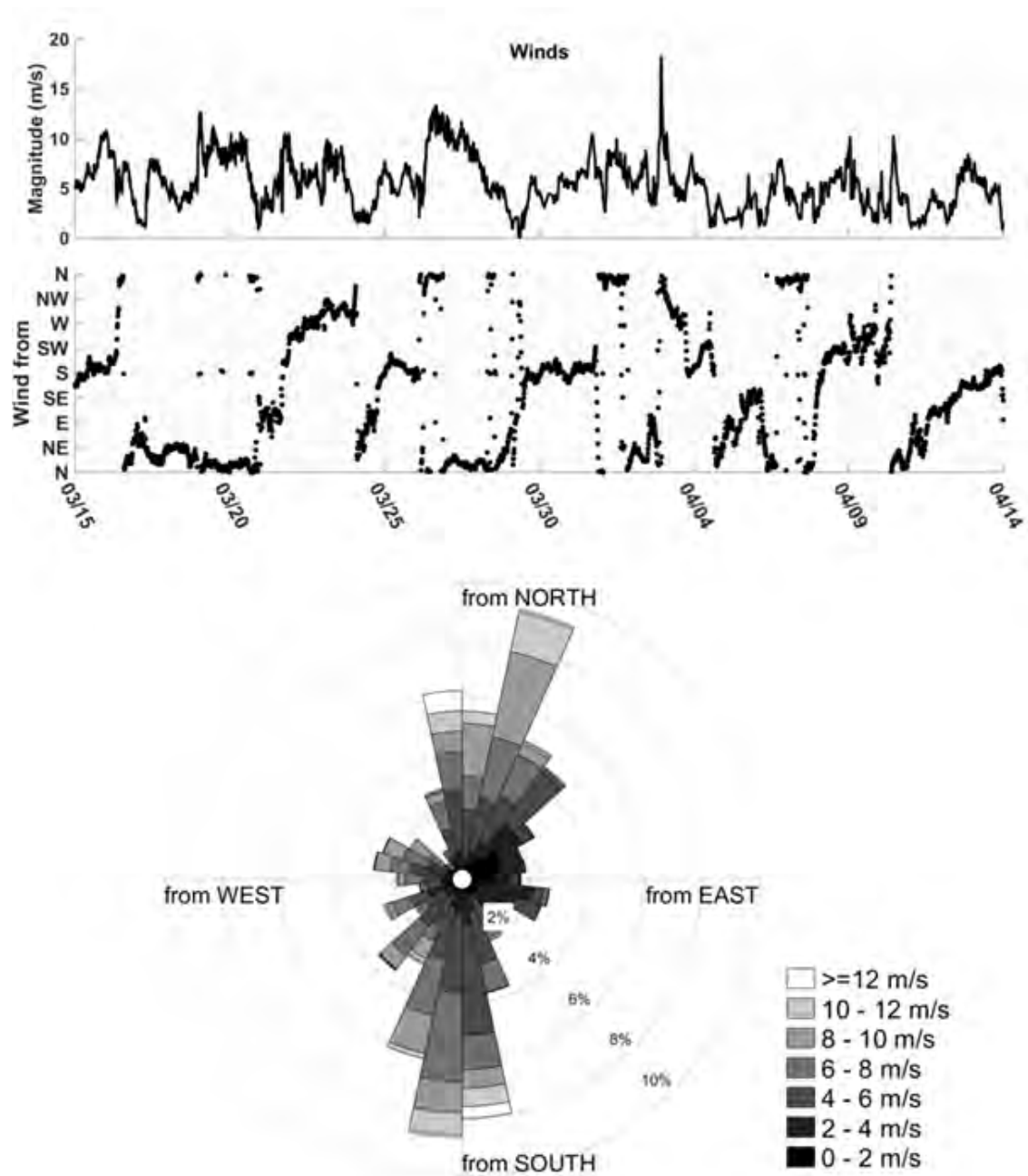


Figure 3.3: Time series of observed wind speeds (top) and directions (middle) over the 40-day study period. (Bottom) A wind rose shows the dominant wind directions during the experiment

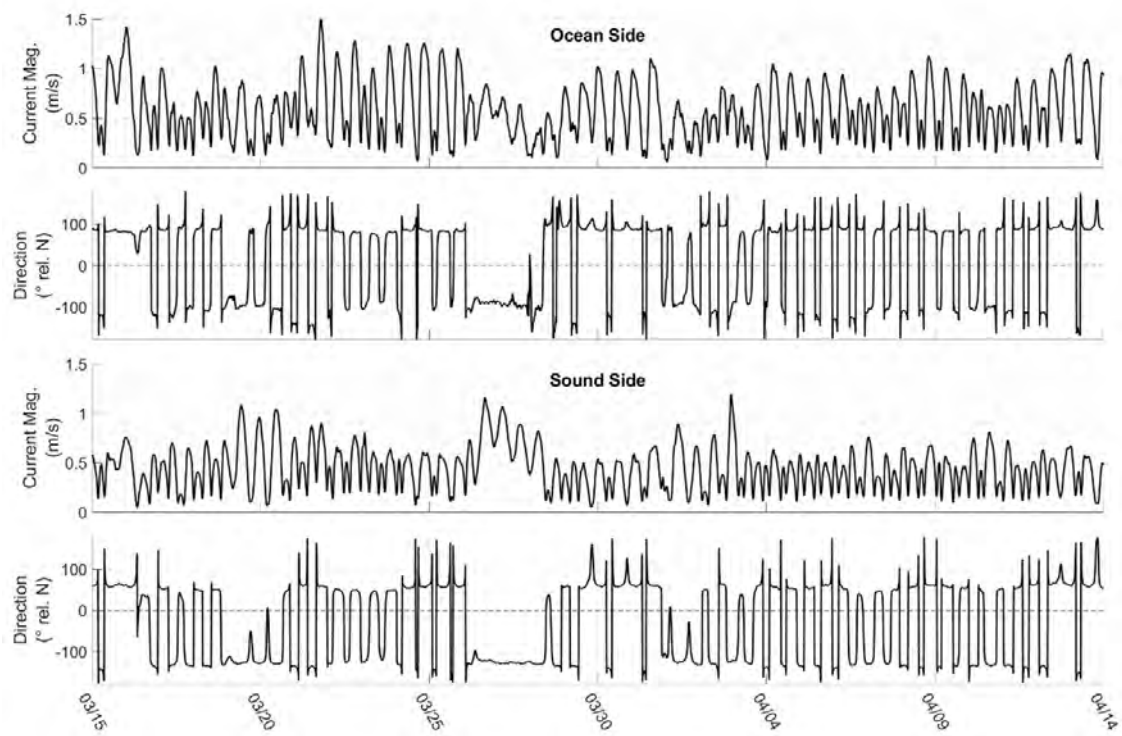


Figure 3.4: The Ocean side observed current magnitude (top) and direction (2nd from top) and the Sound side observed current magnitude (3rd from top) and direction (4th from top) for the 40-day study period.

Time series of the observed water levels from the ADCP (ocean side) and AWAC (sound side) sensors are shown in Figure 3.5. The datum for the water levels was determined by comparing the approximate water depths estimated from the bathymetric survey with the average water depth estimated from the pressure sensor over the 40-day record. Each sensor tripod was buried somewhat by sediment accretion at the sensor locations over the course of the experiment, but comparisons of the mean pressure and the bathymetric survey suggest that the elevation of the sensor itself did not change more than a few cm. Errors in the elevation of the mean water levels would affect the magnitude of the pressure gradient observed between the two sensors but were small compared to the magnitude and time scales of observed water levels modulated by the tides and subtidal forcing. The magnitudes of the tidal water level oscillations ranged about $0.4 - 1.5m$ on the ocean side. Tidal amplitudes were significantly attenuated through the inlet as observed in other tidally choked inlets (e.g., Lippmann et al., 2013b; MacMahan et al., 2014). Consequently, the range in tidal water levels on the sound side, $0.1 - 0.7m$, were reduced 50-75% compared to the ocean side data. The water level records from both the ocean and sound side show significant modulations at frequencies much lower than the tides (subtidal).

The wind and current velocities components along the axis of the primary inlet channel (deg 13 rel. true North, with the positive axis direction oriented towards the ocean) were extracted and are shown in Figure 3.5. It can be noted that the current measured by the ADCP in the primary inlet channel is ebb dominant, likely a consequence of its location where ebb currents are at a maximum while flood currents are more dispersed owing to strong flood flows through the marginal flood channels. While not a primary focus in this study, the significant wave height observations are also shown in Figure 3.5 for reference and later discussion.

The raw water level and along channel current time series were subjected to a tidal analysis (using T_{TIDE} ; Pawlowicz et al., 2002) to remove the tidal constituents from the raw time series. A low-pass filter with a $33hr$ half-amplitude period was applied to the de-tided

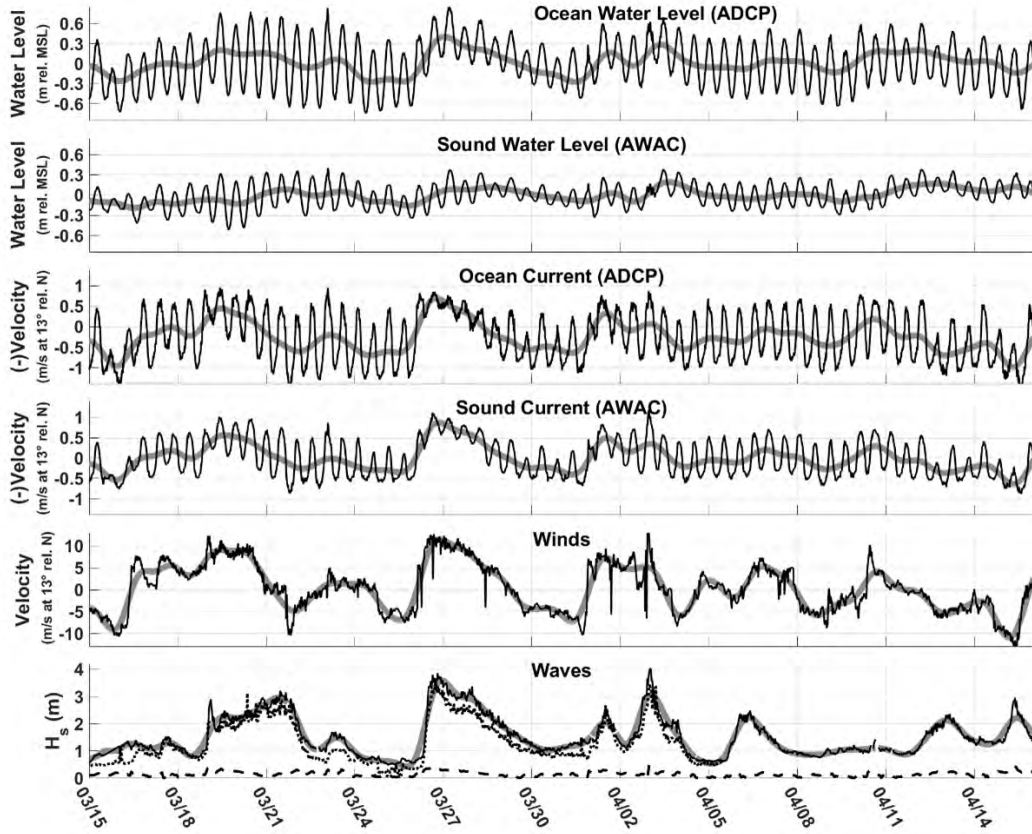


Figure 3.5: Observed (thin lines) and filtered subtidal (thick lines) time series. Water levels for the ocean side ADCP (top) and from the sound side AWAC (2nd from top). Along-channel current speed for the ocean side ADCP (3rd from top) and sound side AWAC (4th from top). Along-channel wind speed from the meteorological station at Oregon Inlet Marina (5th from top). Significant wave heights (bottom) from the offshore waverider buoy (black line), the spotter buoy just seaward of the ebb-tidal delta (dotted black line), and the sound side AWAC (dashed black line), with the subtidal signal shown only for the waverider buoy timeseries.

water level and along channel current time series, as well as the along channel wind and the wave times series using the pl66tn filter , (Beardsley et al., 1977; Alessi et al., 1985; Beardsley et al., 1985, 2004) to isolate subtidal variations from other higher frequency oscillations. The resulting subtidal variations are overlain on the raw time series in Figure 3.5. During the 40-day study period, the magnitude of the along-channel subtidal current (henceforth referred to as the ST current) surpassed the magnitude of the astronomical tidal current 32% of the time and was at least half as strong 58% of the time. Even though no major storms occurred during this study period, it is clear from these results alone that a non-tidal process alters the currents in Oregon Inlet significantly and consistently.

Time series of the subtidal water level gradient (herein referred to as the STWL gradient) was calculated by subtracting the ocean side from the sound side subtidal water level records and dividing by 3.18km , the horizontal distance between the sensors. Timeseries of the STWL gradient, subtidal wind, and ST current (from the main channel ADCP) from both the sound and ocean sensors are shown in Figure 3.6. Clearly shown is that the temporal variation in the subtidal components of the winds, water level gradient, and inlet currents closely follow the same pattern, suggesting a relationship between wind forcing and both the pressure gradient through the inlet and the flow response.

Time-lagged cross-correlations (R ; Figure 3.7) show that the subtidal winds are in-phase and strongly coupled to both the STWL gradient ($R = 0.86$ at zero lag) and ST current ($R = 0.92$ at near zero lag with Ocean side ADCP), with the winds accounting for 74% and 85% of the variance (based on R^2 values) in along-channel pressure gradient and along channel currents, respectively. While low pass filtered time series will tend to increase correlations, the de-tided but unfiltered forms of these time series remain well correlated ($R=0.78$ for winds and pressure gradient, and $R=0.81$ for winds and currents), suggesting that winds are a likely driver of the hydrodynamic force balance within the inlet. There are two ways that the wind may be driving the currents in the inlet. The local surface wind stress can directly drive the current and the regional wind can force differential setup(down) through

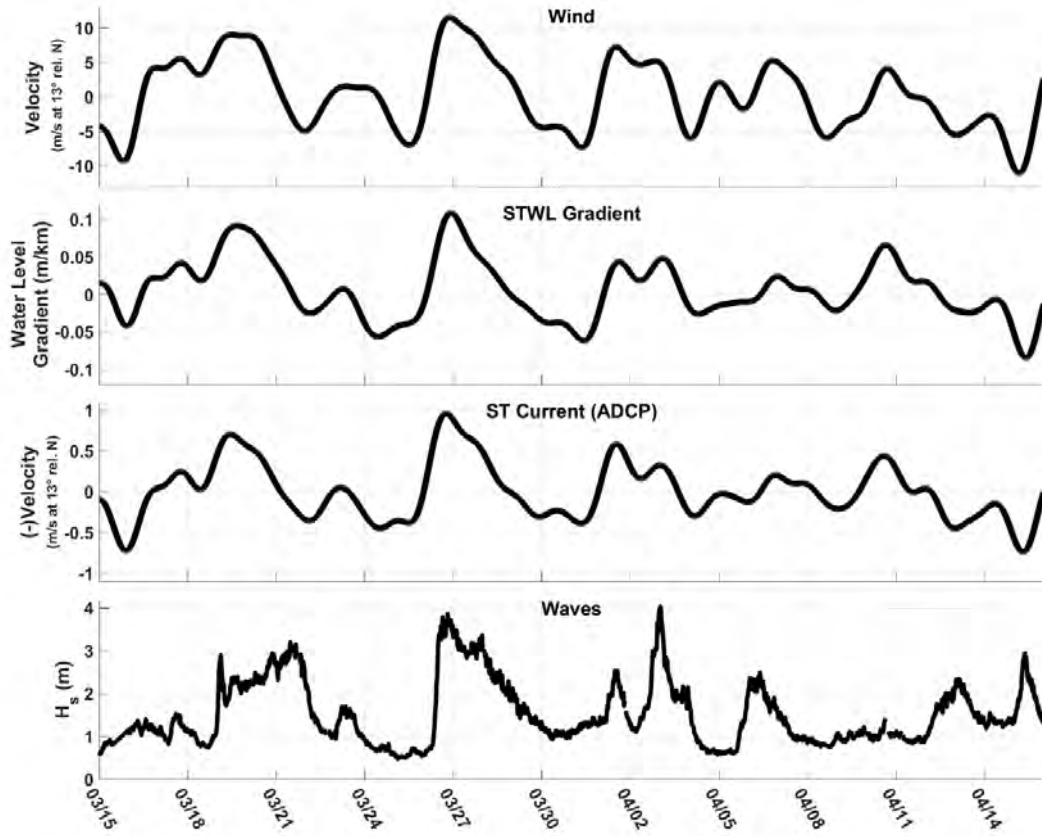


Figure 3.6: Subtidal time series for the along-channel wind speed (top), STWL gradient (2nd from top), and ST currents from the main channel ADCP (3rd from top), and the raw significant wave height time series (bottom).

the inlet that induces a pressure gradient and subsequently a flow. While the first scenario is perhaps the simplest explanation, the second scenario is not improbable given that the component of the winds orthogonal to the orientation of the island are expected to increase the water level on one side of the island chain and decrease it on the other, thus creating a pressure gradient through the inlet (as found during a large wind event discussed in Safak et al., 2016). Additionally, the prevailing winds in this area are from the SSW and NNE (Figure) which aligns well with the orientation of the main inlet channel as well as the orientation of maximum fetch across Pamlico Sound (also noted by Safak et al., 2016). Because the influence of both local surface wind stress and regional wind-induced pressure gradients would tend to be in phase and in the same direction, it remains unclear the relative contributions to the net forcing of the along-channel subtidal inlet flows.

3.4 Force Balance

To examine the relative contribution of the winds to the subtidal currents through the inlet, a simple 2-D force balance is considered. Ignoring momentum fluxes from wave radiation stresses (assumed to be mostly localized to areas of wave breaking over the ebb-tidal delta) and inertial currents, the steady force balance is given by

$$\tau_b = \tau_w - \rho_w g (h + \overline{\eta_w}) \frac{\partial \eta_w}{\partial x} \quad (3.1)$$

where $\frac{\partial \eta_w}{\partial x}$ is the along channel sea surface slope over the inlet distance ∂x between the ADCP and AWAC, (η_w) is the mean sea surface elevation across the inlet, τ_w is the local surface wind stress across the inlet, τ_b is the bed shear stress, h is the mean water depth of the inlet, ρ_w is the density of sea water, and g is gravity. As previously stated, the subtidal sea surface fluctuations are assumed to be the result of wind-driven processes and that surface gravity wave-induced changes to the low-frequency water level fluctuations at the locations of the sensors are negligible. Atmospheric barometric pressure fluctuations would affect (η_w) ,

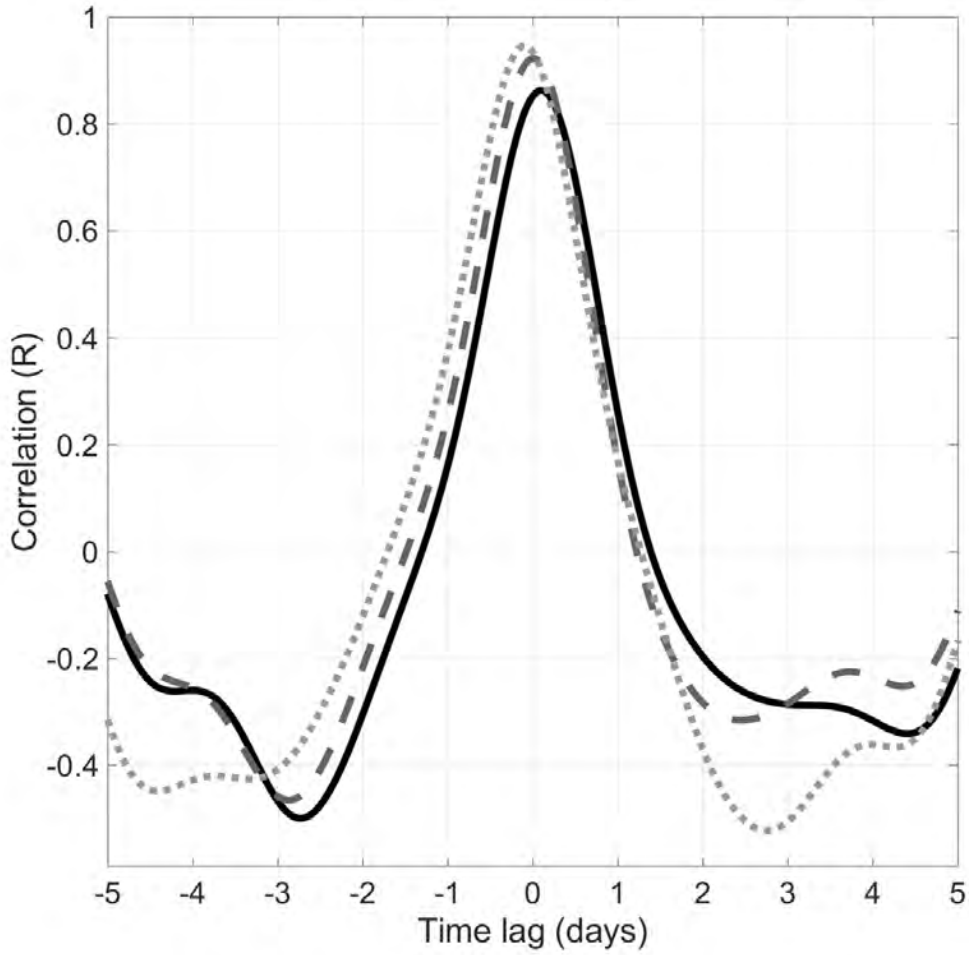


Figure 3.7: Time-lagged cross correlation between the along-channel component of wind speed and the sub-tidal water level gradient (solid), between the along channel component of the wind and the sub-tidal ST current (dashed gray), and between the sub-tidal STWL water level gradient and the along-channel component of the ST current (dot-dashed light gray).

but the magnitude of this effect is small (of order 0 to 0.3m) relative to the average water depth of the inlet (about 12m) and is ignored. The influence of barometric pressure on the STWL gradient are also expected to be negligible because the scales associated with the passing of atmospheric fronts are much larger than the scale of the inlet.

The wind stress enters (3.1) in two ways: by driving the mean pressure gradient across the inlet (observed by the observations of water levels on either side of the inlet), and by directly applying a surface stress to the water column. The surface wind stress, τ_w , is described by a quadratic drag given by

$$\tau_w = f_w f_r \rho_a C_f U |U| \quad (3.2)$$

where U is the observed along-channel wind speed 6.7m above the sea surface, $f_w = \ln(10z_o) / \ln(6.7z_o)$ is a wind velocity correction factor that converts wind speeds observed at 6.7m elevation to 10m elevation assuming a logarithmic wind profile and a local topography roughness height, z_o , f_r is a roughness correction factor for coastal zones, ρ_a is the density of air (assumed to be 1.22 kg/m^3), and C_f is a surface wind drag coefficient. The local roughness elements, z_o , are assumed to be 2m due to the topography and structures across the barrier islands that alter the vertical profile of the wind. The roughness correction factor, f_r , is used to account for the increased roughness element over coastal waters relative to open ocean conditions and is estimated to be 2.5 based on work by Ortiz-Suslow et al. (2015). The ocean surface drag coefficient, C_f , typically varies as a function of wind velocity, and was estimated following Large and Pond (1981) with (3.3).

$$C_f = \begin{cases} 1.14 \times 10^{-3} & \text{for } U_{10} \leq 10 \text{ m/s} \\ 0.49 + 0.065 \times 10^{-3} \times U_{10} & \text{for } U_{10} \geq 10 \text{ m/s} \end{cases} \quad (3.3)$$

The bottom drag, τ_b , is approximated with a quadratic velocity with

$$\tau_b = \rho_w C_d V |V| \quad (3.4)$$

where C_d is a bottom drag coefficient, and V is the depth-averaged along-channel current velocity. C_d varies as a function of sediment characteristics, seabed roughness, and bedform morphology, and for this case was approximated as 0.05, a value proposed by (Wargula et al., 2014) for New River Inlet, NC, a somewhat similar but smaller-scale environment to that of Oregon Inlet.

The depth-averaged current through the inlet is estimated from (3.1) with and without local wind drag and compared to the measured current (Figure 3.8). The current resulting from the pressure gradient forcing associated with the wind-induced STWL gradient captures the majority of the current (with $R = 0.95$, accounting for 89.9% of the variance). Local wind drag was found to be generally insignificant with correlations that include the effects of local wind drag explaining less than 1% more of the variance of the observed currents. We note that changes to the current magnitudes increased during the strongest wind events, a result possibly owing to increased wind drag through the inlet, or potentially wave influence not included in this force balance.

In general, the simple force balance better predicts ebb current magnitudes than flood currents, perhaps a result of omitting inertial currents in the force balance (3.1), as also found by Wargula et al. (2018), but this may also be simply due to the location of the ADCP sensor within the main ebb channel. A significant portion of the flooding tide moves through the marginal flood channels before entering the inlet throat, thus bypassing the sensor on the ocean side. Even so, this effect appears to be relatively small, with the model correlations still strongly suggesting that water level gradients along the inlet channel are the predominant forcing of inlet currents, with local wind drag, wave effects, and inertial currents acting as lower order influences.

For a consistency check of the sea surface elevation on the sound side of the inlet, the wind surge induced by regional winds across Pamlico sound is approximated with a finite difference

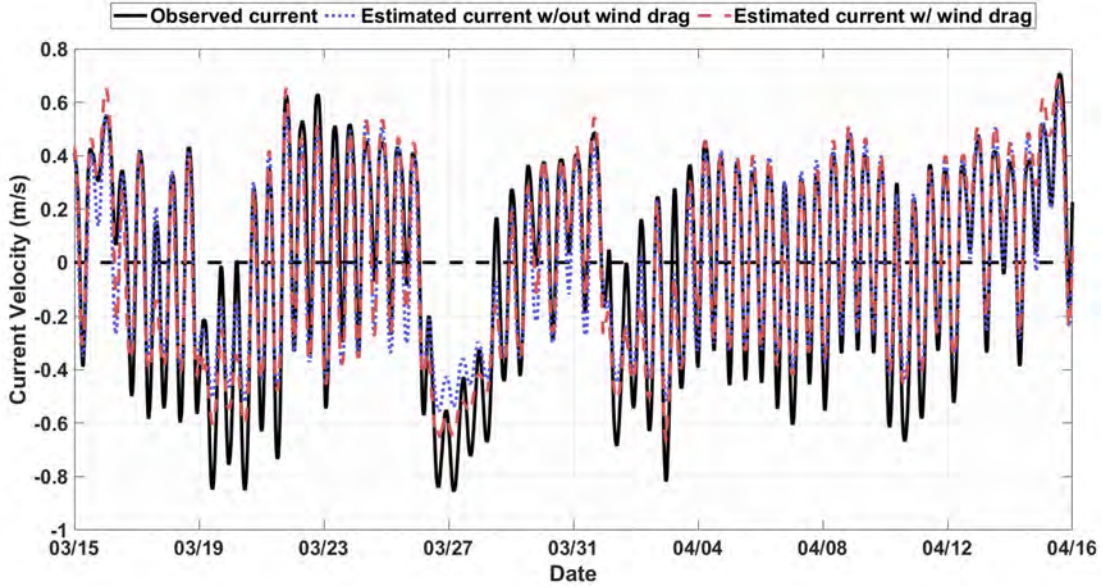


Figure 3.8: Time series of the observed along-channel ST current (black solid line), and the predicted current based on a force balance using the STWL pressure gradient without wind drag incorporated (dashed blue line), and the predicted current based on the STWL pressure gradient including the surface wind stress (red dashed line).

approach using the geographically defined fetch in the orientation of the main channel (deg 13 east of true north), the observed wind speed, and a uniform bathymetry representative of the shallow sound. The wind induced setup on the sound side of the inlet is iteratively solved using (3.1) for the total depth in 10m increments over the approximately 75km fetch length. The bottom drag, C_d , is estimated as 0.003 after Roelvink and Van Banning (1995) for similar environments as Pamlico Sound. For 5, 7 and 10m/s winds, the wind setup on the sound side of the inlet is estimated to be 0.08, 0.15 and 0.30m, respectively. A least squares fit is found between the observed wind and non-tidal component of water level at the Oregon Inlet Marina located near the inlet (a location less influenced by inlet processes than the AWAC). For the same wind speeds, the observed water level modifications at the tidal gauge are 0.09, 0.14 and 0.19m, respectively. This suggests that the observed subtidal water level fluctuations, which dictate the STWL gradient, are of the appropriate magnitude to have been induced by regional winds. This is supported by other studies that modeled wind surge due to winds in the Pamlico Sound (Mulligan et al., 2015).

3.5 Discussion

The simple force balance (3.1) suggests that tides and winds are the dominant forces controlling the hydrodynamics within the main channel of Oregon Inlet as they account for 90% of the variance of the along-channel subtidal current (see Figure 3.8). Waves are often considered to be of first order importance to tidal inlet hydro- and morpho-dynamics, and unlike with tides, waves result from local and regional winds and get larger with winds blowing landward and smaller with winds blowing seaward. This results in wave momentum fluxes approximately in-phase and in the same direction as the wind forcing. Thus, there is likely some degree of correlation between wave forcing and the observed ST current because the winds force both and in the same direction. This is qualitatively observed during a storm front that passed on 25-28 April producing large 4 m significant wave heights from strong north winds (Figure 3.9). The largest wave height and largest STWL gradient both coincide with the period of the strongest winds out of the north, and fade as the winds fade. The STWL gradient becomes negative as the winds rotate to the south. On the other hand, a large wave event on 14-15 April produced 3m significant wave heights driven by winds out of the south but the STWL gradient remained sharply negative in opposition to any potential wave influence (Figure 3.10). Similar situations occurred several times during the study period, suggesting that, while waves may alter water levels over the ebb tidal delta near breaking locations, their influence is either small compared to wind induced surges, or highly localized to the ebb-tidal delta. In either case, the strong agreement between observed and predicted ST currents also supports that wave influences at this area are of a lower order than pressure gradients induced by regional winds.

With evidence to suggest that winds may be an additional first order influence on tidal inlet hydrodynamics, it is worth considering how this mechanism fits into the traditional theory that assumes inlet hydrodynamics and morphology result from a balance of astronomical tides and surface gravity wave forcing. Winds produce a water level slope through

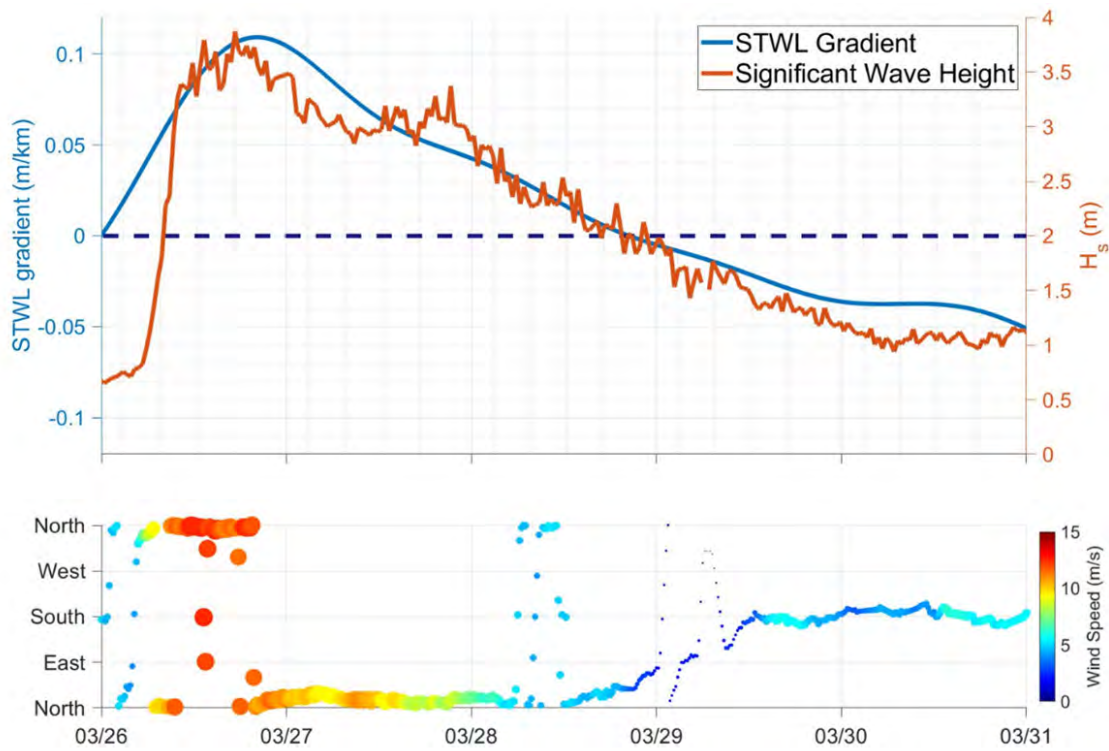


Figure 3.9: Observations during storm waves with strong winds out of the north (upper panel). Time series of STWL pressure gradient (blue line) and offshore significant wave height (orange line) as measured by a wave rider buoy (NDBC station 44095). (lower panel) Time series of wind direction with wind speeds indicated by the color scale on the right-hand-side.

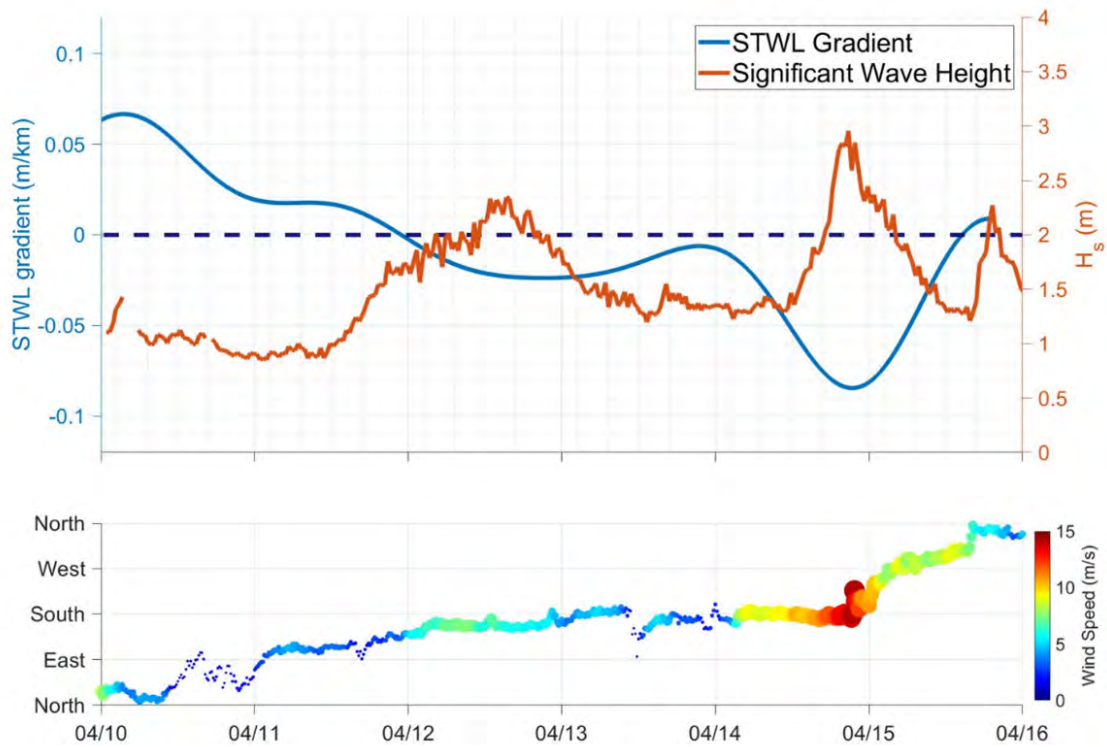


Figure 3.10: Observations during storm waves with strong winds out of the south (upper panel). Time series of STWL pressure gradient (blue line) and offshore significant wave height (orange line) as measured by a wave rider buoy (NDBC station 44095). (lower panel) Time series of wind direction with wind speeds indicated by the color scale on the right-hand-side.

the inlet that forces a flow in the opposite direction of the gradient. However, wind forcing generally varies over longer timescales decoupled from the predictable astronomical tides. Instead, the STWL gradient is linked to regional wind patterns that vary more irregularly and unpredictably. Furthermore, wind effects on hydrodynamics is strongly dependent on the geographic setting and bathymetry of both the ocean and inland water body. This is to say that the net gradient through an inlet strongly affected by winds is complex and challenging to predict.

This is the case for NOAA's Tides and Currents water level predictions near Oregon Inlet. Water levels are recorded on the ocean side of the inlet 50 km to the north at the U.S. Army Corps Field Research Facility pier in Duck, NC, where the mean tidal range is approximately 0.98 m . During 2019, the predicted water levels based solely on astronomical forces had a root mean square error (RMSE) of 0.23 m , or 24% of the mean tidal range when compared with observations. This issue is exacerbated in the sound where the tidal range is attenuated through the inlet. At Oregon Inlet Marina, where the tidal range is approximately 0.28 m , the 2019 water level RMSE was 0.25 m , or 90% of the astronomical tidal range at this location, greatly reducing the effectiveness of predictions used by mariners. The inability to accurately predict water levels around Oregon Inlet, and consequently to estimate the inlet currents, has increased challenges to navigation as well as dredging and other engineering efforts.

Capturing the complex interaction of wave and inertial processes in any detail would require a numerical model with broad coverage to capture the regional wind influence, as well as accurately tuned boundary conditions to properly simulate tides, waves, wave-driven flows, and local wind effects. However, for improving the high volume of operational forecasts needed at inlets, a simpler empirical approach may suffice for practical purposes. The data from this study show there is a relatively linear relationship between wind speed through the axis of the main inlet channel and the resulting STWL gradient (Figure 3.9). A linear fit line indicates that, on average, the STWL gradient through the inlet increases in magnitude by 3.4 cm/km for every 5 m/s positive increase in the wind speed in the along channel direction.

This predicted subtidal water level gradient can then be added to the water level gradient associated with astronomical tides and used to estimate inlet currents (Figure 3.11). Using this methodology to modify current estimates at Oregon Inlet during the study increased the explained variance of the observed currents velocity (R^2 values) by 39% compared to simply using the predicted tides. There is more uncertainty in forecasted winds, but short term predictions (3 – 5 days) would almost certainly improve prediction of the flood and ebb inlet current magnitude and phase, a useful prediction to improve navigational safety to local mariners.

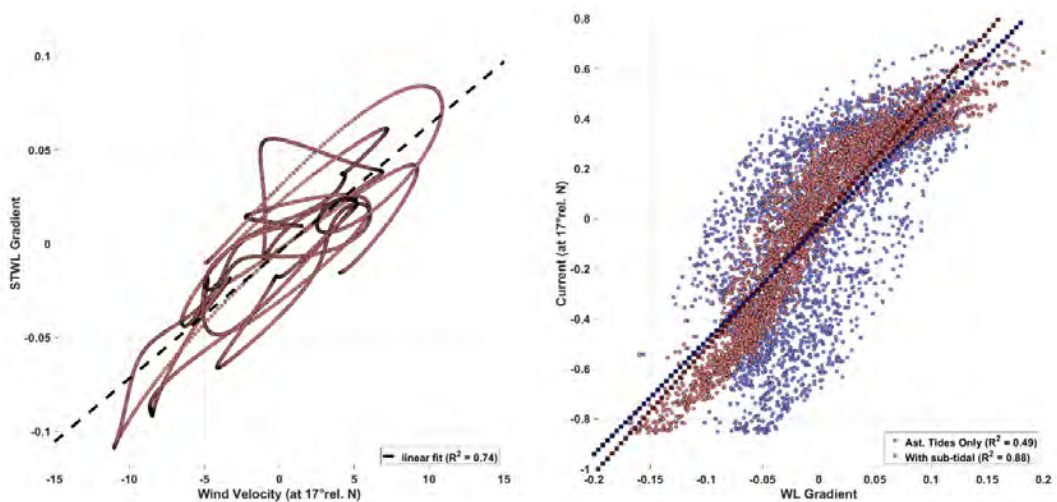


Figure 3.11: (left) STWL gradient as a function of the along-channel wind velocity. Linear regression is shown by the dashed black line with R^2 value of 0.74. (right) The observed current as a function of the water level gradient only associated with astronomical tides (blue; $R^2=0.49$), and as function of the water level gradient that includes tides and the wind-forced STWL gradient from wind forcing (red; $R^2 = 0.88$).

Finally, the inclusion of wind as a first order term at Oregon Inlet raises interesting questions about how the morphology of this system fits into the traditional spectrum of inlet morphology based on the ratio between tidal and wave energy. Do wind effects cause the system to behave like one with a larger tidal range, a smaller one, or in some entirely new way? These questions are not easily answered with the hydrodynamics measurements collected in this experiment, but preliminary evidence from remote sensing in another study suggest a re-

lationship does exist between the STWL gradient and bedform movement over the ebb-tidal delta (McNinch and Humberston, 2019). Another question raised is whether the seasonality of winds may introduce a seasonal signal in inlet hydro- and morpho-dynamics. An extensive record of the frequency of fronts in the northern hemisphere at this latitude shows that fronts typically pass every 3 days in summer and every 8 days in winter, with winter winds generally reaching higher magnitudes (Schumann and Van Rooy, 1951). Does the frequency and magnitude of weather fronts and the winds they create add a seasonal component to inlet hydro- and morpho-dynamics? The answers to these questions could be addressed with a combination of in situ and remote sensing measurements coupled with publicly available hydrodynamic and sediment transport models, and is the subject of ongoing research.

3.6 Conclusions

Observations of winds, water levels and currents were obtained over a 40-day period at Oregon Inlet, NC, in the Spring of 2019. A component of the along-inlet current varies on subtidal time scales unassociated with astronomical tides. The magnitude of this subtidal currents has magnitudes that exceed the tidal current approximately one third of the time. The along-channel component of the current is well correlated with the subtidal component of the water level gradient through the inlet accounting for 89% of the variance. Both the subtidal water level gradient and the subtidal current are well correlated to the component of wind blowing through the main axis of the inlet, accounting for 74% and 85% of the variance, respectively.

A simple wind surge forcing model demonstrates that the observed water level modifications that produce the subtidal gradient are likely due to regionally induced wind setup(down) on either side of the inlet. A force balance at the inlet confirms that the subtidal current results primarily from the subtidal water level gradient, with local wind drag only slightly altering the net current. These results provide strong evidence that regional winds may alter tidal inlet hydrodynamics to an extent comparable with tides. The intensity of

wind influence likely depends on geographic setup, including the size and bathymetry of the inland water body.

Most tidal inlets, including other meso-scale tidal inlets like Oregon Inlet, are still classified by the relative strength of astronomical tides and waves in the region, without consideration of wind forcing. The results from this study show that winds will at times accelerate tidal currents, and at other times retard or even reverse them, suggesting the traditional classification may not always be appropriate. Preliminary evidence from a remote sensing study (McNinch and Humberston, 2019) showed that bedform movements over the ebb-tidal delta at Oregon Inlet are also correlated with the subtidal water level gradient, though ambiguity in this relationship remains owing to the use of breaking patterns to imply morphology. Further studies are required that include numerical modelling to determine if a tidal inlet morphology will evolve significantly differently with the addition of wind forcing.

CHAPTER 4

Idealized simulations of tidal inlet morphologic responses to wave, sub-tidal water level gradients and engineering modifications

4.1 Abstract

Innumerable coastal forces, acting simultaneously, instigating feedback loops, and further modified by human intervention, are responsible for the complex morphodynamics of tidal inlet systems. This study utilizes an idealized modelling approach via the Delft-3D modelling suite to isolate morphologic responses from specific forcing alterations. The model is run over a synthetic topo-bathymetric surface depicting large scale characteristics of Oregon Inlet and the northern Outer Banks (NC, USA). A 180 day initial simulation allows tidal and simple wave forcing to develop a realistic inlet system including deltas and channel systems. The end state is then branched into 4 separate simulations where 1) maintains the same forcing to serve as a control, 2) varies wave angle by 45 degrees, 3) adds sub-tidal oscillations to the sound-side water level, and 4) introduces an impermeable terminal groin feature to one side of the inlet based on the setup at Oregon Inlet. The morphologic evolution and sediment transport resulting from 2, 3 and 4 are compared to the control scenario to assess bulk changes associated with each individual forcing alteration. Modifying the incident wave angle skews the ebb-tidal delta in the longshore direction. Sound-side sub-tidal oscillations, like those observed on the Outer Banks due to winds, modify the through-inlet transport patterns and alter the lateral extents of the flood and ebb tidal deltas. A terminal groin positioned on the terminus of the southern island causes an angling of the main tidal inlet relative to the shoreline orientation, a pattern also observed at Oregon Inlet.

4.2 Introduction

Barrier island systems exist world-wide (Stutz and Pilkey, 2001), and almost all of them have tidal inlets that divide individual spits and islands and connect the ocean to the back bay. The size and spatial frequency of tidal inlets largely depends on the regional tidal range but may also be modified by the wave climate, sediment availability and other local influences (Hayes, 1979). New tidal inlets may be generated during storm events as water levels rise particularly high along one side of a land mass, eventually causing a breach as the hydraulic gradient forces water to flow over the land. Because barrier islands are usually composed of unconsolidated sand, this may quickly excavate a large volume of sediment and form a new inlet, though the long-term fate of such breaches is variable (Hayes and FitzGerald, 2013).

Once developed, inlet system morphology may continue to be dynamic; channels and shoals frequently meander over the shallow deltas that develop on either side of the inlet. A skewed wave climate can cause full system mobility as the up-current landmass extends as a recurring spit and the down current landmass is eroded by the shifting main ebb channel (Hayes, 1980; Nienhuis and Ashton, 2016; Dissanayake et al., 2009). Consequently, many coastal communities install hard structures such as jetties or groins. This tends to stabilize the inlet positions, but the greater challenge is in understanding how these structures influence sediment transport patterns and inlet morphodynamics. Tidal inlets and their associated deltas may be a source or sink of sediments to the regional coastline, so their sediment dynamics are an important consideration for broader barrier island evolution. (Hayes et al., 1970; Hayes, 1980; Hayes and FitzGerald, 2013; FitzGerald, 1982; Fitzgerald et al., 1984).

And while tides and waves have traditionally been the primary, if not only, considerations in analyses of inlet morphodynamics, there are potentially other important processes contributing to inlet morphodynamics. At Oregon Inlet, a large inlet system located on the northern part of the Outer Banks, regional winds were found to be a first-order control of

current variations over sub-tidal time scales (Humberston et al., 2019)(Humberston et al., 2021 - In Review). In a remote sensing study of the ebb tidal-delta at Oregon Inlet, Humberston et al. (2019) found a strong correlation between the wind induced gradient and the and cross-shore movement of shoals on the ebb-tidal delta, evidence that winds affect inlet and delta morphology.

However, even with remote sensing capabilities, it remains difficult to make the observations necessary to derive causal relationships. Instead, numerous inlet studies have turned to discrete numerical models to capture processes not easily measured by observations (Bertin et al., 2009; Olabarrieta et al., 2011; Elias et al., 2006; Wargula et al., 2014; Provan et al., 2018). In many cases, site-specific models have proven useful in providing locally relevant quantitative guidance for maintenance dredging or engineering projects. The intricacies of a model tuned to a specific site, however, tend to also limit insights to that specific inlet. An alternative approach is to create an idealized model to simplify and isolate facets of an inlet system while holding other conditions constant. Olabarrieta et al. (2014), for example, used a numerical model to simulate simplified and controlled forcings on a synthetic topobathymetric surface to inspect the feedbacks between ebb-jet currents and waves. Mariotti and Murshid (2018) use an idealized modeling approach that fully averaged tides to explore long term trends in inlet system morphodynamics.

Numerical modeling is a useful tool for examining morphodynamic patterns that are still not well understood despite a relatively strong grasp of the underlying physics. The challenge addressed by models is that morphology evolves not just due to individual grain scale physics, but the innumerable interactions and evolution of these processes occurring over both space and time. While there are continued challenges in properly tuning the various parameterizations required to simulate the fine scale physics of sediment transport, numerical models are well suited to capturing the illusive spatial and temporal dependencies of morphodynamics.

It should be noted that morphology differs from bathymetry in that it is not a quantitative

measure of elevations, but rather a relative measure of characteristics of the shape of a surface. While there is inherent ambiguity in this qualitative measure, it remains valuable for at least two reasons. First, it is often possible to make accurate assessments of morphology (generally via remote sensing) but not bathymetry. Second, morphology is a measure of shape and thus lends itself to capturing relative relations that may exist at varying scales. This may be seen in the presence of some coastal shapes (such as channels and sinusoidal bedforms) and hydrodynamic processes (such as eddies) across a wide range of spatial scales; the relation between the hydrodynamics forces and the morphology can be relative.

This study uses an idealized modeling approach to isolate and examine how three simple variables (wave angle, sound side sub-tidal oscillations and an engineering structure) may alter tidal inlet system morphology. Because it is impossible to verify an idealized model, all deductions remain necessarily qualitative and the primary focus remains on bulk morphologic patterns. These patterns, though not easily related to exact elevation changes, are useful approximations of how these significant forcing and structural changes are likely to modify bulk inlet system morphology.

4.3 Methodology

The Delft-3D modeling suite (herein D-3D) applied in this study solves the two-dimensional depth-averaged continuity equation and horizontal momentum equations with an assumption that the vertical momentum equation can be reduced to the hydrostatic relation by considering gravity to be the dominant vertical force (Roelvink and Van Banning, 1995; Lesser et al., 2004; Gerritsen et al., 2007). The software is structured as modules so that hydrodynamics (simulated within the FLOW module) can be coupled with waves (simulated within the WAVE module) to simulate current-wave interactions. The WAVE module employs the third generation Simulating Waves Nearshore (SWAN) model (Booij et al., 1999). A 2-way online coupling is used to capture the influence of currents on waves and vice versa [D-3D WAVE manual].

4.3.1 Domain Setup

An initial 17km by 17km synthetic topo-bathymetric surface was created based loosely on major characteristics of the Outer Banks barrier island system and its northern most inlet system, Oregon Inlet (Figure 4.1 - top). The artificial surface was constructed with 5m resolution and includes a 10km (cross-shore) by 17km (alongshore) back bay with a constant 3m depth representative of the shallow Pamlico and Albermarle Sounds on the landward side of the Outer Banks. The sound is separated from the ocean by a 300m wide island of a convex sinusoidal shape extending to a height of 3m (Figure 4.1 - middle). The nearshore and offshore profiles were determined by equation 4.1 using empirical constants estimated for the Outer Banks by Lippmann et al. (1999) where the nearshore slope (β_1) is 0.07, the offshore slope (β_2) is 0.0064, the first coefficient (α_1) is 2.93 and the second coefficient (α_2) is 0. The x term defines the cross-shore position and h is the resulting elevation at that location. The zeroing of the second coefficient indicates that the entire last term is 0 and so defines a non-barred beach profile so that the bar position indicated by x_c is irrelevant (Lippmann et al., 1999; Putrevu and Svendsen, 1992). The offshore profile extends 6.5km from shore to a depth of 45m. A simple inlet separates the northern landmass from the southern landmass in the center of the domains North-South extent. The inlet is concave sinusoidal in shape and extends to a depth of 3m (Figure 4.1 - bottom).

$$h = x \tan \beta_2 + \frac{\alpha_a}{\tan \beta_1} (\tan \beta_1 - \tan \beta_2) \tanh \left(\frac{x \tan \beta_1}{\alpha_1} \right) - \alpha_2 \exp \left[-5 \left(\frac{x - x_c}{x_c} \right)^2 \right] \quad (4.1)$$

4.3.2 Model Configuration

The full model domain is decomposed into eight sub-domains for the application of a domain-decomposition approach within D-3D (Figure 4.2). Domain decomposition allows a domain to be broken up into sub-domains with variable resolutions that are run on separate proces-

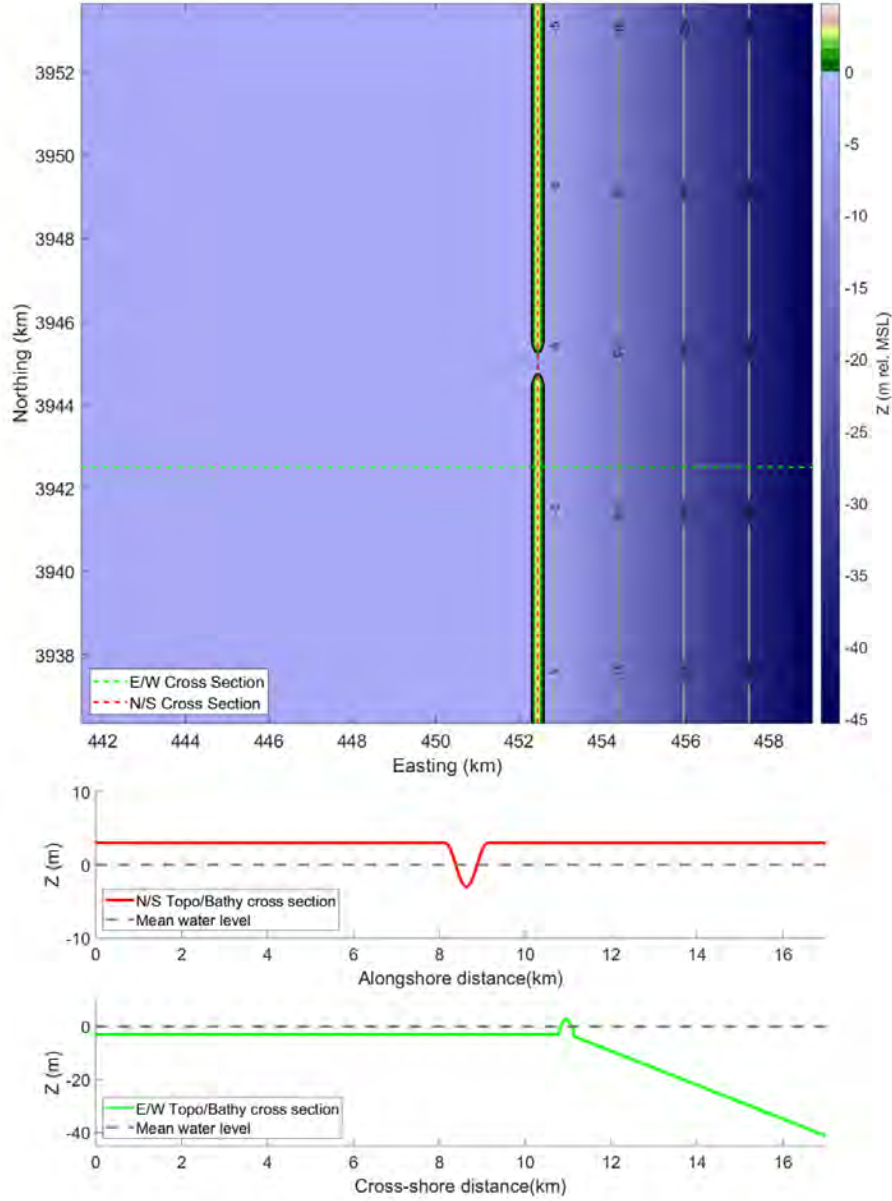


Figure 4.1: The synthetic domain extends 18km in the y-direction and 18km in the x-direction. There is a 3m deep sound on the west side, separated from the ocean on the East side by a 300m wide and 3m tall island with an inlet centered in the y-direction

sors and relay relevant information to other processors along the boundaries. Application of this approach was used to create a constant and high resolution rectilinear grid over the vicinity of the inlet and ebb-tidal delta and a courser resolution grid over the large surrounding areas. A 15m resolution was used in the vicinity of the inlet in sub-domains b, c, d, and g. In the areas surrounding the inlet, (sub-domains a and e), a 45m resolution was used. In areas further from the inlet (sub-domains f and h), a 135m resolution was used. Even within areas defined by the courser grid, the large scale hydrodynamic patterns could evolve naturally which prevents boarder effects from propagating into the inlet area. Because each domain is run on separate processors and requires inter-processor communication at each time step, sub-domains were constructed with a similar number of cells to improve computational efficiency.

All sub-domains were set up to be simulated in a depth integrated mode. A grain size (D₅₀) of 0.35mm was used throughout and the roughness was estimated with a Chézy roughness coefficient of 65 and horizontal viscosity and diffusivity were set to 1 and 10(m^2/s) based on early estimations suggested for Oregon Inlet by Velasquez-Montoya and Overton (2017). Van Rijn (2007) sediment transport formulation was used which lets waves and currents modify the bottom shear stress. A time step of 3s was used to meet estimates for the CFL relation for the finest resolution grids.

Astronomic tidal levels are forced on the east side ocean boundary. The tidal forcing is based on the 4 dominant tidal constituents (M2, S2, SA, N2) from a tidal gauge located in Duck, NC, 50 km north of Oregon Inlet. Respectively, these constituents have amplitudes of 0.557, 0.083, 0.224 and 0.111m. A Neumann type (gradient) forcing was applied to the North and South ocean boundaries with a 0 magnitude to allow water surface features to naturally progress along these borders with neither reflections nor an abrupt water level forcing. Sound side borders were forced with a 0-water level and a 2000s2 reflection parameter alpha to simulate full dissipation of tidal energy within the large sound.

SWAN was run over an evenly spaced 90m resolution grid covering the full domain. Hy-

hydrodynamic and resulting morphodynamic results were integrated into wave simulations via bilinear interpolation of FLOWs water level, current and bathymetry records every 60minutes. In all simulations with waves, a generic jonswap spectra (Hasselmann et al., 1973) ranging from $0.05Hz$ to $1Hz$ over 24 bins was used with a single $0.1Hz$ frequency peak and directional spreading factor of 4.

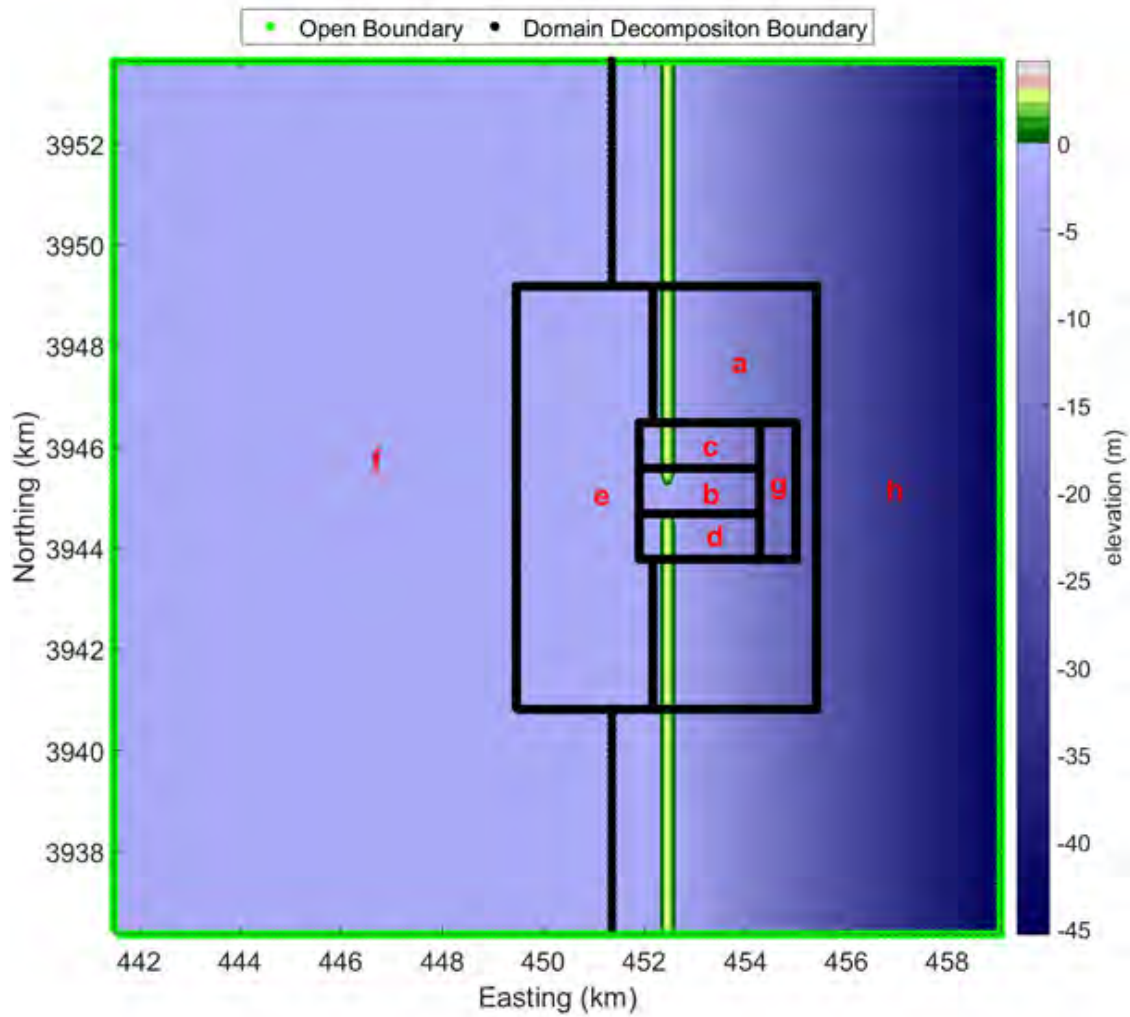


Figure 4.2: An initial synthetic topo-bathymetric surface was constructed and divided into 8 sub-domains of varying resolution for application of domain-decomposition in D-3D.

4.3.3 Model Scenarios

A schematic of the model development is shown in Figure 4.3. Starting with the initial featureless inlet, a 180-day simulation was conducted with the tidal forcing constituents representative of those on the Outer Banks and 1m high, 10s period normally incident (90 degrees relative to North) waves in the form of a jonswap spectrum. Sediment transport and morphologic evolution began after a 12-hour delay to allow stabilization of initial numerical noise. The topo-bathymetric surface resulting from this preliminary simulation was used to initialize 4 follow up simulations (Figure 4.3), each running for 90-days.

The first simulation maintained the same forcings and serves as the control. For each of the three additional simulations, a single parameter was varied relative to the control. In Scenario A, the wave angle was rotated 45° such that waves propagated from 45° relative to North on the east ocean border. In Scenario B, the wave angle remained at 90° while a sub-tidal oscillation was forced on the sound side borders. The oscillation representing sub-tidal events is composed of alternating positive and negative sinusoids with maximum amplitudes of 0.75m that occur over 5 days with 5-day periods of zero forcing between each event (Figure 4.4). In Scenario C, the control forcings were maintained, but a terminal groin was inserted along the northern edge of the southern island. The groin is represented by a thin dam in D-3D, an infinitely thin and impenetrable layer along cell borders.

4.4 Results

The control scenario produced a simple and relatively symmetric but more realistic inlet system (see Figure 4.3). Scouring of the main ebb-channel as well as other channels in the back bay provided sediment to form a flood tidal delta (FTD) and ebb tidal delta (ETD). The FTD is large and marked by various channels and shoals, like that at Oregon Inlet. The ETD is smaller and simpler. Marginal flood channels are present on either side of the inlet between the shorelines and the ETD.

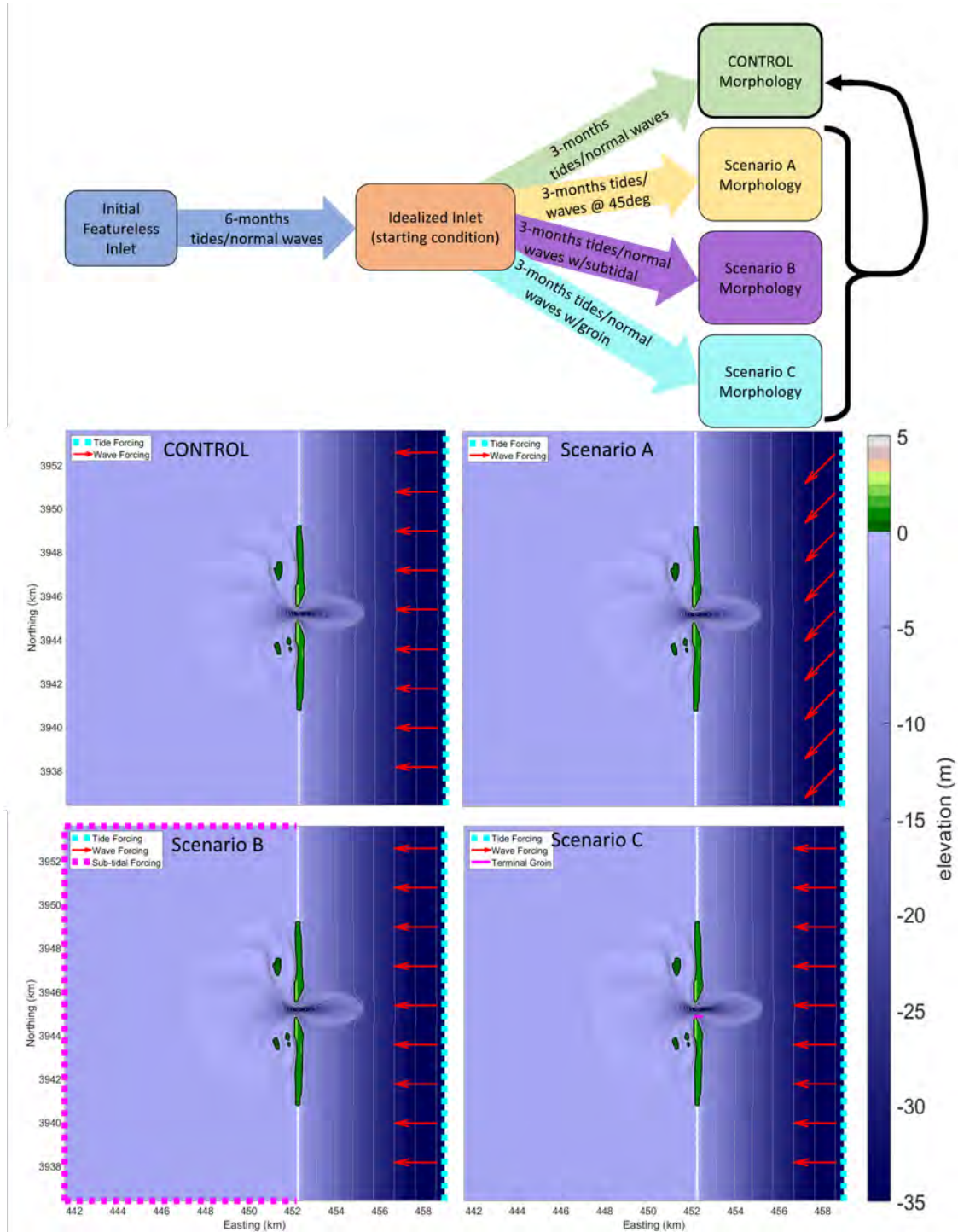


Figure 4.3: The initialized topo-bathymetric surface was used as a starting bathymetry to simulate a control scenario and 3 test scenarios. The Control maintains the same forcings and setup as the initialization run and serves as a control. Scenario A is forced by waves on a 45° relative to north. Scenario B includes a sub-tidal oscillation forced along the sound-side borders. Scenario C includes a terminal groin along the northern terminus of the southern island.

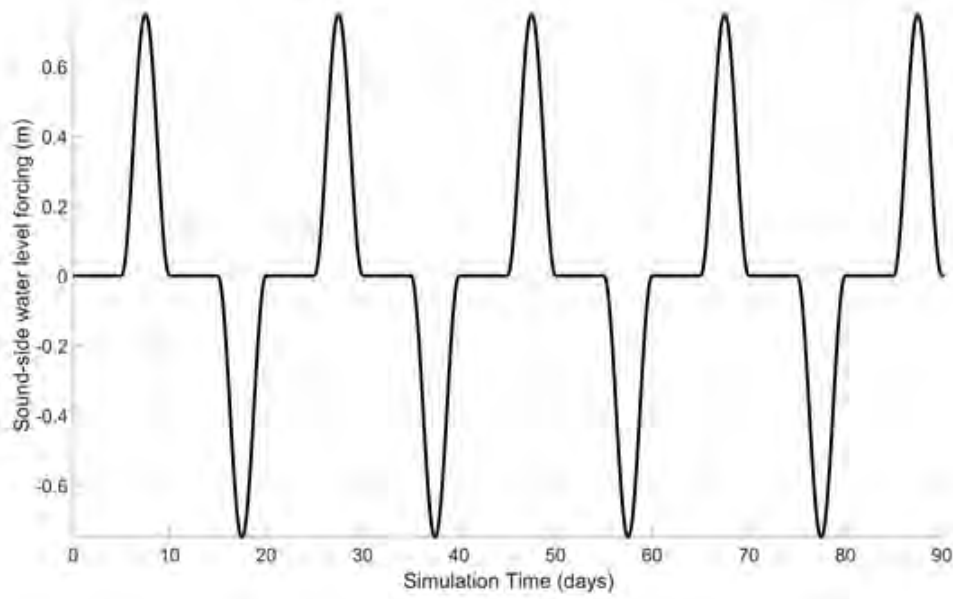


Figure 4.4: In Scenario B, a sub-tidal water level forcing was applied to the sound-side boundaries. The signal consists of alternating positive and negative sinusoids occurring over 5 days with 5 days of zero forcing in between.

Applying the same forcings to this resulting topo-bathymetric surface for 90 more days (CONTROL) resulted in a similar morphology (Figure 4.5). On the ocean side of the inlet, sediment continued to be transported through the marginal flood channels into the main ebb channel. Here, it was either transported to the FTD or ETD. Sediment was predominantly transported away from the inlet over the FTD with the exception of several channels near the sound side of the islands that delivered sediment into the main ebb channel. The remaining test scenarios were compared against these results.

In the test Scenario A, the rotation of the wave angle to 45° relative to North altered the sediment transport patterns, particularly over the ETD (Figure 4.6 - Top). These transport modifications, as well as those to the resulting morphology, are examined by subtracting the Scenario A surface and transport patterns from those of the control (Figure 4.6 - Bottom). Over the ETD terminal lobe, bathymetric alterations are more than $3m$ with a clear pattern of additional southward transport.

In Scenario B, the sound side sub-tidal oscillations, like those that may be produced

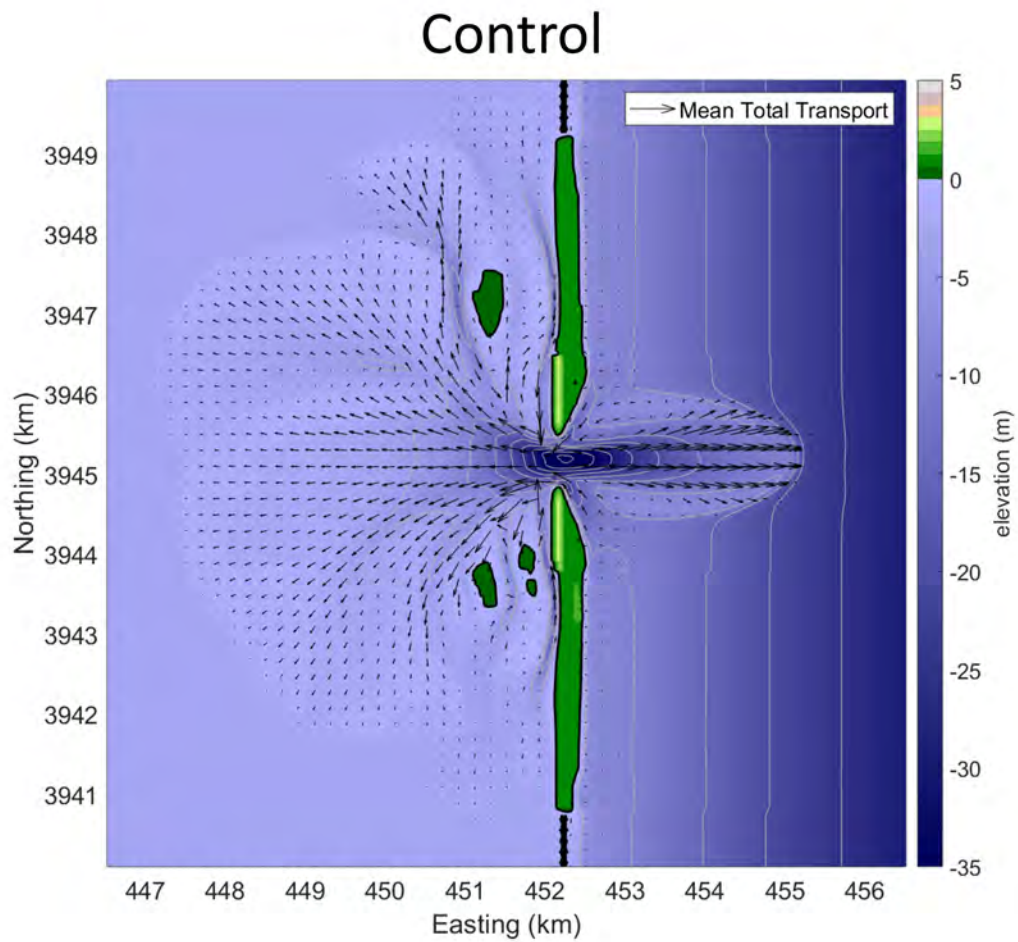


Figure 4.5: The topo-bathymetric surface and mean-total sediment transport patterns from the control Scenario.

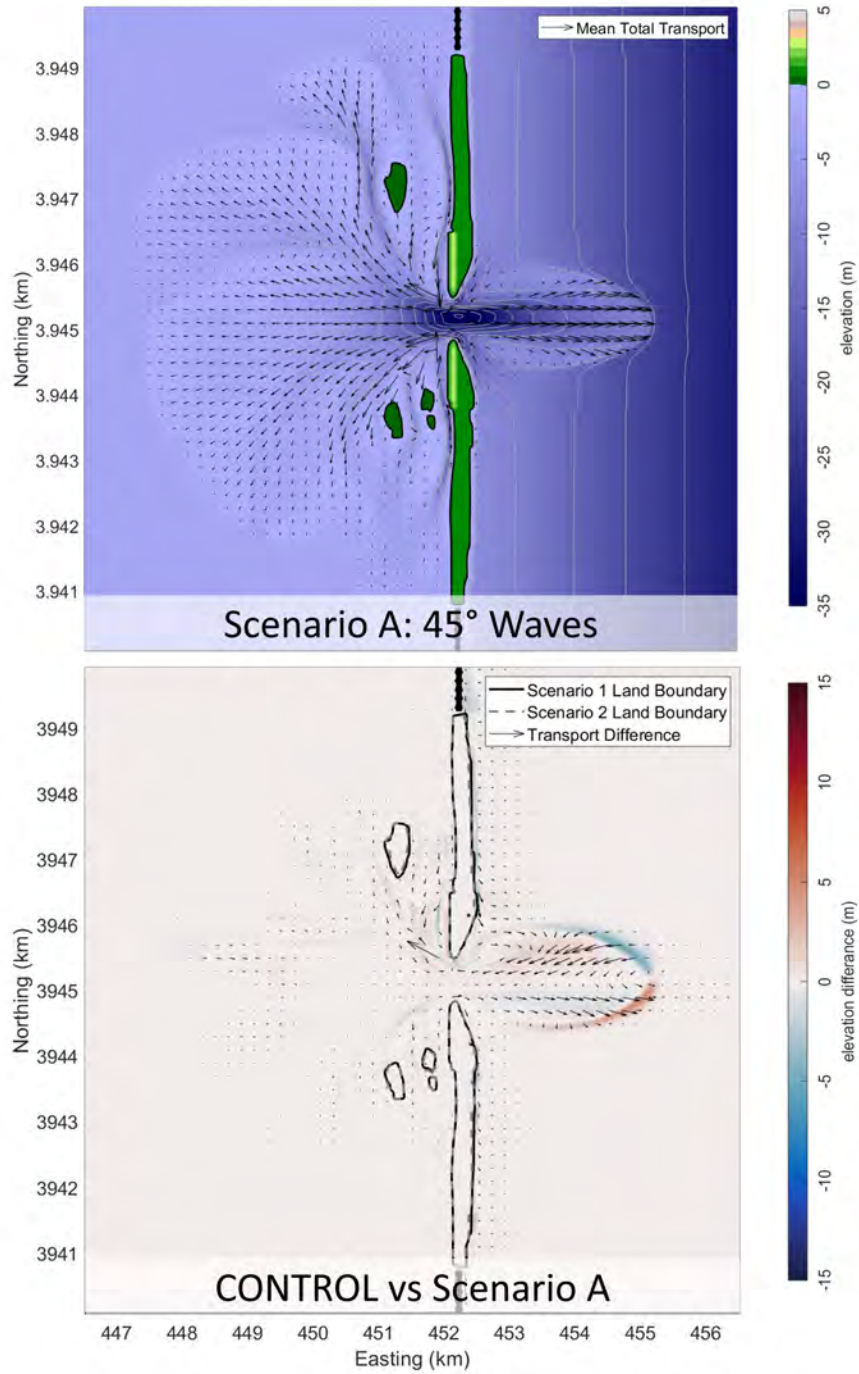


Figure 4.6: Top, the topo-bathymetric surface and mean-total sediment transport vectors from Scenario A that included incident waves from 45° relative to North. Bottom, the difference in end-state topobathymetric surfaces and transport vectors between the control and scenario B. Note that warm colors indicate that Scenario B had a higher elevation (shallower depth) than the control.

by strong wind events, dramatically altered sediment transport patterns through the inlet (Figure 4.7 - Top). Relative to the control, a large excess of sediment was scoured from the main ebb channel and inner parts of the ETD and deposited further seaward, extending the perimeter of the ETD (Figure 4.7 - bottom). There was also a shallowing along the sides of the main ebb channel near the termini of the two islands, though there was no major change in the depths of the marginal flood channels. Depths were relatively deeper over much of the ETD, but shallower along shoals near the inlet and over the entire perimeter of the ETD where it was extended further into the sound.

Scenario C differed from the other two test scenarios in that all forcings remained identical to the control, but a structure was inserted into the domain. The mean-total transport patterns show an angling of the transport directions and very limited transport through the southern marginal flood channel where the groin was inserted (Figure 4.8 - Top). Relative to the control, there were significant bathymetric changes resulting from groin that extended throughout the inlet system (Figure 4.8 - bottom). There is a relative shoaling on the northern half of the ETD terminal lobe, and a deepening on the southern side. There is a substantial shoaling on the inlet side of the groin, as well as a filling in of the southern marginal flood channel. There is a relative deepening of the main ebb channel along an axis tilted slightly from southwest to northeast and a shoaling of the southern inner portion of the ETD.

4.5 Discussion

There is a constant feedback between coastal morphology and hydrodynamics. When some hydrodynamic force transports sediment and modifies morphology, the modified morphology then alters the hydrodynamics, together resulting in a coupled evolution of the two processes over space and time. At a tidal inlet, this may allow a single hydrodynamic alteration to drive a hydro-morphodynamic disturbance that influences the system dynamics well beyond the location and time of the original alteration. However, the interactions of many disturbances

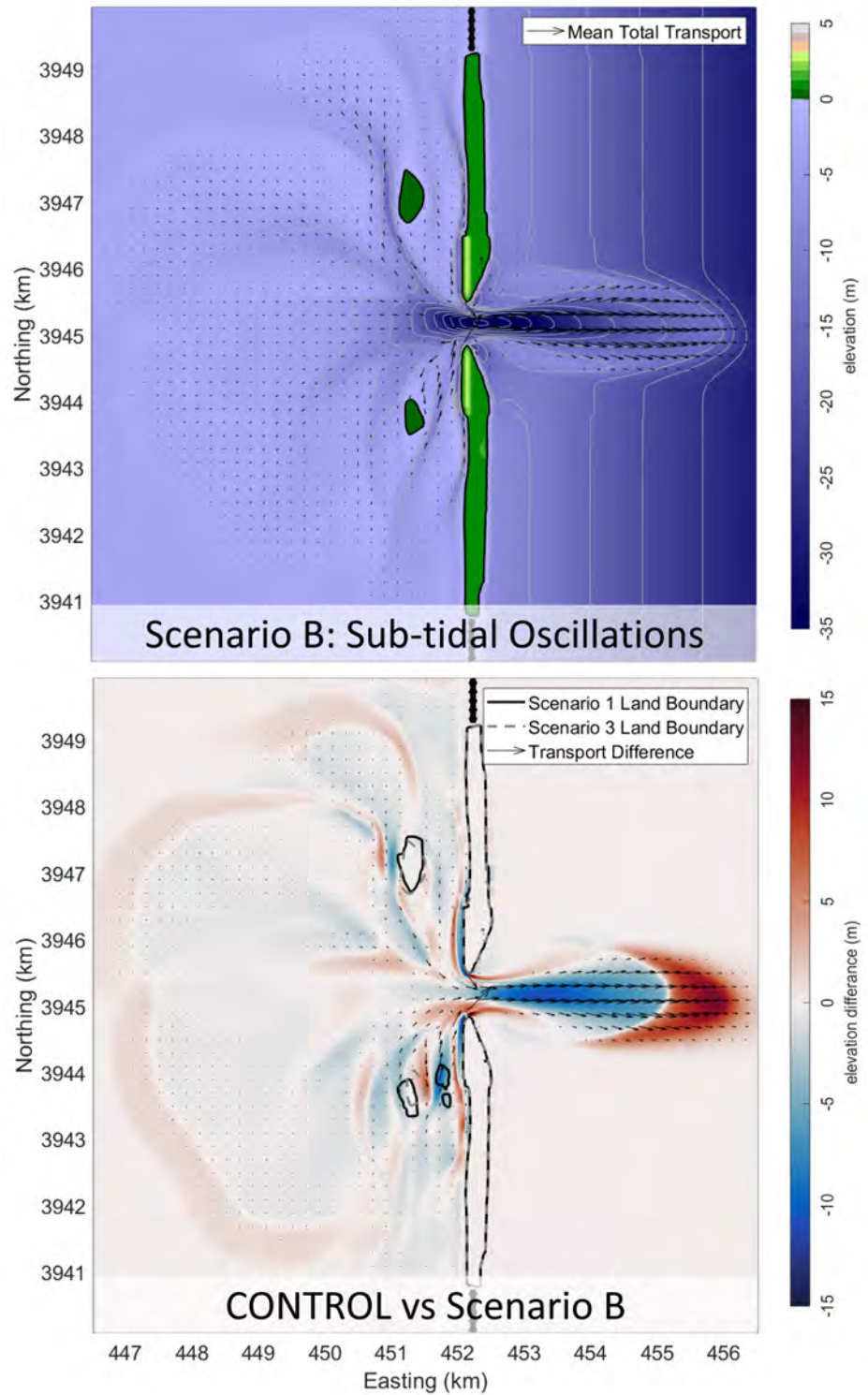


Figure 4.7: Top, the topo-bathymetric surface and mean-total sediment transport vectors from scenario B that included a sub-tidal water level forcing on the sound side of the inlet. Bottom, the difference in end-state topobathymetric surfaces and transport vectors between the control and scenario B. Note that warm colors indicate that Scenario A had a higher elevation (shallower depth) than the control.

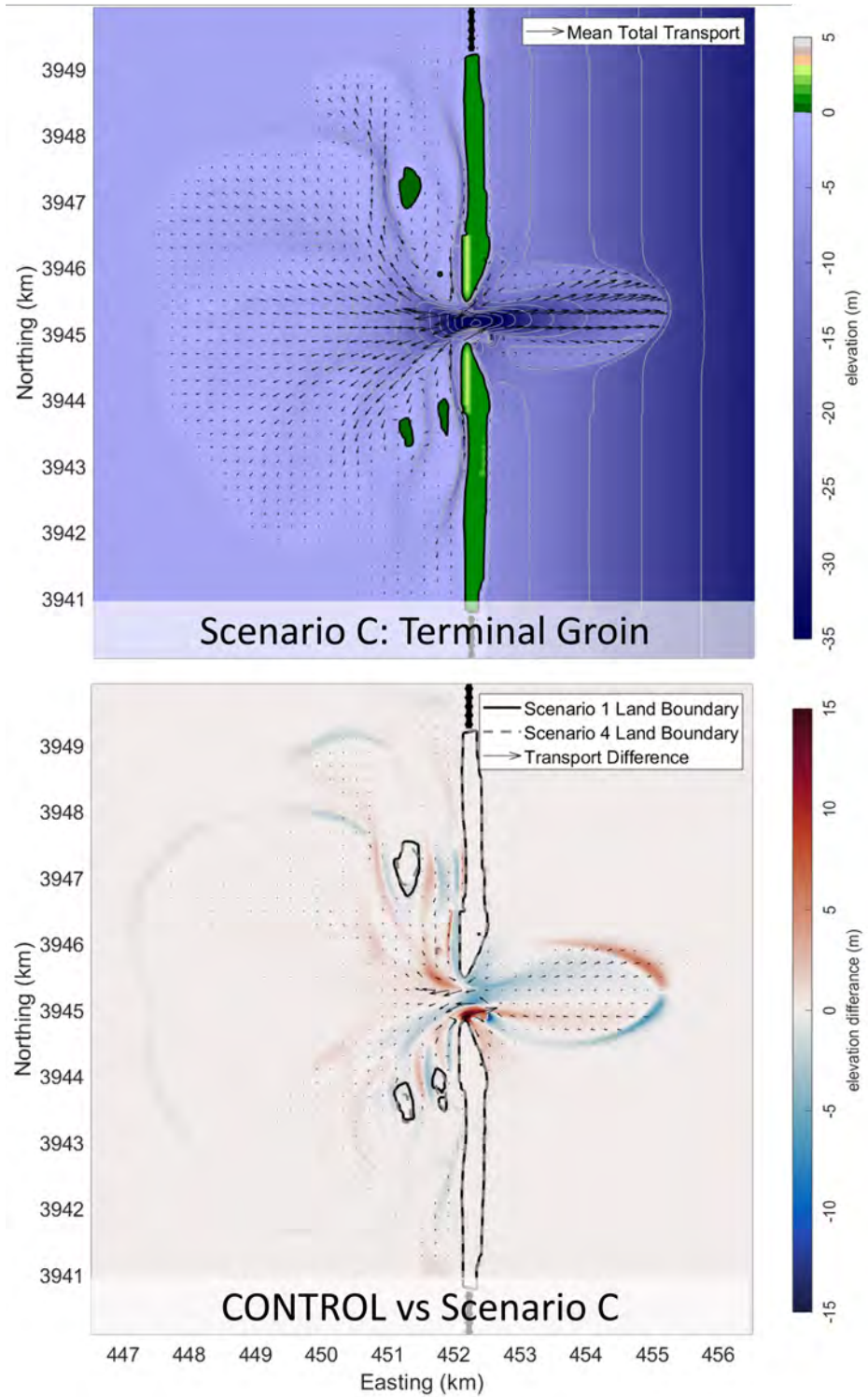


Figure 4.8: Top, the topo-bathymetric surface and mean-total sediment transport vectors from scenario C that included a representation of a terminal groin on the northern side of the southern land mass. Bottom, the difference in end-state topobathymetric surfaces and transport vectors between the control and scenario C. Note that warm colors indicate that Scenario C had a higher elevation (shallower depth) than the control.

and forcing variations makes it difficult to connect unique responses to individual forcing changes. In this study, the hydro-morphodynamic disturbances associated with a several prominent hydrodynamic or morphodynamic alterations are isolated using synthetic and idealized simulations. While these simulations do not capture the complex nature of real-world forcings, they enable each disturbance to be examined individually and compared to a control simulation.

The four idealized simulations (Control, A, B, and C) are initiated on a topo-bathymetric surface that results from an initial 180-day simulation. This initial simulation begins with a completely featureless inlet, as described previously in the methods section. Astronomical tides and normally incident wave forcing are then applied during the initial simulation to produce a more realistic but still idealized inlet system. During the initial simulation, the inlet channel is scoured by tidal currents and the sediment is transported outside of the inlet throat where it settles to form flood- and ebb-tidal deltas. As in nature, the lateral extent of the ebb-tidal delta is limited by landward oriented wave forces. Still, the terminal lobe extends 3km offshore. To the North and South of the primary channel, between the ebb-tidal delta and the islands, marginal flood channels form in response to strong flooding currents. On the landward side of the inlet, the flood-tidal delta extends nearly 5 km radially from the inlet throat and various meandering channels incise the delta including well developed marginal ebb channels adjacent to the sound-side of the islands. Very shallow shoal features develop between channels that are subaerial during low tides.

The spatial extent and depths associated with the tidal-deltas and channels are like those at Oregon Inlet which served as a general model for the overall setup. However, the depth of the primary channel in the simulations reaches nearly 35m, substantially deeper than the primary channel at Oregon Inlet which rarely exceeds 20m depth. There are many factors that could contribute to this difference, including the chosen hydrodynamic parameters, the uniform grain size used, or the downslope sediment transport in the transverse direction (a commonly underestimated term at tidal inlets that leads to overly deep channels according

to Baar et al., 2019). Regardless, differences between the idealized model and a specific site are expected. Individual model parameters could be tuned to replicate a site more exactly such as Oregon Inlet, but that would not necessarily benefit the goal of this work which is to simulate gross morphologic patterns of a wave-dominated tidal inlet in a highly controllable and generic simulation.

Starting with the topo-bathymetric surface resulting from the initial simulation, a control scenario was simulated for 90 days during which all model parameters were held constant to the initial simulation. The results of the control (see Figure 4.5) showed that sediment continued to be transported out of the inlet throat onto the delta systems. This may suggest the system did not reach an equilibrium state, though it can be noted that morphologic evolution had slowed dramatically relative to the initial simulation. Some of the simulated transported is also indicative of normal inlet dynamics: sediment is transported through the marginal channels into the inlet throat, where strong tidal currents transport that sediment to the deltas and then, in some cases, back to the shoreline. Similar patterns have been observed at Oregon Inlet (McNinch and Humberston, 2019).

In Scenario A, the deep-water incident wave angle was rotated to 45° rel. North rather than 90° rel. North as in the Control scenario. This resulted in waves approaching the shoreline and inlet at an angle. As the angled waves shoal and refract to become more shore parallel, a portion of their excess momentum flux (radiation stress) is converted into a bottom stress as well as a longshore current (Longuet-Higgins, 1970). Both processes may drive sediment transport in the alongshore direction. At a tidal inlet, the influence of these alongshore forces may be complicated by cross-shore oriented tidal currents. However, Humberston et al. (2019) found a strong relationship existed between wave driven alongshore transport and alongshore shoal migration over the ebb-tidal delta at Oregon Inlet.

Comparing the morphologic and sediment transport results of Scenario A to the control provides some insights into the bulk morphologic effects of angled waves relative to normally incident waves. Unsurprisingly, there is a clear North to South transport. Sediment is

transported from the northern edge of the ebb-tidal delta landward into the interior of the delta and the main ebb-channel. Conversely, sediment from the internal portion of the southern ebb-tidal delta is transported seaward to the southern edge of the ebb-tidal delta. There is also a deepening of the northern marginal flood channel, potentially a consequence of increased wave and longshore currents accelerating transport within this feature. A shoal feature begins to form due to deposition on the landward side off the terminus of the northern island. This may represent the genesis of a recurring spit, though a longer simulation would be necessary to see how this feature develops. Interestingly, some of the shoal and channel development over the flood tidal delta also differ from the control, particularly on the North side. Since wave forcing only occurs at a significant level over the ebb-tidal delta and nearly all wave energy is dissipated through the inlet, this is an example of how a hydro-morpho-disturbance may propagate beyond the vicinity where the original forcing is altered.

In Scenario B, the incident wave angle is again set to be normally incident, and a water level oscillation over sub-tidal time scales is applied to the sound side boundaries. Numerous studies have shown that regional winds may dramatically alter water levels in the sound, often over sub-tidal time scales associated with the passing of atmospheric fronts (Mulligan et al., 2015; Thompson et al., 2014; Van Weerdenburg, 2019). In a follow up study, (Chapter 3; Humberston et al., submitted to JGR 2021) found that such wind driven water level changes may have a first-order influence on tidal inlet hydrodynamics. Preliminary evidence from a remote sensing study further suggested that these wind driven hydrodynamic alterations may be a major control of the cross-shore movement of shoals on the ebb-tidal delta (McNinch and Humberston, 2019).

Although the sub-tidal water level in the sound was forced to oscillate in both the positive and negative directions, Figure 4.7-Top shows that the resulting transport was dominated by scour of the main ebb channel and that the sediment was predominantly transported seaward to the ebb-tidal delta. Comparing these results to the control (Figure 4.7-bottom) shows that the sound side sub-tidal water level oscillations had a dramatic influence on the inlets

morphology. The seaward most edge of the ebb-tidal delta was extended nearly $2km$ further seaward while North and South lateral extends were not dramatically altered. The entire perimeter of the flood-tidal delta was also extended about $0.7km$. The extension of the tidal deltas likely results from increases in current velocities associated with pressure forcing from the sub-tidal oscillations. As noted in Chapter 3, wind induced sub-tidal water level changes will at times be in phase with tidal currents, and at other times oppose them. However, it seems that the dominant morphological effect results from the periods of acceleration of currents rather than periods of reduced current magnitude.

Besides the extension of the tidal deltas, Scenario B shows substantial changes in the morphodynamics of the inner shoals and channels of the inlet system. Even while the primary ebb channel deepens, long, narrow shoals begin to develop to either side of the channel. These may be similar to a feature observed at Oregon Inlet (Humberston et al., 2019). On the landward side of the inlet, the channels and shoal systems within the flood-tidal delta become generally more pronounced (ie. deeper channels and shallower shoals). This suggests that the inlet system morphology is adapting to the increased flow velocities that must pass through the system owing to the sub-tidal forcing. Following results that showed regional winds may have a first-order influence on tidal inlet hydrodynamics, this scenario would suggest that wind induced currents may also have a first-order influence on the inlet system morphology. The simulation suggests that the acceleration of tidal currents by wind induced sub-tidal currents leads to exaggerated inlet system morphology relative to what would be expected based on the regional tidal range. While these effects will be particularly noticeable where there is a large and shallow back-bay system, as defined in these simulations, it seems likely that winds should be considered amongst tidal range and wave climate as a dominant control of inlet morphology.

The last test simulation, Scenario C, maintains all hydrodynamic forcings of the control scenario, but a thin dam (infinitely thin and impenetrable structure in model space) is inserted along the northern terminus of the southern island to represent a terminal groin.

The design of the groin is based on the groin constructed at Oregon Inlet and follows the natural curve of the island along the inlet and then, on the ocean side, extends linearly seaward to the original extent of the shoreline (Figure 4.9). At Oregon Inlet, the groin was put in place to prevent further erosion of the southern island that was threatening the stability of the bridge ramp. As planned, this caused a sand fillet to form within the concave nook of the groin, essentially rebuilding a portion of the eroded island (Figure 4.10). Scenario C, which is simulated for 90 days, does not capture the full creation of a sand fillet, but deposition patterns do clearly demonstrate that the hydrodynamics due to the insertion of the terminal groin are causing the equivalent area of the idealized model to shallow (Figure 4.9). It is also interesting to note similar deposition on the northern (channel side) of the groin in both reality and simulation, as well as the development of a new marginal flood channel just seaward of the end of the groin.

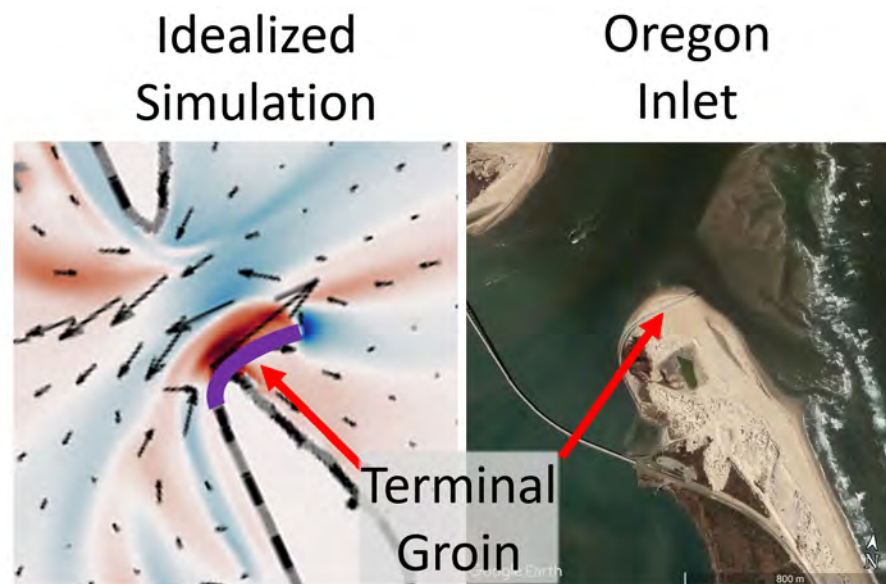


Figure 4.9: Left, a zoom of the results of Scenario C, where the purple line represents the position of the infinitely thin dam used to simulate a terminal groin. Right, a zoom in of Oregon Inlet focused on the terminus of the southern island that is maintained by a terminal groin. This satellite image was collected in 2006.

The effects of the insertion of the terminal groin also extend well beyond its immediate vicinity, and these effects would be more challenging to identify and relate to the groin in

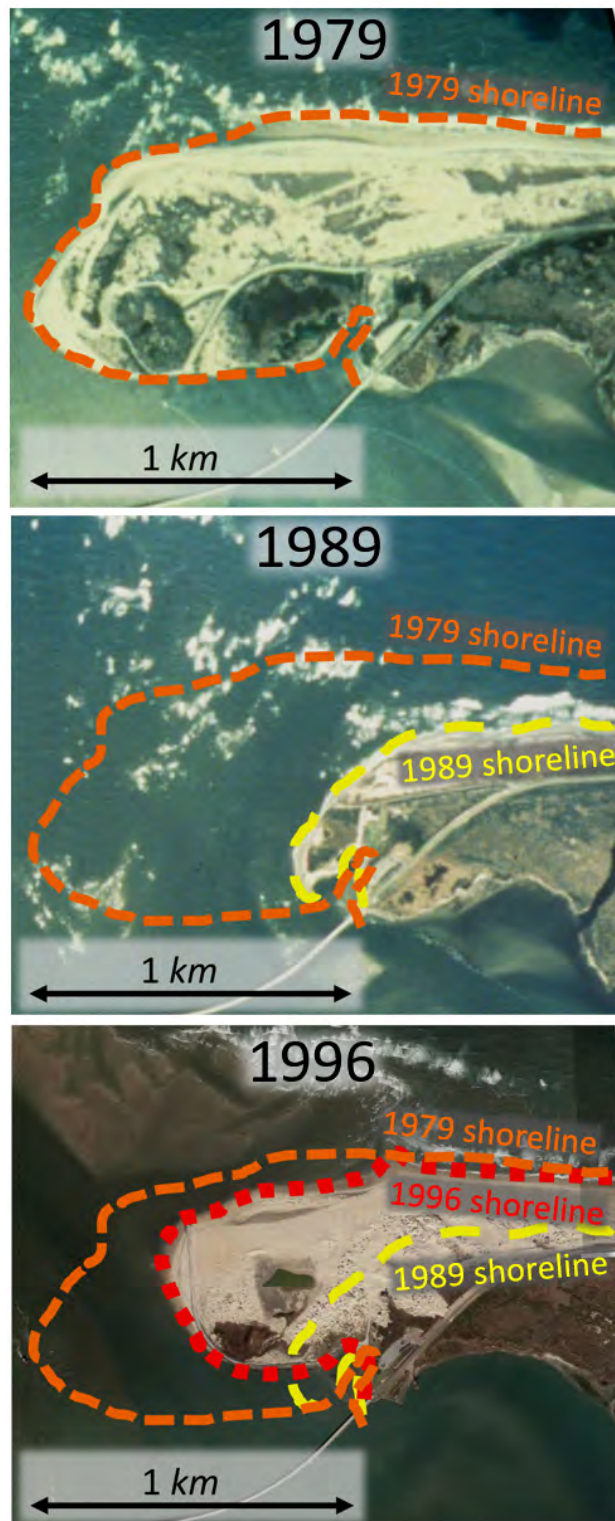


Figure 4.10: From top to bottom, 3 aerial images of Oregon Inlet from 1979, 1989, and 1996. The shorelines of each are marked for the year the image was collected as well as in all subsequent images.

nature or in a more complex model. The insertion of a groin along the terminus of the South Island causes asymmetric transport patterns over the ebb-tidal delta and within the main ebb channel. Comparing Scenario C to the control, it can be noted that the terminal groin is beginning to cause an angling of the main channel, like what is seen at Oregon Inlet (see Figure 4.9 and 4.8). It appears that the sediment scoured from the evolving channel is deposited along the terminal lobe of the northern side of the inlet. Conversely, there is increased erosion along the southern terminal lobe, and that sediment is transported landward into the interior of the ebb tidal delta. On the landward side of the inlet, many of the channels to the south of the inlet deepen while most of the channels to the north shallow. This too is akin to Oregon Inlet, where bathymetric surveys and current observations show the angling of the main channel forces increased flow to the south over the flood tidal delta. Lastly, there is a minor reduction in sediment deposited along the perimeter of the flood tidal delta. This may suggest that groin is ultimately reducing flow and transport to these further reaches and is another prime example of how a highly localized disturbance may alter hydrodynamics and morphology much further away.

4.6 Conclusions

A synthetic digital elevation map (DEM) was created whose bulk features are representative of the Outer Banks barrier island system in the vicinity of Oregon Inlet. This includes a large and shallow bay, a roughly $1km$ wide inlet defined by narrow islands, and an offshore slope similar to that measured for the Outer Banks. The DEM was used to initialize a 180-day initial simulation within the Delft-3D modeling suite. The initial simulation was run with astronomical tidal water levels and JONSWAP spectra of waves ($1m$ significant wave height, $10s$ peak period). The resulting surface formed a more realistic but still highly idealized tidal delta system that included deltas and meandering channels.

Four follow up scenarios were initialized with the surface resulting from the initial simulation. First, a control scenario extended the same forcing parameters for an additional 90

days. Scenario A altered the wave angle to be 45° rel. N and resulted in asymmetric transport over the ebb-tidal delta. In Scenario B, sub-tidal water level oscillations were forced on the sound-side boundaries to represent the water level modifications observed in Chapter 3 (Humberston et al., submitted to JGR 2021). Combined with tidal and wave forcing, these sub-tidal oscillations led to increased scour within the main inlet channel, extensions of both the flood- and ebb-tidal deltas, and more pronounced channel features incising these systems. In Scenario C, wave and water level forcings were reverted to that of the control, but a terminal groin feature like that at Oregon Inlet was inserted along the terminus of the southern island using a 'thin dam,' which in Delft-3D, prevents a flow or transport through the cell. This resulted in a morphologic setup where the primary channel was beginning to angle northward on the ocean side, and southward on the sound side. There was also increased deposition to either side of the groin, as qualitatively observed at Oregon Inlet, and small changes to the deposition patterns on both deltas.

It can be noted that the simulations were not realistically tuned to match Oregon Inlet exactly, but it was still able to provide qualitative insights into the complex relationships between forcing changes and the spatially and temporally evolving morphologic responses. Many of the most prominent morphologic features at Oregon Inlet can begin to be explained by examining the morphologic reactions captured in the idealized model. Wave angle, sound-side sub-tidal oscillations, and a terminal groin all prompted notable morphologic reactions that resembled those observed at Oregon Inlet.

CHAPTER 5

Conclusions

A barrier island is little more than an over-sized sandbar, and yet they provide a number of crucial roles for coastal environments (Figure 5.1). For starters, it is fitting that they are called 'barriers' as they receive and dissipate the great energy of the open ocean, shielding the areas behind them where elaborate but more delicate ecosystems may exist. Without the protection of barrier islands, these inland coastal habitats, filled with spawning marine species, migrating birds, and productive plant life, could not exist.

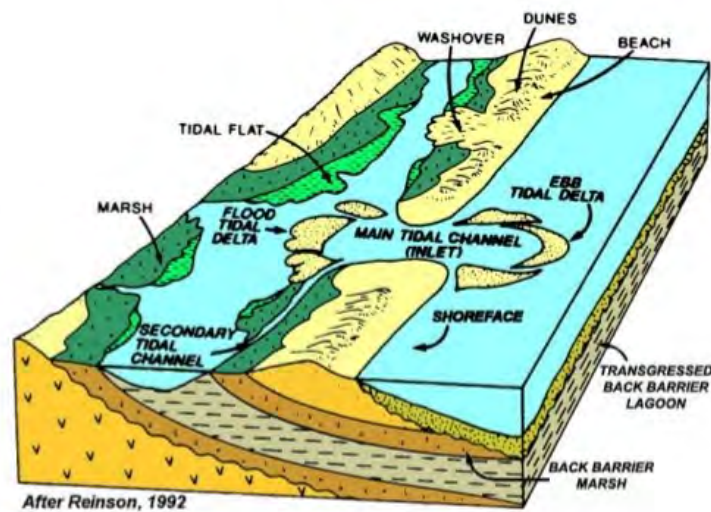


Figure 5.1: A schematic of barrier island system from Reinson (1992). The islands are composed primarily of sand forced landward by wave action, and overlay back barrier marsh material from a previous period of lower sea level. The island is marked by a tidal inlet and washover events and shelters the back barrier marshes and mud flats.

In spite of their apparent robustness, the fate of most barrier islands depends on a delicate balance between sediment inputs, exports, and sea level. They are essentially the

physical phenomenon representing a dynamic equilibrium between wave, tidal and other coastal forces. As sea levels shift, this equilibrium point may shift landward or seaward, causing the barrier island to migrate (Figure 5.2). However, if a barrier island is prevented from shifting, either by a lack of sediment availability or human intervention, the system will fall out of equilibrium and may quite literally dissolve (Figure 5.3).

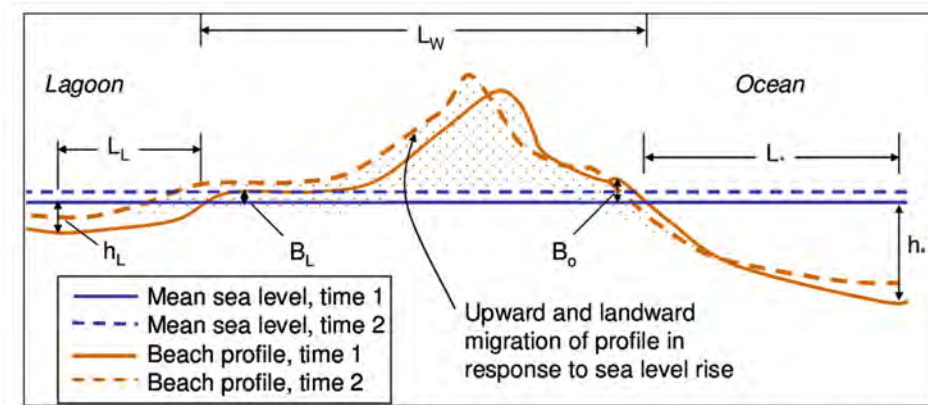


Figure 7. Bruun Rule modified for barrier island migration due to sea level rise (adapted from Dean and Maurmeyer 1983; Dean et al. 2002).

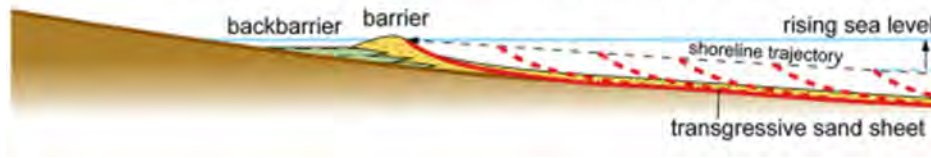


Figure 5.2: Top, a schematic of a incremental shift in barrier island position associated with a rise in sea level. Bottom, a schematic of the long term migration of a barrier island into the back bay due to rising sea levels. . From (Rosati, 2009; Zecchin et al., 2019)

While the relationship between sea level and barrier island location may be simple in theory, it becomes exceptionally complex when considering the sediment dynamics along hundreds of miles of shoreline with various sources and sinks, each experiencing unique coastal forces. The installation of hard structures for engineering projects, as well as physically pumping sediment from one location to another for dredging and nourishment projects, introduces another layer of complexity for barrier island evolution that has not been well constrained at the system level. Nonetheless, with the fate of thousands of km^2 of valuable natural habit and many billions of dollars of infrastructure on the line, efforts to understand these complex systems must continue.



Figure 5.3: Top, a major breach of the Outer Banks near the town of Hatteras caused by Hurricane Isabel, 2003 (photo: US Geological Survey). Bottom, destruction near the town of Rodanthe on the Outer Banks caused by Hurricane Irene (2011) that devastated more than 1,100 homes in the state, costing \$70 million in damages. (photo: REUTERS)

Tidal inlets are one of the most influential components of a barrier island system, suggests this author, but also one of the least constrained in terms of internal processes, external controls, and inter-barrier island system dependencies. On an open sandy coastline, exposed geologic features or sand bars may focus wave energy and cause local erosion or even dramatic overwash events. Still, unless these result in the development of a new inlet, wave action and alongshore transport tend to smooth any major discontinuities to maintain a relatively linear island form. This is not true at a tidal inlet.

Tidal inlets are the gateway between the ocean and an inland water body where tidal currents are concentrated by a hydrodynamic constriction between the open ocean and the protected inland water body. Relative to the great stretches of open beaches, their footprint is relatively small ($1km$ width), yet their influence may be far reaching. Cross-shore oriented tidal inlet currents disrupt alongshore sediment transport pathways, and the intricacies of these currents determine whether sediment may bypass the inlet and nourish the downcurrent coast, or if it will be removed and stored away more permanently.

The opportunities and challenges presented by tidal inlets also makes them a focal point for human engineering efforts, further complicating their processes. Access from inland safe harbors to the open ocean is a valuable and often rare resource for commercial and recreational vessels, and tidal inlets may naturally fulfill this valuable role, though rarely without some level of intervention to maintain permanent and easily navigable channels. And from the perspective of land transportation, tidal inlets are just the opposite, a hurdle to be overcome. The pilings and ramps of the large bridge structure constructed for this purpose further alter inlet flow characteristics and may also limit the available routes for marine vessels. Between the myriad coastal forces and human intervention at tidal inlets, it becomes a great challenge to grasp the net hydro- and morpho-dynamics. Such is the case at Oregon Inlet, NC where the complex interplay between natural dynamics and human development is especially clear.

5.1 The story of Oregon Inlet

Oregon Inlet is a wave-dominated inlet system located between Bodie and Pea Island on the Outer Banks of North Carolina (Figure 5.4). The inlet originated during a large storm event in 1845 that precipitated a sound to ocean breach of the island, an event first witnessed and reported by a vessel named the *Oregon* that was sheltered within the sound during this time (Hardy and Carney, 1962). Following its formation, the inlet rapidly migrated southward at rates averaging from $23m/year$ to $165m/year$ due to prevalent southward alongshore currents driven by major storm events from the northeast (Hardy and Carney, 1962; Pilkey et al., 1998). Significant engineering of the inlet began in 1962 and 1963 when the \$4 million Bonner bridge was constructed to replace a haphazard ferry system and unite segments of North Carolina Highway 12 on Bodie and Pea Island, a strategic step in opening mainstream tourism to the southern Outer Banks. Following construction, however, the inlet continued its southerly march which lead to severe navigation channel infilling and eventually threatened to strand the bridge's southern ramp within the inlet. Plans were developed to stabilize the inlet via a pair of 3.2 km jetties but, for various reasons, were never realized. Instead, a roughly 1-km terminal groin was constructed along the northern edge of Pea Island (the southern edge of Oregon Inlet) in 1989-1991 (Riggs et al., 2009).

Storms surges and waves have driven several new breaches of the Northern Outer Banks in recent decades, but all have since naturally closed and Oregon Inlet remains the only connection between the ocean and sounds for nearly $200km$. Although there are strong tidal currents within the main channel, Oregon Inlet is generally considered a classic example of a wave-dominated inlet due to the relationship between the tidal range and wave climate that result in an expansive flood-tidal delta relative to the ebb-tidal delta that is more constrained by wave action (see Figure 5.4). Since construction of the terminal groin, the migration of the southern edge of the Oregon Inlet has come to a halt, but wave driven transport continues to be dominant from the North. This has caused continuous navigation channel infilling around



Figure 5.4: A satellite image of Oregon Inlet, NC that shows the expansive flood-tidal delta channels and shoals, the condensed flood-tidal delta, the terminal groin, and the nearby beach faces.

what was the only navigation span of the Bonner Bridge and required nearly continuous maintenance dredging as the cost of millions of dollars (Figure 5.5). The installation of the terminal groin is also suspected to have caused a narrowing of the inlet throat (McNinch and Humberston, 2019). Since Oregon Inlet is not considered a high traffic inlet, funds for dredging have been stretched thin as this challenging site, like at many low to medium trafficked inlets around the United States, and the Corps has often struggled to maintain the recommended 14*ft* draft clearance. At times, the depth of the channel through the primary navigation span has been reduced to as little as 2*ft* and become entirely impassible. This is a major concern for the commercial fishing fleets that use the inlet daily and are a necessary year-round component of the otherwise highly seasonal economy.



Figure 5.5: As a recurring spit intrudes upon the navigation channel, a single hopper dredger attempts to clear the channel through the only navigation span of the Bonner Bridge.

Faced with the ongoing cost of maintenance dredging and growing concerns about the integrity of the aging Bonner Bridge, a decision was made to replace the bridge with the Marc Basnight Bridge (Figure 5.6). This new 2.8 mile bridge, costing more than \$250 million, provides continuous clearance for vessels across the width of the inlet in nine 350*ft* spans.

However, even as the pilings of the old bridge are removed to make these new spans available for vessels, Oregon Inlet has continued to challenge mariners. The constantly shifting shoals over the ebb-tidal delta have made it a challenge for the Coast Guard to maintain effective navigational markers and dozens of vessels have run aground. During large wave events, wave breaking may occurs around the entire parameter of the ebb-tidal delta, rendering it highly dangerous for navigation or, at times, entirely impassable.

This ongoing story of human development, engineering, and then re-engineering at Oregon Inlet demonstrates the remarkable challenge local communities and the Corps face in balancing the need for navigable marine and ground passageways with natural processes and environmental impacts. The outcome of these efforts at Oregon Inlet is not particularly clear; some studies suggest this balance has been found (Overton et al., 1993) while others suggest the groin and other human intervention are playing a role in destabilizing the larger island system (Riggs et al., 2009). In either case, there is an obvious lack of understanding in why and how this system evolves and how those changes affect the large barrier island system.

5.2 Insights from this work

The studies presented in previous chapters focus on the mechanisms and methods of evolution at Oregon Inlet. The goal was to learn more about why this system has evolved as it has, and extrapolate those findings to provide guidance for this and other similar systems now and into the future. Chapter 2 discusses the development and use of a new x-band radar remote sensing system (RIOS) at Oregon Inlet to measure shoal movement over the dynamic ebb-tidal delta for 9 months (McNinch and Humberston, 2019). The spatially averaged alongshore rate of the shoal movements on the ebb-tidal delta is well correlated with estimated wave driven transport and the net annual transport rate during this time is comparable with a previous estimate. However, it is also noted that the alongshore sediment flux is dominated by individual storm events that may lead to dramatically different



Figure 5.6: Top, the construction of the new Marc Basnight Bridge that spans Oregon Inlet. Bottom, the completed March Basnight Bridge (left) next to the the old Bonner Bridge (right) before its removal.

seasonal transport signals and result in large inter-annual variability in net alongshore flux (Humberston et al., 2019). This has important implications for both inlet infilling as well as sediment availability for the down current coastlines. From the same data set, McNinch and Humberston (2019) found another intriguing relationship: the cross-shore mobility of shoals on the ebb-tidal delta is highly correlated to a sub-tidal water level gradient that is unassociated with astronomical tides.

Chapter 3 further explored this thread. *In situ* current and pressure sensors confirmed the presence of the sub-tidal water level gradient and showed that a similar signal existed in the current time series within the main inlet channel. Based on previous studies and a simple wind surge model, it seems that the sub-tidal gradient is set up by regional wind patterns that have opposing effects to either side of the inlet. A force balance at the inlet indicates that the currents associated with the regionally induced water level gradient are far larger than currents resulting from local wind or wave effects and are comparable in magnitude to the tidal currents. Models may benefit from this insight, but it also raises several new questions: if winds may be a first-order influence on tidal inlet currents, should they be introduced into the classification scheme that is presently based only on waves and tides? Further, if regional winds have such a significant influence on tidal inlet currents, might they have a similar influence on inlet morphology?

These questions, as well as questions on the impact of waves and engineering modifications, were examined in Chapter 4 using an idealized numerical modeling approach. An idealized model was constructed to run highly controlled simulations that isolate the specific morphodynamic reactions of the inlet system to single forcing or structural changes relative to a control. The idealized model is not designed to closely replicate Oregon Inlet, but bulk characteristic of Oregon Inlet and the Northern Outer Banks were used to design the synthetic inlet system such that similar hydrodynamic and morphologic patterns would naturally form. In the first test scenario, rotating wave angle from normally incident to 45° rel. North supported findings from Chapter 2; asymmetric wave forcing will result in

asymmetric morphodynamics over the ebb-tidal delta. Interestingly, other morphodynamic alterations were also observed within the marginal flood channels in this scenario, and channels incising the flood-tidal delta were also altered despite nearly all wave energy dissipating before reaching this area.

The second test applied sub-tidal oscillations to the sound side boundaries, similar in magnitude and duration to those caused by winds (Chapter 3). The results suggested that the morphology reacts to the periodic acceleration of tidal currents by the sub-tidal forcing. The main inlet channel was scoured to greater depths and the ebb-tidal delta was extended seaward while the flood-tidal delta was extended landward. Overall, both channels and shoals in the system became more pronounced due to the sub-tidal oscillations and this scenario demonstrated that sub-tidal water level oscillations may significantly alter tidal inlet morphology, primarily by exaggerating already existing features.

The last test scenario examined the effects of inserting a terminal groin along the terminus of one of the islands, like at Oregon Inlet. In the simulation, the groin causes the primary channel to begin to pivot such that the ocean side channel was oriented more northward, a trend observed at Oregon Inlet. The groin also resulted in infilling on its southern seaward side (as happened at Oregon Inlet) and additionally caused changes to channel and shoal development throughout the inlet system. In all test scenarios, the hydro-morpho-dynamics disturbances associated with a single forcing or structural change propagated throughout the system, well beyond the area of the original alteration. While it would be untenable to relate the many simultaneous and interacting disturbances to their origin forces in nature, or even in a more complex model, the idealized modeling approach provides a unique ability to track the individual propagating disturbances relative to the initial alteration.

The relationship between regional winds and tidal inlet morphodynamics appears to be strong, at least at Oregon Inlet, NC. There are numerous inlets along barrier island systems that also enclose large and shallow water bodies and are likely to experience similar wind influence. At other inlets, the water level of the inland water body may be less susceptible

to wind influence if they are not large and shallow like the Pamlico Sound inland of Oregon Inlet. Nonetheless, it may still be the case that ocean side wind induced surge may alone significantly alter tidal inlet currents and morphodynamics. For example, there was a period during the study at Oregon Inlet when the wind surge along the ocean side of Oregon Inlet dominated the sub-tidal water level gradient and forced nearly 2 days of constant flooding through inlet throat.

This topic may also be better examined through additional numerical modeling efforts, both real and synthetic. For a realistic model, this work shows that accurately simulating tidal inlet flow and morphodynamics likely requires including wind influence. This may be achieved through water level observations along boundaries that may be used to force a hindcast simulation. For a predictive model, a realistic and accurate forecast of the regional wind field and its effect on water levels would be required. Accurately constructing either is not a menial task. Incorporated correctly though, wind influence may help numerical models better simulate real processes at a tidal inlet, and provide improved guidance of future inlet dynamics.

5.3 Closing Remarks

Tidal inlets like Oregon Inlet are astonishingly complex coastal systems, but they provide such great utility for human activities and exert such a strong influence on the regional coastal environment that we must continue our venture to understand their behavior. This work underscores the importance of winds to natural coastal processes. In addition to generating waves, winds may also cause set-up and set-down of the coastal water levels and their drag on the water surface may directly force currents. This work also highlights the need for coastal engineering plans to incorporate an understanding of the far reaching natural coastal processes that contribute or respond to tidal inlet systems. An important take away conclusion is that we are still discovering some of the most important environmental forces that dictate how tidal inlet systems evolve. An important corollary is that we also do not

have a firm grasp on how tidal inlets and the broader coastal system respond to human intervention. This work improves our understanding in both regards; winds are a first-order influence of tidal inlet hydro- and morpho-dynamics and engineering structures may have broad and cascading effects on inlet morphology. Going forward, these two lessons may be brought together to develop a more synchronous approach to human development in these environments.

LIST OF REFERENCES

- Alessi, C. A., Beardsley, R. C., Limeburner, R., Rosenfeld, L. K., Lentz, S. J., Send, U., Winant, C. D., Allen, J. S., Halliwell, G. R., Brown, W. S., et al. (1985). Code-2: Moored array and large-scale data report.
- Ashton, A. D. and Murray, A. B. (2006). High-angle wave instability and emergent shore-line shapes: 1. modeling of sand waves, flying spits, and capes. *Journal of Geophysical Research: Earth Surface*, 111(F4).
- Aubrey, D. G. (1993). *Formation and evolution of multiple tidal inlets*. American Geophysical Union.
- Baar, A., Albernaz, M. B., Van Dijk, W., and Kleinhans, M. (2019). Critical dependence of morphodynamic models of fluvial and tidal systems on empirical downslope sediment transport. *Nature communications*, 10(1):1–12.
- Balouin, Y., Howa, H., and Michel, D. (2001). Swash platform morphology in the ebb-tidal delta of the barra nova inlet, south portugal. *Journal of Coastal Research*, pages 784–791.
- Barrick, D. (1972). Remote sensing of sea state by radar. In *Ocean 72-IEEE International Conference on Engineering in the Ocean Environment*, pages 186–192. IEEE.
- Bass, F., Fuks, I., Kalmykov, A., Ostrovsky, I., and Rosenberg, A. (1968). Very high frequency radiowave scattering by a disturbed sea surface part ii: Scattering from an actual sea surface. *IEEE Transactions on Antennas and Propagation*, 16(5):560–568.

- Beardsley, R., Mofjeld, H., Wimbush, M., Flagg, C., and Vermersch Jr, J. (1977). Ocean tides and weather-induced bottom pressure fluctuations in the middle-atlantic bight. *Journal of Geophysical Research*, 82(21):3175–3182.
- Beardsley, R. C., Chapman, D. C., Brink, K. H., Ramp, S. R., and Schlitz, R. (1985). The nantucket shoals flux experiment (nsfe79). part i: A basic description of the current and temperature variability. *Journal of Physical Oceanography*, 15(6):713–748.
- Beardsley, R. C., Limeburner, R., and Owens, W. B. (2004). Drifter measurements of surface currents near marguerite bay on the western antarctic peninsula shelf during austral summer and fall, 2001 and 2002. *Deep Sea Research Part II: Topical Studies in Oceanography*, 51(17-19):1947–1964.
- Bell, P. S. (1999). Shallow water bathymetry derived from an analysis of x-band marine radar images of waves. *Coastal Engineering*, 37(3-4):513–527.
- Bell, P. S. (2002). Determination of bathymetry using marine radar images of waves. In *Ocean Wave Measurement and Analysis (2001)*, pages 251–257.
- Bergsma, E., Conley, D., Davidson, M., and O’Hare, T. (2016). Video-based nearshore bathymetry estimation in macro-tidal environments. *Marine Geology*, 374:31–41.
- Bertin, X., Fortunato, A. B., and Oliveira, A. (2009). A modeling-based analysis of processes driving wave-dominated inlets. *Continental Shelf Research*, 29(5-6):819–834.
- Bird, E. C. F. (1969). Coasts. Technical report.
- Birkemeier, W. A., Miller, H. C., Wilhelm, S. D., DeWall, A. E., and Gorbics, C. (1985). A user’s guide to the coastal engineering research center’s (cerc’s) field research facility. Technical report, Coastal Engineering Research Center Bicksburg, MS.
- Booij, N., Ris, R. C., and Holthuijsen, L. H. (1999). A third-generation wave model for

- coastal regions: 1. model description and validation. *Journal of geophysical research: Oceans*, 104(C4):7649–7666.
- Boothroyd, J. C. (1985). Tidal inlets and tidal deltas. In *Coastal sedimentary environments*, pages 445–532. Springer.
- Bowen, A., Inman, D., and Simmons, V. (1968). Wave set-down and set-up. *Journal of Geophysical Research*, 73(8):2569–2577.
- Bruun, P. (1978). Common reasons for damage or breakdown of mound breakwaters. *Coastal Engineering*, 2:261–273.
- Catálan, P. A. and Haller, M. C. (2008). Remote sensing of breaking wave phase speeds with application to non-linear depth inversions. *Coastal Engineering*, 55(1):93–111.
- Catalán, P. A., Haller, M. C., and Plant, W. J. (2014). Microwave backscattering from surf zone waves. *Journal of Geophysical Research: Oceans*, 119(5):3098–3120.
- Chen, J.-L., Hsu, T.-J., Shi, F., Raubenheimer, B., and Elgar, S. (2015). Hydrodynamic and sediment transport modeling of new river inlet (nc) under the interaction of tides and waves. *Journal of Geophysical Research: Oceans*, 120(6):4028–4047.
- Clunies, G. J., Mulligan, R. P., Mallinson, D. J., and Walsh, J. (2017). Modeling hydrodynamics of large lagoons: Insights from the albemarle-pamlico estuarine system. *Estuarine, Coastal and Shelf Science*, 189:90–103.
- Costanza, R., d’Arge, R., De Groot, R., Farber, S., Grasso, M., Hannon, B., Limburg, K., Naeem, S., O’neill, R. V., Paruelo, J., et al. (1997). The value of the world’s ecosystem services and natural capital. *nature*, 387(6630):253–260.
- Davidson-Arnott, R., Bauer, B., and Houser, C. (2019). *Introduction to coastal processes and geomorphology*. Cambridge university press.

- Davis, R. A. (1994). Barrier island systemsa geologic overview. In *Geology of Holocene barrier island systems*, pages 1–46. Springer.
- Davis, R. E. (1976). Predictability of sea surface temperature and sea level pressure anomalies over the north pacific ocean. *Journal of Physical Oceanography*, 6(3):249–266.
- Díaz Méndez, G. M., Haller, M. C., Raubenheimer, B., Elgar, S., and Honegger, D. A. (2015). Radar remote sensing estimates of waves and wave forcing at a tidal inlet. *Journal of Atmospheric and Oceanic Technology*, 32(4):842–854.
- Dissanayake, D., Roelvink, J., and Van der Wegen, M. (2009). Modelled channel patterns in a schematized tidal inlet. *Coastal Engineering*, 56(11-12):1069–1083.
- Dolan, R. and Glassen, R. (1973). Oregon inlet, north carolinaa history of coastal change. *Southeastern Geographer*, 13(1):41–53.
- Donelan, M. A. and Pierson Jr, W. J. (1987). Radar scattering and equilibrium ranges in wind-generated waves with application to scatterometry. *Journal of Geophysical Research: Oceans*, 92(C5):4971–5029.
- Elias, E., Cleveringa, J., Buijsman, M., Roelvink, J., and Stive, M. (2006). Field and model data analysis of sand transport patterns in texel tidal inlet (the netherlands). *Coastal Engineering*, 53(5-6):505–529.
- Elias, E., Stive, M., Bonekamp, H., and Cleveringa, J. (2003). Tidal inlet dynamics in response to human intervention. *Coastal engineering journal*, 45(04):629–658.
- Elias, E. P., Van der Spek, A. J., Pearson, S. G., and Cleveringa, J. (2019). Understanding sediment bypassing processes through analysis of high-frequency observations of ameland inlet, the netherlands. *Marine Geology*, 415:105956.
- Faria, A. G., Thornton, E., Stanton, T., Soares, C. k., and Lippmann, T. (1998). Vertical

- profiles of longshore currents and related bed shear stress and bottom roughness. *Journal of Geophysical Research: Oceans*, 103(C2):3217–3232.
- Farneback, G. (2003). Two-frame motion estimation based on polynomial expansion. In *Scandinavian conference on Image analysis*, pages 363–370. Springer.
- Fiechter, J., Steffen, K. L., Mooers, C. N., and Haus, B. K. (2006). Hydrodynamics and sediment transport in a southeast florida tidal inlet. *Estuarine, coastal and shelf science*, 70(1-2):297–306.
- FitzGerald, D. M. (1982). Sediment bypassing at mixed energy tidal inlets. In *Coastal Engineering 1982*, pages 1094–1118.
- FitzGerald, D. M. (1988). Shoreline erosional-depositional processes associated with tidal inlets. In *Hydrodynamics and sediment dynamics of tidal inlets*, pages 186–225. Springer.
- FitzGerald, D. M. (1996). Geomorphic variability and morphologic and sedimentologic controls on tidal inlets. *Journal of Coastal Research*, pages 47–71.
- FitzGerald, D. M. and Buynevich, I. V. (2003). *Tidal inlets and deltas*, pages 737–741. Springer Netherlands, Dordrecht.
- FitzGerald, D. M., Kraus, N. C., and Hands, E. B. (2000). Natural mechanisms of sediment bypassing at tidal inlets.
- FitzGerald, D. M. and Pendleton, E. (2002). Inlet formation and evolution of the sediment bypassing system: New inlet, cape cod, massachusetts. *Journal of Coastal Research*, (36):290–299.
- Fitzgerald, D. M., Penland, S., and Nummedal, D. (1984). Control of barrier island shape by inlet sediment bypassing: East frisian islands, west germany. *Marine Geology*, 60(1-4):355–376.

- Forte, M. F., Birkemeier, W. A., and Mitchell, J. R. (2017). Nearshore survey system evaluation. Technical report, ERDC-CHL Vicksburg United States.
- Fulton, M., Scott, G., Fortner, A., Bidleman, T., and Ngabe, B. (1993). The effects of urbanization on small high salinity estuaries of the southeastern united states. *Archives of Environmental Contamination and Toxicology*, 25(4):476–484.
- Gao, J. (2009). Bathymetric mapping by means of remote sensing: methods, accuracy and limitations. *Progress in Physical Geography*, 33(1):103–116.
- Gerritsen, H., De Goede, E., Platzek, F., Genseberger, M., van Kester, J., and Uittenbogaard, R. (2007). Validation document delft3d-flow; a software system for 3d flow simulations. *The Netherlands: Delft Hydraulics, Report X*, 356:M3470.
- Giese, G. S., Borrelli, M., and Mague, S. T. (2020). Tidal inlet evolution and impacts of anthropogenic alteration: An example from nauset beach and pleasant bay, cape cod, massachusetts. *Northeastern Naturalist*, 27(sp10):1–21.
- Greer, J. M. (2011). *The wealth of nature: Economics as if survival mattered*. New Society Publishers.
- Haller, M. C., Honegger, D., and Catalan, P. A. (2014). Rip current observations via marine radar. *Journal of waterway, port, coastal, and ocean engineering*, 140(2):115–124.
- Haller, M. C. and Lyzenga, D. R. (2003). Comparison of radar and video observations of shallow water breaking waves. *IEEE transactions on geoscience and remote sensing*, 41(4):832–844.
- Hardy, A. and Carney, D. (1962). North carolina hurricanes; a descriptive listing of storms which have affected the state. *US Weather Bureau Publication*, page 26.
- Hasselmann, K., Barnett, T. P., Bouws, E., Carlson, H., Cartwright, D. E., Enke, K., Ewing, J., Gienapp, H., Hasselmann, D., Kruseman, P., et al. (1973). Measurements of wind-wave

- growth and swell decay during the joint north sea wave project (jonswap). *Ergänzungsheft* 8-12.
- Hayes, M. (1979). Barrier island morphology as a function of tidal and wave regime. in: Leatherman sp (ed) barrier islands. *Academic Press, New York*, 1:27.
- Hayes, M. O. (1975). Morphology of sand accumulation in estuaries: an introduction to the symposium. In *Geology and Engineering*, pages 3–22. Elsevier.
- Hayes, M. O. (1980). General morphology and sediment patterns in tidal inlets. *Sedimentary geology*, 26(1-3):139–156.
- Hayes, M. O. and FitzGerald, D. M. (2013). Origin, evolution, and classification of tidal inlets. *Journal of Coastal Research*, (69):14–33.
- Hayes, M. O., Goldsmith, V., and Hobbs III, C. H. (1970). Offset coastal inlets. In *Coastal Engineering 1970*, pages 1187–1200.
- Hayes, M. O. and Kana, T. W. (1976). *Terrigenous Clastic Depositional Environments: Some Modern Examples; a Field Course Sponsored by the American Association of Petroleum Geologists*. Department of Geology, University of South Carolina.
- Herrling, G. and Winter, C. (2018). Tidal inlet sediment bypassing at mixed-energy barrier islands. *Coastal Engineering*, 140:342–354.
- Hessner, K., Reichert, K., Borge, J. C. N., Stevens, C. L., and Smith, M. J. (2014). High-resolution x-band radar measurements of currents, bathymetry and sea state in highly inhomogeneous coastal areas. *Ocean Dynamics*, 64(7):989–998.
- Holman, R. and Haller, M. C. (2013). Remote sensing of the nearshore. *Annual Review of Marine Science*, 5:95–113.
- Holman, R. A., Sallenger, A. H., Lippmann, T. C., and Haines, J. W. (1993). The application of video image processing to the study of nearshore processes. *Oceanography*, 6(3):78–85.

- Holman, R. A. and Stanley, J. (2007). The history and technical capabilities of argus. *Coastal engineering*, 54(6-7):477–491.
- Hopkins, J., Elgar, S., and Raubenheimer, B. (2018). Storm impact on morphological evolution of a sandy inlet. *Journal of Geophysical Research: Oceans*, 123(8):5751–5762.
- Hoyt, J. H. (1967). Barrier island formation. *Geological Society of America Bulletin*, 78(9):1125–1136.
- Humberston, J., Lippmann, T., and McNinch, J. (2019). Observations of wave influence onshore ebb-tidal delta morphodynamics at oregon inlet, nc. *Marine Geology*, 418:106040.
- Inman, D. L. and Dolan, R. (1989). The outer banks of north carolina: Budget of sediment and inlet dynamics along a migrating barrier system. *Journal of Coastal Research*, pages 193–237.
- Jarrett, J. T. (1978). Coastal processes at oregon inlet, north carolina. In *Coastal Engineering 1978*, pages 1257–1275.
- Komar, P. D. (1971). The mechanics of sand transport on beaches. *Journal of Geophysical Research*, 76(3):713–721.
- Komar, P. D. (1996). Tidal-inlet processes and morphology related to the transport of sediments. *Journal of Coastal Research*, pages 23–45.
- Komar, P. D. (1998). *Beach processes and sedimentation*.
- Komar, P. D. and Inman, D. L. (1970). Longshore sand transport on beaches. *Journal of geophysical research*, 75(30):5914–5927.
- Large, W. and Pond, S. (1981). Open ocean momentum flux measurements in moderate to strong winds. *Journal of physical oceanography*, 11(3):324–336.

- Lee, P., Barter, J., Beach, K., Hindman, C., Lake, B., Rungaldier, H., Shelton, J., Williams, A., Yee, R., and Yuen, H. (1995). X band microwave backscattering from ocean waves. *Journal of Geophysical Research: Oceans*, 100(C2):2591–2611.
- Legault, K., Rosati, J. D., Engle, J., and Beck, T. M. (2012). St. Johns county, St. Augustine inlet, FL, report 1: Historical analysis and sediment budget. Technical report, ENGINEER RESEARCH AND DEVELOPMENT CENTER VICKSBURG MS COASTAL AND HYDRAULICS LAB.
- Lenstra, K. J., Pluis, S. R., Ridderinkhof, W., Ruessink, G., and van der Vegt, M. (2019). Cyclic channel-shoal dynamics at the Ameland inlet: the impact on waves, tides, and sediment transport. *Ocean Dynamics*, 69(4):409–425.
- Lesser, G. R., Roelvink, J. v., Van Kester, J., and Stelling, G. (2004). Development and validation of a three-dimensional morphological model. *Coastal engineering*, 51(8-9):883–915.
- Lillycrop, W., Parson, L., Irish, J., and Brooks, M. (1996). Hydrographic surveying with an airborne lidar survey system. In *International Airborne Remote Sensing Conference and Exhibition, 2nd- Technology, Measurement and Analysis, San Francisco, CA*.
- Lippmann, T., Herbers, T., and Thornton, E. (1999). Gravity and shear wave contributions to nearshore infragravity motions. *Journal of Physical Oceanography*, 29(2):231–239.
- Lippmann, T. and Holman, R. (1990). The spatial and temporal variability of sand bar morphology. *Journal of Geophysical Research: Oceans*, 95(C7):11575–11590.
- Lippmann, T. C. and Holman, R. A. (1989). Quantification of sand bar morphology: A video technique based on wave dissipation. *Journal of Geophysical Research: Oceans*, 94(C1):995–1011.

- Lippmann, T. C., Irish, J., and Hunt, J. (2013a). Observations of the vertical structure of tidal currents in two inlets. *Journal of Coastal Research*, (65):2029–2034.
- Lippmann, T. C., Irish, J. D., and Hunt, J. (2013b). Subtidal flow structure in tidally modulated inlets.
- Longuet-Higgins, M. S. (1970). Longshore currents generated by obliquely incident sea waves: 1. *Journal of geophysical research*, 75(33):6778–6789.
- Longuet-Higgins, M. S. and Stewart, R. (1964). Radiation stresses in water waves; a physical discussion, with applications. In *Deep sea research and oceanographic abstracts*, volume 11, pages 529–562. Elsevier.
- Lyzenga, D. R. (1991). Interaction of short surface and electromagnetic waves with ocean fronts. *Journal of Geophysical Research: Oceans*, 96(C6):10765–10772.
- Lyzenga, D. R. (1998). Effects of intermediate-scale waves on radar signatures of ocean fronts and internal waves. *Journal of Geophysical Research: Oceans*, 103(C9):18759–18768.
- MacMahan, J., van de Kreeke, J., Reniers, A., Elgar, S., Raubenheimer, B., Thornton, E., Weltmer, M., Rynne, P., and Brown, J. (2014). Fortnightly tides and subtidal motions in a choked inlet. *Estuarine, Coastal and Shelf Science*, 150:325–331.
- Mariotti, G. and Murshid, S. (2018). A 2d tide-averaged model for the long-term evolution of an idealized tidal basin-inlet-delta system. *Journal of Marine Science and Engineering*, 6(4):154.
- McNinch, J. and Humberston, J. (2019). Radamcninch2019radarr inlet observing system (rios) at oregon inlet, nc: sediment transport pathways at a wave-dominated tidal inlet. *Shore and Beach*, 87(1):24–36.
- McNinch, J. E. (2007). Bar and swash imaging radar (basir): A mobile x-band radar designed

- for mapping nearshore sand bars and swash-defined shorelines over large distances. *Journal of Coastal Research*, 23(1 (231)):59–74.
- McNinch, J. E., Brodie, K. L., and Slocum, R. K. (2012). Radar inlet observing system (rios): Continuous remote sensing of waves, currents, and bathymetry at tidal inlets. In *2012 Oceans*, pages 1–8. IEEE.
- Miller, H. C., Dennis, W. A., and Wutkowski, M. J. (1997). A unique look at oregon inlet, nc usa. In *Coastal Engineering 1996*, pages 4517–4530.
- Montreuil, A.-L., Levoy, F., Bretel, P., and Anthony, E. J. (2014). Morphological diversity and complex sediment recirculation on the ebb delta of a macrotidal inlet (normandy, france): A multiple lidar dataset approach. *Geomorphology*, 219:114–125.
- Mulligan, R. P., Walsh, J., and Wadman, H. M. (2015). Storm surge and surface waves in a shallow lagoonal estuary during the crossing of a hurricane. *Journal of Waterway, Port, Coastal, and Ocean Engineering*, 141(4):A5014001.
- Munk, W. H. (1949). The solitary wave theory and its application to surf problems. *Annals of the New York Academy of Sciences*, 51(3):376–424.
- Nichols, C. R. and Pietrafesa, L. J. (1997). Oregon inlet: hydrodynamics, volumetric flux and implications for larval fish transport. Technical report, North Carolina State Univ., Raleigh, NC (United States); North Carolina Univ .
- Nienhuis, J. H. and Ashton, A. D. (2016). Mechanics and rates of tidal inlet migration: Modeling and application to natural examples. *Journal of Geophysical Research: Earth Surface*, 121(11):2118–2139.
- O’Brien, M. P. and Zeevaert, L. (1969). Design of a small tidal inlet. In *Coastal Engineering 1968*, pages 1242–1257.

- O'Connor, M. C., Cooper, J. A. G., and Jackson, D. W. (2011). Decadal behavior of tidal inlet-associated beach systems, northwest ireland, in relation to climate forcing. *Journal of Sedimentary Research*, 81(1):38–51.
- Olabarrieta, M., Geyer, W. R., and Kumar, N. (2014). The role of morphology and wave-current interaction at tidal inlets: An idealized modeling analysis. *Journal of Geophysical Research: Oceans*, 119(12):8818–8837.
- Olabarrieta, M., Warner, J. C., and Kumar, N. (2011). Wave-current interaction in willapa bay. *Journal of Geophysical Research: Oceans*, 116(C12).
- Orescanin, M., Raubenheimer, B., and Elgar, S. (2014). Observations of wave effects on inlet circulation. *Continental Shelf Research*, 34:37–42.
- Ortiz-Suslow, D., Haus, B., Williams, N., Laxague, N., Reniers, A., and Graber, H. (2015). The spatial-temporal variability of air-sea momentum fluxes observed at a tidal inlet. *Journal of Geophysical Research: Oceans*, 120(2):660–676.
- Otvos, E. G. (2020). Coastal barriers-fresh look at origins, nomenclature and classification issues. *Geomorphology*, 355:107000.
- Overton, M., Fisher, J., Dennis, W., and Miller, H. (1993). Shoreline change at oregon inlet terminal groin. In *Coastal Engineering 1992*, pages 2332–2343.
- Pacheco, A., Vila-Concejo, A., Ferreira, Ó., and Dias, J. (2008). Assessment of tidal inlet evolution and stability using sediment budget computations and hydraulic parameter analysis. *Marine Geology*, 247(1-2):104–127.
- Pawlowicz, R., Beardsley, B., and Lentz, S. (2002). Classical tidal harmonic analysis including error estimates in matlab using t_tide. *Computers & Geosciences*, 28(8):929–937.
- Phillips, O. (1988). Radar returns from the sea surfacebragg scattering and breaking waves. *Journal of physical oceanography*, 18(8):1065–1074.

- Pianca, C., Holman, R., and Siegle, E. (2014). Mobility of meso-scale morphology on a microtidal ebb delta measured using remote sensing. *Marine Geology*, 357:334–343.
- Pilkey, O. H., Neal, W. J., Webb, C. A., Riggs, S. R., Bush, D. M., Bullock, J., Pilkey, D. F., and Cowan, B. A. (1998). *The North Carolina shore and its barrier islands: restless ribbons of sand*. Duke University Press.
- Plant, W. J., Keller, W. C., Hayes, K., and Chatham, G. (2010). Normalized radar cross section of the sea for backscatter: 1. mean levels. *Journal of Geophysical Research: Oceans*, 115(C9).
- Provan, M., Logan, S., Nistor, I., Cornett, A., and Drouin, A. (2018). Field and numerical investigations of the morpho-hydrodynamic processes of the tidal inlet at shippagan gully, new brunswick, canada. *Coastal Engineering Journal*, 60(4):400–422.
- Putrevu, U. and Svendsen, I. A. (1992). Shear instability of longshore currents: A numerical study. *Journal of Geophysical Research: Oceans*, 97(C5):7283–7303.
- Radermacher, M., Wengrove, M., van Thiel de Vries, J., and Holman, R. (2014). Applicability of video-derived bathymetry estimates to nearshore current model predictions. *Journal of Coastal Research*, (70):290–295.
- Rey, A. J. and Mulligan, R. P. (2021). Influence of hurricane wind field variability on real-time forecast simulations of the coastal environment. *Journal of Geophysical Research: Oceans*, 126(1):e2020JC016489.
- Ridderinkhof, W., De Swart, H., Van der Vegt, M., and Hoekstra, P. (2016). Modeling the growth and migration of sandy shoals on ebb-tidal deltas. *Journal of Geophysical Research: Earth Surface*, 121(7):1351–1372.
- Riggs, S. R., Ames, D. V., Culver, S. J., Mallinson, D. J., Corbett, D. R., and Walsh, J. P.

- (2009). Eye of a human hurricane: Pea island, oregon inlet, and bodie island, northern outer banks, north carolina. *Geological Society of America Special Papers*, 460:43–72.
- Robinson, A. (1975). Cyclical changes in shoreline development at the entrance to teignmouth harbour, devon, england. *Nearshore Sediment Dynamics and Sedimentation*. John Wiley, London, pages 181–198.
- Roelvink, J. and Van Banning, G. (1995). Design and development of delft3d and application to coastal morphodynamics. *Oceanographic Literature Review*, 11(42):925.
- Rosati, J. D. (2009). Barrier island migration over a consolidating substrate.
- Rosati, J. D., Walton, T., and Bodge, K. (2002). Longshore sediment transport. *Coastal Engineering Manual*, (Part III):2.
- Ruessink, B., Bell, P., Van Enckevort, I., and Aarninkhof, S. (2002). Nearshore bar crest location quantified from time-averaged x-band radar images. *Coastal Engineering*, 45(1):19–32.
- Safak, I., Warner, J. C., and List, J. H. (2016). Barrier island breach evolution: Alongshore transport and bay-ocean pressure gradient interactions. *Journal of Geophysical Research: Oceans*, 121(12):8720–8730.
- Sallenger Jr, A., Krabill, W., Swift, R., Brock, J., List, J., Hansen, M., Holman, R., Manizade, S., Sontag, J., Meredith, A., et al. (2003). Evaluation of airborne topographic lidar for quantifying beach changes. *Journal of Coastal Research*, pages 125–133.
- Sallenger Jr, A. H. and Holman, R. A. (1985). Wave energy saturation on a natural beach of variable slope. *Journal of Geophysical Research: Oceans*, 90(C6):11939–11944.
- Schumann, T. and Van Rooy, M. (1951). Frequency of fronts in the northern hemisphere. *Archiv für Meteorologie, Geophysik und Bioklimatologie, Serie A*, 4(1):87–97.
- Schwartz, M. L. (1971). The multiple causality of barrier islands. *The Journal of Geology*, 79(1):91–94.

- Shand, R. D., Bailey, D. G., and Shepherd, M. J. (1999). An inter-site comparison of net offshore bar migration characteristics and environmental conditions. *Journal of coastal Research*, pages 750–765.
- Shepard, F. (1999). P., 1963, submarine geology. *Harper and Row, New York*, 196:941–957.
- Spore, N. J. and Brodie, K. L. (2017). Collection, processing, and accuracy of mobile terrestrial lidar survey data in the coastal environment.
- Spore, N. J., Renaud, A. D., Conery, I. W., and Brodie, K. L. (2019). Coastal lidar and radar imaging system (claris) lidar data report: 2011-2017. Technical report, ENGINEER RESEARCH AND DEVELOPMENT CENTER VICKSBURG MS VICKSBURG United States.
- Stockdon, H. F., Doran, K. S., Sopkin, K. L., Smith, K. E., and Fredericks, X. (2013). Coastal topography–northeast atlantic coast, post-hurricane sandy, 2012. Technical report, US Geological Survey.
- Stockdon, H. F., Holman, R. A., Howd, P. A., and Sallenger Jr, A. H. (2006). Empirical parameterization of setup, swash, and runup. *Coastal engineering*, 53(7):573–588.
- Stockdon, H. F., Sallenger Jr, A. H., List, J. H., and Holman, R. A. (2002). Estimation of shoreline position and change using airborne topographic lidar data. *Journal of Coastal Research*, pages 502–513.
- Stutz, M. L. and Pilkey, O. H. (2001). A review of global barrier island distribution. *Journal of Coastal Research*, pages 15–22.
- Symonds, G., Black, K. P., and Young, I. R. (1995). Wave-driven flow over shallow reefs. *Journal of Geophysical Research: Oceans*, 100(C2):2639–2648.
- Thompson, P. R., Merrifield, M. A., Wells, J. R., and Chang, C. M. (2014). Wind-driven coastal sea level variability in the northeast pacific. *Journal of Climate*, 27(12):4733–4751.

- Thornton, E. B. and Guza, R. (1983). Transformation of wave height distribution. *Journal of Geophysical Research: Oceans*, 88(C10):5925–5938.
- Trizna, D. B. (1997). A model for brewster angle damping and multipath effects on the microwave radar sea echo at low grazing angles. *IEEE Transactions on Geoscience and Remote Sensing*, 35(5):1232–1244.
- Van Den Boomgaard, R. and Van Balen, R. (1992). Methods for fast morphological image transforms using bitmapped binary images. *CVGIP: Graphical Models and Image Processing*, 54(3):252–258.
- Van Rijn, L. C. (2007). Unified view of sediment transport by currents and waves. i: Initiation of motion, bed roughness, and bed-load transport. *Journal of Hydraulic engineering*, 133(6):649–667.
- Van Weerdenburg, R. (2019). *Exploring the relative importance of wind for exchange processes around a tidal inlet system: the case of Ameland Inlet*. PhD thesis, Msc. Thesis, Delft University of Technology, Delft, The Netherlands.
- Velasquez-Montoya, L. and Overton, M. (2017). Impacts of seasonal forcings on the hydrodynamics of oregon inlet, nc. In *Proceedings of Coastal Dynamics*.
- Velasquez-Montoya, L., Overton, M. F., and Sciaudone, E. J. (2020). Natural and anthropogenic-induced changes in a tidal inlet: Morphological evolution of oregon inlet. *Geomorphology*, 350:106871.
- Walton, Jr, T. L. and Dean, R. G. (2011). Addressing an optimal schedule for inlet bypassing. *Journal of Coastal Research*, 27(6A):87–93.
- Wargula, A., Raubenheimer, B., and Elgar, S. (2014). Wave-driven along-channel subtidal flows in a well-mixed ocean inlet. *Journal of Geophysical Research: Oceans*, 119(5):2987–3001.

- Wargula, A., Raubenheimer, B., Elgar, S., Chen, J.-L., Shi, F., and Traykovski, P. (2018). Tidal flow asymmetry owing to inertia and waves on an unstratified, shallow ebb shoal. *Journal of Geophysical Research: Oceans*, 123(9):6779–6799.
- Williams, W. (1947). The determination of gradients on enemy-held beaches. *The Geographical Journal*, 109(1/3):76–90.
- Winant, C. D. and Beardsley, R. C. (1979). A comparison of some shallow wind-driven currents. *Journal of physical oceanography*, 9(1):218–220.
- Wright, J. (1968). A new model for sea clutter. *IEEE Transactions on antennas and propagation*, 16(2):217–223.
- Zecchin, M., Catuneanu, O., and Caffau, M. (2019). Wave-ravinement surfaces: Classification and key characteristics. *Earth-science reviews*, 188:210–239.

APPENDIX A

Sensativity to different wave angle observations near Oregon Inlet

The spatial separation between the location of the wave buoy (offshore of the FRF in 26 m depth) and Oregon Inlet was examined to assess its potential influence on transport rates. In intermediate and shallow water, waves refract due to interaction with the bottom and their angle of incidence changes. Differences in multi-year wave angle records from the Oregon Inlet (NDBC station #44095) and FRF (NDBC station #44100) buoys, separated by approximately 60km, demonstrate that refraction patterns consistently altered the wave angles between the buoys due to their geographic separation. Wave angles measured at the buoy offshore of Oregon Inlet were an average 5.8° larger (relative to north) than those measured offshore of the FRF over a two-year period based on times when both buoys were operational. Waves of different wavenumbers and orbital velocities would experience varying degrees of refraction, but the analysis used only the average difference to account for the bulk differences in wave angles between these locations.

A simple sensitivity analysis of the effects of the bulk angle correction was conducted by computing alongshore sediment transport using the FRF measured average wave angles modified by -40° to 40° in 2° increments. Maximum correlations between the estimated alongshore transport and average alongshore bedform migration rates varied from 0.25 to 0.68 with the highest correlation occurring when angles were altered 16° . Applying a bulk rotation of 5.8° increased the correlation by 0.009 suggesting the results were not strongly influenced by using the FRF wave buoy located to the North of the inlet.